# Numerical Modelling of Multiphase Flow With Application to Industrial Processes

*Author*

Ashutosh Bhokare

[redacted]

*Supervisor*

Prof. Chenfeng Li

*Submitted to Swansea University in fulfilment of the requirements for the degree of PhD in Civil Engineering*

Swansea University
Prifysgol Abertawe

December 2020

*I would like to dedicate this thesis to my loving parents...*

# Abstract

Multiphase flows are witnessed often in nature and the industry. Simulating the behaviour of multiphase flows is of importance to scientists and engineers for better prediction of phenomena and design of products. This thesis aims to develop a multiphase flow framework which can be applied to industrial applications such as placement of concrete in construction and proppant transport in oil and gas. Techniques available in literature to model multiphase flows are systematically introduced and each of their merits and demerits are analysed. Their suitability for different applications and scenarios are established. The challenges surrounding the placement of fresh concrete in formwork is investigated. Construction defects, the physics behind these defects and existing tests used to monitor fresh concrete quality are evaluated. Methods used to simulate fresh concrete flow as an alternative to experiments are critically analysed. The potential benefits of using numerical modelling and the shortcoming of the existing approaches are established. It is found that the homogeneous Bingham model is currently the most widely used technique to model fresh concrete flow. Determining the Bingham parameters for a given concrete mix remains a challenge and a novel method to obtain values for them is demonstrated in this work. The Bingham model is also applied to a full-scale tremie concrete placement procedure in a pile. Knowledge on the flow pattern followed by concrete being placed using a tremie is extracted. This is used to answer questions which the industry currently demands. The need for a more sophisticated model is emphasised in order to obtain an even greater understanding of fresh concrete flow behaviour. A CFD-DEM framework in which the multiphase nature of concrete is captured is developed. To validate this framework a new benchmark test is proposed in conjunction with the fluidised bed experiment. A comparative study of the drag models used in CFD-DEM approaches is performed to systematically assess each of their performances. CFD-DEM modelling is then applied to model fresh concrete flow and its potential to model defect causing phenomena is demonstrated. A model to capture more complex behaviours of concrete such as thixotropy is introduced and demonstrated.

This work has not previously been accepted in substance for any degree and is not being concurrently submitted in candidature for any degree.

Signed.....  .....

Date.....20/08/2021.....

This thesis is the result of my own investigations, except where otherwise stated. Other sources are acknowledged by footnotes giving explicit references. A bibliography is appended.

Signed.....  .....

Date.....20/08/2021.....

I hereby give consent for my thesis, if accepted, to be available for photocopying and for inter-library loan, and for the title and summary to be made available to outside organisations.

Signed..... 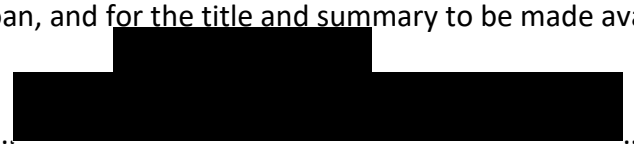 .....

Date.....20/08/2021.....

The University's ethical procedures have been followed and, where appropriate, that ethical approval has been granted.

Signed.....  .....

Date.....20/08/2021.....

# Contents

# Acknowledgement

First and foremost, I would like to thank my supervisor, Prof. Chenfeng Li, for his systematic guidance, support and inspiration at all stages of this PhD. Apart from providing me support on the technical side of things he has been a great mentor and his commitment and dedication continues to be of great inspiration. His constant encouragement at even the most difficult times of this PhD has made the completion of this thesis possible.

I would like to say a special thanks to my colleagues who have worked closely with me during the PhD. I thoroughly enjoyed working with Sizeng You and he has also been a good friend. Dr. Bjornar Sandnes and Dr. Miles Morgan have been a pleasure to collaborate with and their experience in performing experiments used in this PhD have been invaluable.

I would like to thank Swansea University, the staff here and the ZCCE for providing the environment and facilities necessary for good quality research and learning. The knowledge I have gained from taught modules during my MSc at Swansea University were the crucial stepping stones for this PhD and I am indebted to all my professors.

I would like to thank the National Research Network (NRN) for conducting workshops and seminars which I was a part of and contributed to my development. I am grateful for the support provided by Prof. Andrew Barron, Prof Wulf Dettmer, Prof. Djordje Peric and Prof. Yuntian Feng during my time as a student at Swansea University.

I would like to say a very special and whole hearted thank you to Aishwarya Vora whose support was not only crucial for the PhD but also furthering my understanding about life.

I would like to thank Bin Chen, Jinlong Fu, Matthew Hall and Jinsheng Wang from my research team for making my stay in Swansea a memorable one. Last but not least I would like to say a big thank you to my parents and my dear friends for supporting me throughout this PhD and whom without nothing would be possible.

# List of Figures

# List of Tables

# Nomenclature

### Abbreviations

CFD Computational Fluid Mechanics

DEM Discrete Element Method

DPD Dissipative particle dynamics

DPM Discrete particle modelling

FDR Force displacement relationship

FEM Finite Element Method

FVM Finite Volume Method

LBM Lattice Boltzmann method

PET Polyethylene terepthalate

PTV Particle tracking velocimetry

RCC Reinforced cement concrete

SCC Self compacting concrete

SPH Smooth particle hydrodynamics

VOF Volume of fluid

### General conventions

1. Scalars are written in regular italic typeface eg. $a, A, \alpha$.

2. Vectors, matrices and tensor quantities are written in bold typeface eg. $\mathbf{a}, \mathbf{A}, \alpha$.

3. Equations, figures, tables and reference titles are numbered relative to chapters and appendices. Cross-referencing to equations is given in round brackets, eg. (3.17), while references to bibliography titles are given in rectangular brackets, eg. [ABCD]. Figures and tables are referenced using their caption names together with their numbers, eg. Figure 7.9, Table 6.2.

4. References are listed at the end of the thesis.

**Commonly used notations**

| | |
|---|---|
| $\langle a \rangle$ | Average of a |
| $\mathcal{O}$ | Landau's symbol to depict algorithm time complexity |
| $\partial$ | Partial derivative |
| $d$ | Derivative |
| $\dot{a}$ | First derivative in time of a |
| $\nabla \cdot f$ | Divergence of f |
| $\nabla f$ | Gradient of f |
| $\int$ | Integration |
| $D$ | Material derivative |
| $max\{a, b, c\}$ | Maximum of a, b and c |
| $min\{a, b, c\}$ | Minimum of a, b and c |
| $Re$ | Reynold's number |
| $\mathbf{a} \cdot \mathbf{b}$ | Scalar product of vectors **a** and **b** |
| $\Sigma$ | Summation symbol |
| $\mathbf{a} \times \mathbf{b}$ | Vector product of vectors **a** and **b** |

# Chapter 1

# Introduction

We witness multiphase flows in numerous natural and technological systems. Examples of these include sediment transport in rivers, blood flow, drilling fluid in the petroleum industry and bubbly flow in nuclear reactors etc. Figure 1.1 shows an avalanche which is one of the many multiphase flows seen in nature. Figure 1.2 shows a process involving multiphase flows in the steel industry.

Figure 1.1: Avalanche is an example of multiphase flow

Figure 1.2: Multiphase flows in the steel industry

The study of multiphase flows is associated with the study of fluid dynamics and was

initially researched by scientists in chemical engineering for pipe flows. Over a period of time researchers from a variety of backgrounds studied multiphase flows in great detail. [Sun16] Scientists, engineers and researchers face ever increasing challenges requiring a better understanding of multiphase flow systems. Experiments and lab set-ups are the traditional means to study multiphase flows and have been used extensively by researchers and engineers. However, experiments are often expensive to conduct due to the complex apparatus required and the time required to run them [VM07]. The scale at which an experiment can be conducted is often much smaller than the application due to restrictions on the size of experimental environments. The data that can be collected in experiments is highly limited and depends on the technology used to obtain them (eg. sensors, meters etc.). The technologies are often not adequate to fully quantify flow properties. Figure 1.4 shows a multiphase flow laboratory which requires a massive amount of investment. As an alternative to experiments, researchers and scientists have turned towards numerical modelling to study flows. In this approach, established mathematical models are used to describe the flows and solved to quantify flow properties [YT19]. These governing equations are often differential equations with no analytical solution. Numerical methods can be applied to these equations to obtain approximate solutions. Numerical techniques require a number of computations to be preformed which can be done efficiently with the help of a computer. Computational fluid dynamics (CFD) is the study of fluid flows using these computational techniques [FPS02]. Domains of sizes much larger than experiments can be modelled using CFD. It can be used to obtain complex flow data at any point in the domain which cannot be easily monitored in experiments. CFD does not involve costly experimental set-ups and is therefore more cost efficient. Figure 1.3 shows the simulated result of a multiphase flow in a pipe using CFD [MMD+16]. The advancement of computer technology has led to a reliance on computational techniques to better understand and predict phenomena associated with multiphase flows. Application of computational models have gained importance due to feasibility. Modelling multiphase flows consists of treatment at different scales, knowledge of various engineering disciplines and a variety of numerical techniques.

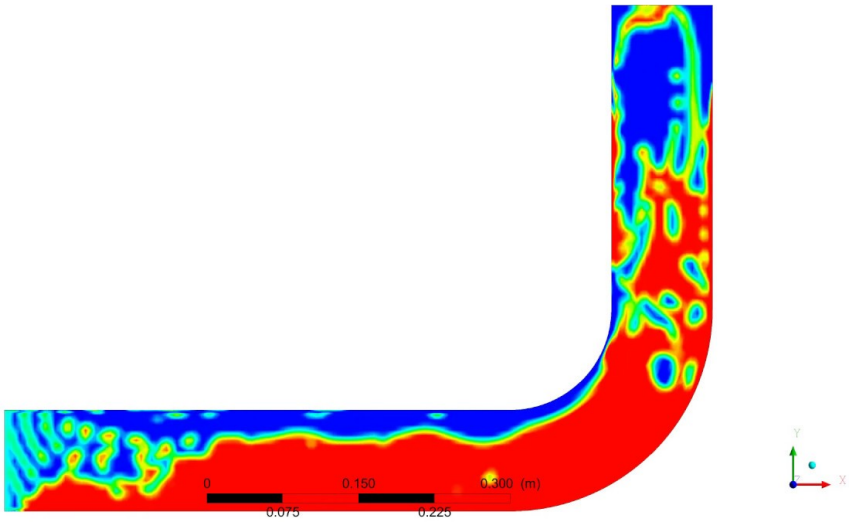

Figure 1.3: Simulation of multiphase flows using CFD

Figure 1.4: Multiphase flow lab at SINTEF

## 1.1 Motivation

The European Federation of Foundation Contractors (EFFC) and Deep Foundations Institute (DFI) conducted a joint review of problems in bored piles and diaphragm walls using tremie concrete [ED18]. Certain issues surrounding inadequate concrete mixes with inadequate workability, insufficient stability and limited robustness were identified. The sources of these problems were found to be inadequate concrete specifications and testing procedures. This review [ED18] concluded that research on designing the right concrete mix is necessary to solve these recurring problems.

Although concrete has been manufactured for centuries it is a material which is comparatively less understood. A better understanding of concrete rheology is essential to design better concrete mixes and avoid construction defects. Apart from the standard industry tests, the review proposed full-scale tests to study concrete rheology and obtain critical information. The review also realised that such tests are extremely expensive and due to a lack of technology are hard to monitor. The use of computer simulations was inevitability accepted as the only possible way to better understand fresh concrete flow. Our research group at Swansea University partnered with the EFFC-DFI joint task group to investigate the issue using simulation technology.

The homogeneous Bingham model is currently the most accepted strategy in literature to model fresh concrete flow. However, it was quickly realised that this model can only simulate certain broad aspects of concrete rheology. Concrete is a multiphase material consisting of various components and complex interactions between those constituents. Most defect causing phenomena in concrete happen due to these interactions and thus have to be captured during the simulation. There is thus a need to systematically assess the current experimental techniques to test fresh concrete mixes and the numerical models which are being used to simulate its flow. More sophisticated multiphase models are required to fully understand the mechanism behind the defect causing phenomena.

## 1.2 Aim and objectives

The broader aim of this research is to develop a model which is fully able to capture the defect causing phenomena taking place as a result of the complex interactions between the constituents of concrete. With that in mind the following objective

were identified:

1. Systematically investigate the various multiphase flow modelling techniques available in literature: Numerous methods have been researched to simulate multiphase flows and each have their strengths and weaknesses. They are also suited for different flow regimes and it is therefore imperative to study them in detail.

2. Systematically review literature related to fresh concrete testing and numerical methods used to simulate its flow: There are a number of fresh concrete tests which are regularly used in the industry to qualitatively gauge its rheological properties. Understanding the physics behind concrete rheology and these tests is crucial to solve issues related to its placement. Reviewing literature on the numerical modelling of fresh concrete will give a better idea of the challenges and short comings of existing techniques.

3. Push the existing techniques to model fresh concrete flow to their limits and use it to obtain answers to questions currently challenging the industry: Doing this will solve certain questions which the industry currently demands and also clearly highlight the shortcomings of the methods. This will in turn set the expectations on advanced models that need to be developed.

4. Investigate and develop the framework for an advanced method to simulate fresh concrete flow: This part involves using the knowledge of multiphase flow modelling and applying numerical methods to develop a framework for simulating concrete flow.

5. Apply the newly developed framework to simulate concrete flow and demonstrate its advantages over existing methods.

## 1.3 Outline of the thesis

In this work, multiphase flows are introduced and classified according to their types as seen in various applications. There are different mathematical models that can be employed to describe multiphase flows and used in suitable applications. These are introduced and discussed in detail. The strengths, weaknesses and suitability of each approach is analysed. CFD coupled with discrete element method (CFD-DEM) is an Eulerian-Lagrangian approach to model fluid-particle multiphase flows. In this method the continuum fluid phase is modelled using CFD while the particles are individually tracked using DEM. Drag models play an important role in the coupling between the CFD and DEM phase. Numerous drag models exist in literature and are all mathematically distinct from each other [NZSGM16]. This work systematically analyses and compares the performance of these models and their suitability. CFD-DEM frameworks have been validated using the fluidised bed experiment [TKT93, HKBvS96, XY97]. The experiment is chaotic in nature and is difficult to reproduce. An alternative validation test is proposed in this work which is less chaotic and much easier to reproduce. It is targeted for lower Reynolds number

flows with the hope that it can serve as a benchmark for CFD-DEM frameworks along with the fluidised bed experiment. The construction industry faces severe challenges due to defects caused during the process of placement of fresh concrete in formwork. Experiments are difficult to perform and are often extremely expensive to conduct [ED18]. The information that can be obtained using experiments is limited due to a lack of technology that can fully monitor them. As an alternative the industry has turned towards numerical modelling for answers and solutions to the problems faced during concrete placement [ED18]. This work systematically analyses the use of experiments and numerical modelling in the study of fresh concrete rheology. The various numerical techniques used in literature are classified according to certain criteria and critically discussed. The homogeneous Bingham approach towards modelling fresh concrete flow has been widely used and a consensus on its use has been reached [RG14]. The model requires the determination of two parameters, the plastic viscosity and yield stress. There is no accepted method which exists to determine the value of these parameters for a given concrete mix. This work explores a novel method to determine the Bingham parameters by using the flow diameter and flow time obtained from the slump flow and V-funnel test respectively. The homogeneous Bingham model is used to simulate tremie concrete placement in a full-scale pile foundation. Answers surrounding the general flow pattern in tremie concrete placement are sought via this approach. The limitations of this approach are also witnessed and discussed. In this work more advanced and sophisticated techniques to model multiphase flows are applied to the modelling of fresh concrete flow. The potential of these methods to model defect causing phenomena in concrete flow are explored.

## 1.4 Layout of the thesis

The layout of the rest of this work is as follows. Chapter 2 introduces multiphase flows and the various techniques to model them. Chapter 3 focuses on the CFD-DEM approach, the drag models used within its framework and a novel validation experiment. Chapter 4 reviews the experiments and numerical approaches used in studying fresh concrete rheology. In Chapter 5 the Bingham model is applied to simulate fresh concrete flow in an industrial scale problem and explore a novel method to quantify the Bingham parameters. In Chapter 6 advanced multiphase flow modelling techniques are used to simulate concrete flow and overcome the weaknesses of the homogeneous Bingham approach. Finally in Chapter 7 conclusions on this work as a whole are drawn.

# Chapter 2

# Modelling multiphase flows

Multiphase flows are witnessed regularly in many natural and technological systems. The advancement of computational technology has enabled researchers and engineers to better predict and understand multiphase flows [TSZ11]. The challenge of modelling multiphase flows is not an easy one as it involves physics at multiple scales, complex interactions and, despite the improvement in technology, limited computational resources [CST+98]. The study of this complex subject is highly multi-disciplinary and is mathematically very sophisticated. It requires a thorough understanding of the physics and methods available to solve problems in it. This work focuses on multiphase flows and forms the basis of all other discussions in subsequent chapters. It is therefore worthwhile to introduce the topic and concepts related to it. This chapter discusses from a phenomenological perspective, the physics surrounding multiphase flows. Relevant mathematical background is provided and the various computational techniques available in literature to solve the equations are discussed.

## 2.1 Introduction to multiphase flows

A multiphase flow can be defined as a flow in which two or more distinct phases are flowing simultaneously having a distinct separation at a scale well above the molecular level [YT19]. Depending on the state of phases, they may be classified according to the combination of the states eg. gas-liquid, gas-solid, liquid-solid etc. Gas-solid or gas-particle flows, depending on the particle density, may be classified as either dilute or dense [BB05]. Dilute flows are governed by forces acting on the particles by the gas. If the flow is very dilute, the particles are simply tracers which do not affect or alter the fluid flow. In dense flows, the interaction between particles becomes significant and the flow is controlled by particle-particle collisions. Liquid-solid or liquid-particle flows are mainly driven by pressure-gradient forces and since the densities of both the phases are comparable, drag forces are high. Phenomena such as sedimentation are seen in such type of flows. Gas-liquid flows could range from bubbles in liquids to liquid droplets in gas. In the first case liquid can be considered as the continuous phase while the gas is the dispersed phase. In the second case, dispersed and continuous phases can be interchanged [YT19]. Gas-liquid flows often exhibit complex interfaces such as separated and transitional

flow. The various configurations of liquid-gas flows are shown in Figure 2.1. In free surface flows there is a well defined interface and is usually associated with immiscible phases [IH10]. In the scenarios we have seen above we considered only two phases, but that can be further complicated by adding additional phases which are frequently encountered in nature and engineering applications.

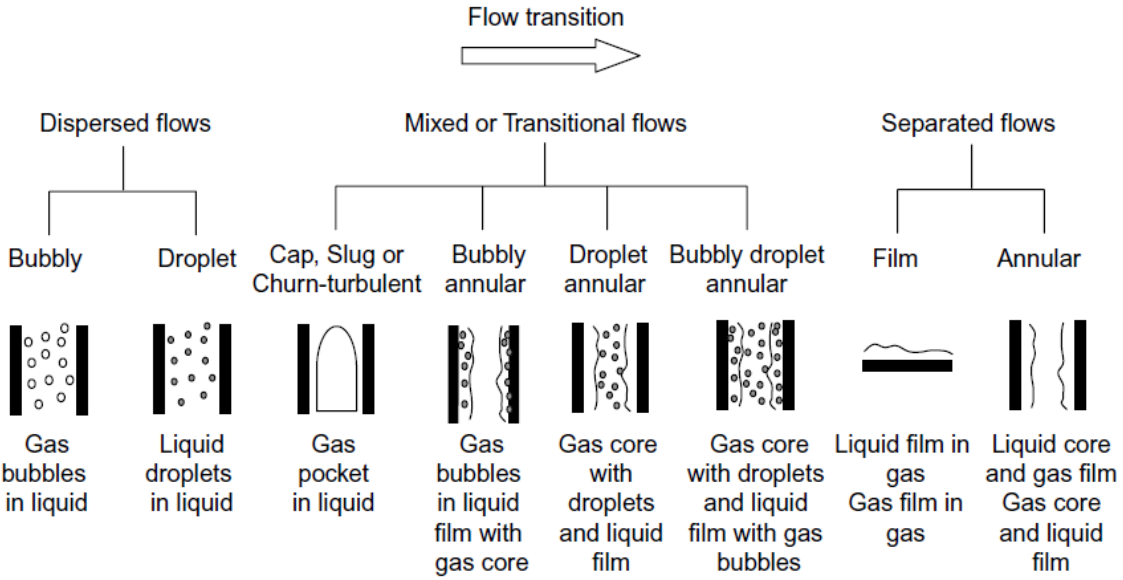

Figure 2.1: Classification of gas-liquid flows [IH10]

Gas-particle flows are found in sandstorms, volcanoes, avalanches, dust-particles in the air, smoke, dust-collectors spray drying etc. Liquid-solid flows are found in sediment transport, blood flow, slurry transportation, fluidised beds etc. Common gas-liquid flows are ocean waves, boiling water, heat exchangers etc. Liquid-liquid flows are seen in emulsifiers, fuel-cell systems etc. In all the examples mentioned above, complexities not witnessed with single phase flow, make modelling a tough task. Multiphase flows are usually multi-scale in nature [YT19]. Interaction with large structures happen on the macro-scale. Phenomena such as agglomeration and coalescence happen at the meso-scale. Motion of phases at the continuum level occur at the micro-scale.

In the next section the various approaches towards modelling multiphase flows are summarised. In the sections that follow, the approaches are mathematically introduced and briefly discussed to serve as a good starting point for the discussions detailed in the rest of this work.

## 2.2 Approaches to multiphase flow modelling

In multiphase flows, a model is required to accurately predict the behaviour of flows. Since there is usually a limitation on the scale at which a model can work at, it should be thoroughly validated using experiments [PT09]. As the computational resources become increasingly available it is more possible than ever to compute multiphase flows with more details. However, the size of problems that need to be solved and the level of detail required will, in the foreseeable future, always exceed the capacity

of these resources [YT19]. Therefore various models are developed to solve problems of varying sizes and detail level. Successful modelling of multiphase flows requires effective use of computational power and choice of technique suitable to a particular problem.

Computational fluid dynamics (CFD) has been successfully used to model single-phase flow over the years and there has been significant research on it [FPS02]. CFD can be used to reveal details that are not possible to obtain using experimental methods. It is therefore an integral part of engineering analysis and design. It naturally makes complete sense to apply the power of CFD to solve problems in multiphase flows as well [YT19]. The formulation for single-phase flows is well established in continuum mechanics and centres around the field equations describing conservation of mass, momentum and energy. Likewise, in multiphase flows similar and appropriate field equations are expected. The equations for multiphase flows are more complicated than for single phase flows owing to the complex interactions between the phases and flow characteristics[KK05]. Assumptions are made to reduce the complexity so that realistically achievable treatment is possible. Despite the discontinuous nature of the discrete phase, it has successfully been modelled as a continuous phase. Thus both phases are modelled as continua interacting and intermingling with each other [YT19]. The resulting equations closely resemble the equations for single-phase flow and the interaction is modelled by exchanging mass, momentum and energy as source terms in the conservation equations. Computational techniques similar to the ones used for single-phase flow can thus be used to solve these equations [YT19]. The main difference is the averaging procedure to characterise properties of the dispersed phase which involves specifying constitutive relationships depending largely on the classification of the flow. This approach of treating the constituent phases as inter-penetrating continua is often called the Eulerian-Eulerian approach.

For flows in which discrete particles such as bubbles, particles and drops flow in a fluid, the particles can be tracked by computing their motion and considering the appropriate forces acting on them in the Lagragian frame. Such an approach is known as the Eulerian-Lagrangian approach [YT19]. Particle trajectory is determined by solving the equation described by Newton's second law of motion through the Eulerian velocity field. The velocity field of the fluid is obtained by solving the effective momentum equation. The influence of particles on the fluid can be seen if the packing density of particles is large enough and there exists relative motion between the fluid and particles. The Eulerian-Lagrangian approach is usually more computationally intensive than the Eulerian-Eulerian approach due to the requirement of tracking the motion of a large number of particles [PT09].

The power of computers has enabled the use of mathematical models to predict and describe complex details of multiphase flow and phenomena associated with them. The most popular approach to model multiphase flows is to use CFD to solve the Navier-Stokes equations governing the motion of the phases. In order to treat the different classifications of multiphase flows we have seen, suitable modelling strategies, tailored to accommodate the variety of ways in which the phases could possibly interact, are required. The two-fluid model and trajectory models are commonly applied to different multiphase flows [BB05]. In the trajectory method,

the motion of the disperse phase is determined by tracking motion of the actual particles or an ensemble averaged representation of the particles. The particles are affected by drag and other fluid forces and could affect the trajectory of the particles. In the two-fluid model the dispersed phase is treated as an inter-penetrating continua interacting with the carrier fluid [YT19]. This approach disregards the discrete nature of the dispersed phase and approximates the effects on the carrier fluid as another fluid in the flow system. Appropriate averaging must be considered to characterise the properties of both phases. The approach of using two continua to model multiphase flows may be further treated using two different approaches. In the first approach, single-phase equations governing each of the phases are solved separately and coupled using appropriate kinematic and dynamic conditions. The second approach, known as the mixture formulation [MTK96], involves solving a single set of conservation equations by treating the different phases as a single fluid with variable properties. For a system where two fluids co-exist, the interface is implicitly determined and changes in properties are accounted for by introducing an additional transport equation for the phase indicator function.

Each of the approaches we have discussed, namely the two-fluid method, trajectory method, mixture model and free surface model is introduced in the subsequent sections. The governing equations of the two-fluid model is detailed first since it is the most complex. Discussions on the other models can be made based on the understanding of the two-fluid model.

## 2.3 Two-fluid model

In this section the basic governing equations of the two-fluid model are introduced and developed for the purpose of discussion. A more detailed derivation can be found in [YT19] The effective conservation equations are obtained and their forms which are suitable for use in CFD are also presented. The governing equations for each of the continuum phases can be obtained from the fundamental laws of physics namely conservation of mass, Newton's second law of motion for the conservation of momentum and the first law of thermodynamics for the conservation of energy. By introducing the phase indicator equation to these equations and by averaging over each phase, the equations in their averaged form are derived. For the sake of brevity $\langle \cdot \rangle$ is used to represent either volume averaging or ensemble averaging throughout the derivation. Also since incompressible flow is assumed for all applications in this work, only the mass conservation and momentum conservation equations are introduced and needed. The energy conservation is excluded from all discussion. Refer to [Ish90] for more details on the two-fluid model.

### 2.3.1 Conservation of Mass

The conservation of mass law states that *matter may neither be created or destroyed*. This basically means that mass must always be conserved. An infinitesimal element of fluid is considered as shown in Figure 2.2. The element of volume $dV$ contains any phase $k$. The rate of increase of mass within the fluid element must equal the net rate at which mass enters the elemental volume. For convenience the

Cartesian coordinate system is considered where the $k$th phase density and velocity are functions of $(x, y, z)$ and time $t$ and denoted as $\rho^k$, $u^k$, $v^k$ and $w^k$. The mass of any fluid $m^k$ is a product of the phase density and elemental volume, $\rho^k dV$ ($dV = dxdydz$). The rate of increase of mass within the fluid element is given by [YT19]

$$\frac{\partial m^k}{\partial t} = \frac{\partial \rho^k}{\partial t} dxdydz \tag{2.1}$$

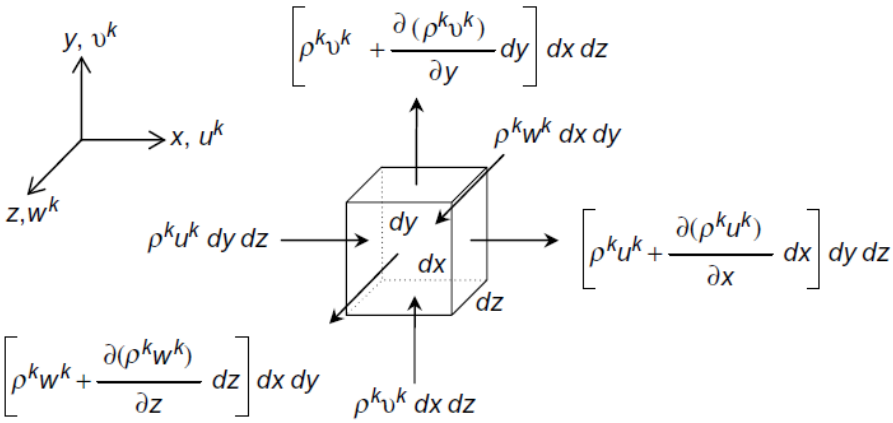

Figure 2.2: The conservation of mass based on the elemental volume [YT19]

The net rate at which mass enters the elemental volume is

$$\begin{aligned}
&\underbrace{\left(\rho^k u^k\right) dydz - \left[\left(\rho^k u^k\right) + \frac{\partial\left(\rho^k u^k\right)}{\partial x} dx\right] dydz +}_{\text{along } x} \\
&\underbrace{\left(\rho^k v^k\right) dxdz - \left[\left(\rho^k v^k\right) + \frac{\partial\left(\rho^k v^k\right)}{\partial y} dy\right] dxdz +}_{\text{along y}} \\
&\underbrace{\left(\rho^k w^k\right) dxdy - \left[\left(\rho^k w^k\right) + \frac{\partial\left(\rho^k w^k\right)}{\partial z} dz\right] dxdy}_{\text{along } z}
\end{aligned} \tag{2.2}$$

or

$$-\left[\frac{\partial\left(\rho^k u^k\right)}{\partial x} + \frac{\partial\left(\rho^k v^k\right)}{\partial y} + \frac{\partial\left(\rho^k w^k\right)}{\partial z}\right] dxdydz \tag{2.3}$$

Equating (2.1) and (2.3) we get

$$\frac{\partial \rho^k}{\partial t} = -\left[\frac{\partial\left(\rho^k u^k\right)}{\partial x} + \frac{\partial\left(\rho^k v^k\right)}{\partial y} + \frac{\partial\left(\rho^k w^k\right)}{\partial z}\right] \tag{2.4}$$

By defining $\mathbf{U}^k \equiv U_j^k \equiv \left(u^k, v^k, w^k\right)$, the above equation can be expressed in a more

compact form

$$\frac{\partial \rho^k}{\partial t} + \frac{\partial \left(\rho^k U_j^k\right)}{\partial x_j} = \frac{\partial \rho^k}{\partial t} + \nabla \cdot \left(\rho^k \mathbf{U}^k\right) = 0 \tag{2.5}$$

(2.5) represents the instantaneous equation of conservation of mass for the $k$th phase. The phase indicator function $\chi^k(x, y, z, t)$ is introduced to distinguish between the phases within the fluid flow [YT19]

$$\chi^k(x, y, z, t) = \begin{cases} 1, & \text{if } (x, y, z) \text{ is in } k \text{ th phase at time } t \\ 0, & \text{otherwise} \end{cases} \tag{2.6}$$

The time material derivative of $\chi^k \left(D\chi^k/Dt\right)$ following the interface velocity $\mathbf{U}^{int} \equiv U_j^{int} \equiv (u^{int}, v^{int}, w^{int})$ vanish as [DP99]

$$\underbrace{\frac{\partial \chi^k}{\partial t} + U_j^{int} \frac{\partial \chi^k}{\partial x_j}}_{D_{\chi_k/Dt}} = \underbrace{\frac{\partial \chi^k}{\partial t} + \mathbf{U}^{int} \cdot \nabla \chi^k}_{D_{\chi_k}/Dt} = 0 \tag{2.7}$$

The averaged form of the conservation of mass equation can be obtained by multiplying (2.5) by $\chi^k$

$$\chi^k \frac{\partial \rho^k}{\partial t} + \chi^k \nabla \cdot \left(\rho^k \mathbf{U}^k\right) = 0 \tag{2.8}$$

On the basis of (2.7) and the following identities

$$\chi^k \frac{\partial \rho^k}{\partial t} = \frac{\partial \left(\rho^k \chi^k\right)}{\partial t} - \rho^k \frac{\partial \chi^k}{\partial t} = \frac{\partial \left(\rho^k \chi^k\right)}{\partial t} + \rho^k \mathbf{U}^{int} \cdot \nabla \chi^k \tag{2.9}$$

and

$$\chi^k \nabla \cdot \left(\rho^k \mathbf{U}^k\right) = \nabla \cdot \left(\chi^k \rho^k \mathbf{U}^k\right) - \rho^k \mathbf{U}^k \cdot \nabla \chi^k \tag{2.10}$$

we get

$$\frac{\partial \left(\chi^k \rho^k\right)}{\partial t} + \nabla \cdot \left(\chi^k \rho^k \mathbf{U}^k\right) = \rho^k \left(\mathbf{U}^k - \mathbf{U}^{int}\right) \cdot \nabla \chi^k \tag{2.11}$$

The averaging procedure is assumed to follow the following rules

$$\langle \langle a \rangle \rangle = \langle a \rangle \tag{2.12}$$

$$\langle a + b \rangle = \langle a \rangle + \langle b \rangle \tag{2.13}$$

$$\langle \langle a \rangle b \rangle = \langle a \rangle \langle b \rangle \tag{2.14}$$

$$\left\langle \frac{\partial a}{\partial t} \right\rangle = \frac{\partial \langle a \rangle}{\partial t} \tag{2.15}$$

$$\left\langle \frac{\partial a}{\partial x_j} \right\rangle = \frac{\partial \langle a \rangle}{\partial x_j} = \nabla \langle a \rangle \tag{2.16}$$

The above are the Reynolds, Leibnitz and Gauss rules of averaging a field $\phi$ [LD88]. Using them the instantaneous averaged equation for the conservation of mass can be written as

$$\begin{aligned} &\left\langle \frac{\partial \left(\chi^k \rho^k\right)}{\partial t} \right\rangle + \left\langle \nabla \cdot \left(\chi^k \rho^k \mathbf{U}^k\right) \right\rangle = \left\langle \rho^k \left(\mathbf{U}^k - \mathbf{U}^{int}\right) \cdot \nabla \chi^k \right\rangle \\ &\Rightarrow \frac{\partial \left\langle \chi^k \rho^k \right\rangle}{\partial t} + \nabla \cdot \left\langle \chi^k \rho^k \mathbf{U}^k \right\rangle = \underbrace{\left\langle \rho^k \left(\mathbf{U}^k - \mathbf{U}^{int}\right) \cdot \nabla \chi^k \right\rangle}_{\Gamma^k} \end{aligned} \tag{2.17}$$

The right hand term of the above equation represents the inter-facial mass source.

### 2.3.2 Conservation of Momentum

For the derivation of the conservation of momentum equation, the concept of material derivative is applied. For any field $\phi$, the conservative form can be written as [YT19]

$$\frac{\partial \left(\rho^k \phi\right)}{\partial t} + \frac{\partial \left(\rho^k U_j^k \phi\right)}{\partial x_j} = 0 \tag{2.18}$$

By applying the chain rule we get

$$\frac{\partial \left(\rho^k \phi\right)}{\partial t} + \frac{\partial \left(\rho^k U_j^k \phi\right)}{\partial x_j} = \rho^k \underbrace{[\frac{\partial \phi}{\partial t} + U_j^k \frac{\partial \phi}{\partial x_j}]}_{D\phi/Dt} + \phi \underbrace{\left( \frac{\partial \rho^k}{\partial t} + \frac{\partial \left(\rho^k U_j^k\right)}{\partial x_j} \right)}_{=0} \tag{2.19}$$

This equation represents the non-conservative form of the rate of change of $\phi$ per unit volume. This non-conservative form is applied to obtain the momentum equation. To derive the instantaneous momentum conservation equation for the $k$th phase the same fluid element of volume $dV$ is considered. Newton's second law of motion states that the rate of increase of momentum of the fluid element is equal to the sum of forces acting on that fluid element. For incompressible flow, the $x$ component of Newton's second law of motion can be expressed as

$$m^k a_x^k = \sum F_x^k \tag{2.20}$$

where $F_x^k$ and $a_x^k$ are the force and acceleration along the $x$ direction. The acceleration is simply the rate of change of $u^k$ which is given by

$$a_x^k = \frac{Du^k}{Dt} \tag{2.21}$$

Given that we are only considering incompressible flow, the rate of increase of momentum in the $x$ direction is simply

$$\rho^k \frac{Du^k}{Dt} dxdydz \tag{2.22}$$

The sum of forces on the fluid element consists of two sources: surface forces and body forces and are included in the momentum equation as source terms. From Figure 2.3 the surface forces for the component of velocity in the $x$ direction are due to normal stress $\sigma^k_{xx}$ and tangential forces $\tau^k_{yx}$ and $\tau^k_{zx}$. The total net force per unit volume along the $x$ direction is

$$\left[\frac{\partial \sigma^k_{xx}}{\partial x} + \frac{\partial \tau^k_{yx}}{\partial y} + \frac{\partial \tau^k_{2x}}{\partial z}\right] dxdydz \tag{2.23}$$

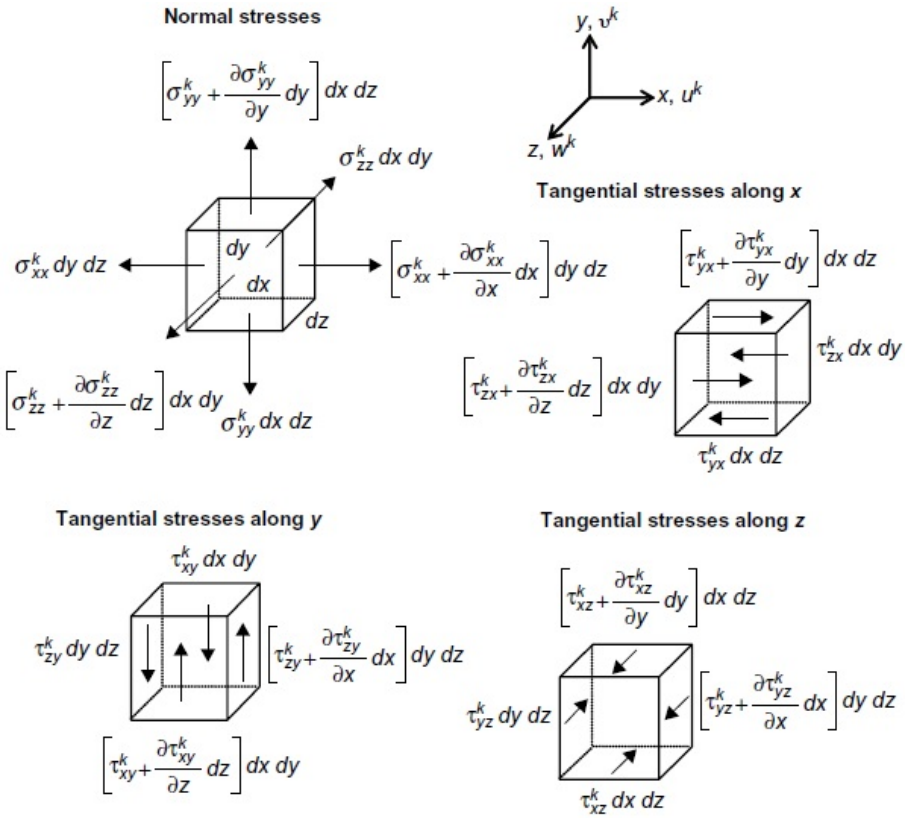


Figure 2.3: The conservation of momentum based on the elemental volume [YT19]

The total net forces on per unit volume in $y$ and $z$ directions can be likewise derived as

$$\left[\frac{\partial \tau^k_{xy}}{\partial x} + \frac{\partial \sigma^k_{yy}}{\partial y} + \frac{\partial \tau^k_{zy}}{\partial z}\right] dxdydz \tag{2.24}$$

$$\left[\frac{\partial \tau^k_{xz}}{\partial x} + \frac{\partial \tau^k_{yz}}{\partial y} + \frac{\partial \sigma^k_{zz}}{\partial z}\right] dxdydz \tag{2.25}$$

Combining 2.23 with 2.22, the X-momentum conservation equation can be written as

$$\rho^k \frac{Du^k}{Dt} dxdydz = \left[ \frac{\partial \sigma^k_{xx}}{\partial x} + \frac{\partial \tau^k_{yx}}{\partial y} + \frac{\partial \tau^k_{zx}}{\partial z} + \sum F^{k,body\ \text{forces}}_x \right] dxdydz$$
$$\Rightarrow \rho^k \frac{Du^k}{Dt} = \frac{\partial \sigma^k_{xx}}{\partial x} + \frac{\partial \tau^k_{yx}}{\partial y} + \frac{\partial \tau^k_{zx}}{\partial z} + \sum F^{k,body\ \text{forces}}_x \tag{2.26}$$

Similar equations for the Y-momentum and Z-momentum can be derived

$$\rho^k \frac{Dv^k}{Dt} = \frac{\partial \tau^k_{xy}}{\partial x} + \frac{\partial \sigma^k_{yy}}{\partial y} + \frac{\partial \tau^k_{zy}}{\partial z} + \sum F^{k,body\ \text{forces}}_y \tag{2.27}$$

$$\rho^k \frac{Dw^k}{Dt} = \frac{\partial \tau^k_{xz}}{\partial x} + \frac{\partial \tau^k_{yz}}{\partial y} + \frac{\partial \sigma^k_{zz}}{\partial z} + \sum F^{k,body\ \text{forces}}_z \tag{2.28}$$

If $\mathbf{T}^k \equiv \left(\sigma^k_{xx}, \tau^k_{xy}, \ldots, \tau^k_{yz}, \sigma^k_{zz}\right)$ is the Cauchy stress tensor and $\sum \mathrm{F}^{k,\text{body forces}} \equiv \left(\sum F^{k,body\ \text{forces}}_x, \sum F^{k,body\ \text{forces}}_y, \sum F^{k,body\ \text{forces}}_z\right)$, the conservation momentum equation can be written in the compact form as

$$\rho^k \frac{\partial \mathbf{U}^k}{\partial t} + \rho^k \mathbf{U}^k \cdot \nabla \mathbf{U}^k = \nabla \cdot \mathbf{T}^k + \sum \mathbf{F}^{k,\text{body forces}} \tag{2.29}$$

It is customary to write $\mathbf{T}^k$ in terms of pressure and extra stresses. Describing normal stress relationships for $\sigma^k_{xx}$, $\sigma^k_{yy}$ and $\sigma^k_{zz}$ in terms of $k$th phase pressure $p^k$ and normal viscous stress components $\tau^k_{xx}$, $\tau^k_{yy}$ and $\tau^k_{zz}$ acting perpendicular to the control volume

$$\sigma^k_{xx} = -p^k + \tau^k_{xx} \quad \sigma^k_{yy} = -p^k + \tau^k_{yy} \quad \sigma^k_{zz} = -p^k + \tau^k_{zz} \tag{2.30}$$

The conservation of momentum equation can be written as

$$\rho^k \frac{\partial \mathbf{U}^k}{\partial t} + \rho^k \mathbf{U}^k \cdot \nabla \mathbf{U}^k = -\nabla p^k + \nabla \cdot \tau^k + \sum \mathbf{F}^{k,\text{body forces}} \tag{2.31}$$

where $\tau^k$ denotes the extra stresses, ($\tau^k \equiv \left(\tau^k_{xx}, \tau^k_{xy}, \ldots, \tau^k_{yz}, \tau^k_{zz}\right)$)
The averaged equations is obtained by multiplying the above equation by the phase indicator function and then applying Reynolds, Leibnitz and Gauss rules [LD88]

$$\frac{\partial \left\langle \chi^k \rho^k \mathrm{U}^k \right\rangle}{\partial t} + \nabla \cdot \left\langle \chi^k \rho^k \mathrm{U}^k \otimes \mathrm{U}^k \right\rangle = -\nabla \left\langle \chi^k p^k \right\rangle + \nabla \cdot \left\langle \chi^k \tau^k \right\rangle + \left\langle \chi^k \right\rangle \left\langle \sum \mathrm{F}^{k,\text{body forces}} \right\rangle$$
$$+ \underbrace{\left\langle \rho^k \mathrm{U}^k \left(\mathbf{U}^k - \mathrm{U}^{int}\right) \cdot \nabla \chi^k \right\rangle + \left\langle p^k \right\rangle \left\langle \nabla \chi^k \right\rangle - \left\langle \tau^k \cdot \nabla \chi^k \right\rangle}_{\Omega^k} \tag{2.32}$$

The last three terms on the right hand side of the above equation represent the inter-facial momentum sources.

### 2.3.3 Effective equations

The averaged equations of conservation of mass and momentum in the previous section cannot be solved directly since they involve average of products and local

variables. One approach is to reduce the averages of products to product of averages and separate out the mean flow from the fluctuations. In multiphase flow Favre-averaging technique is preferred. Two types of averages are used, namely the phase-weighted average and the mass-weighted average. The phase-weighted average on variable $\phi$ is given by

$$\overline{\langle\varphi\rangle} = \frac{\overline{\langle\chi^k\varphi\rangle}}{\langle\chi^k\rangle} \tag{2.33}$$

and the mass-weighted average of variable $\psi$ is given by

$$\overline{\langle\psi\rangle} = \frac{\overline{\langle\rho^k\psi\rangle}}{\overline{\langle\rho^k\rangle}} \tag{2.34}$$

The instantaneous averaged variables of $\phi$ and $\psi$ may be written as

$$\langle\varphi\rangle = \overline{\langle\varphi\rangle} + \varphi'' \tag{2.35}$$

$$\langle\psi\rangle = \overline{\langle\psi\rangle} + \psi'' \tag{2.36}$$

where $\varphi''$ and $\psi''$ are superimposed fluctuations. By multiplying the first equation from the two above by the averaged phase indicator function and the second equation by the averaged density we get

$$\left\langle\chi^k\varphi\right\rangle = \left\langle\chi^k\right\rangle\overline{\langle\varphi\rangle} + \left\langle\chi^k\right\rangle\varphi'' \tag{2.37}$$

$$\left\langle\rho^k\psi\right\rangle = \left\langle\rho^k\overline{X\psi\rangle} + \left\langle\rho^k\right\rangle\psi'' \right. \tag{2.38}$$

By time-averaging the equations

$$\overline{\langle\chi^k\varphi\rangle} = \overline{\langle\chi^k\rangle\,\overline{\langle\varphi\rangle}} + \overline{\langle\chi^k\rangle\,\varphi''} \tag{2.39}$$

$$\overline{\langle\rho^k\psi\rangle} = \overline{\langle\rho^k\rangle\langle\psi\rangle} + \overline{\langle\rho^k\rangle\,\psi''} \tag{2.40}$$

It follows that

$$\left\langle\overline{\chi^k\rangle\,\varphi''} = 0 \right. \tag{2.41}$$

$$\overline{\langle\rho^k\rangle\,\psi''} = 0 \tag{2.42}$$

The local volume fraction is an important parameter in multiphase flow. It is defined as a fraction of time in which a particular phase occupies a particular point in space. The local volume fraction can be considered to be the ratio of the fractional volume $V_k$ of the $k$th phase in a volume of $V$. It is the same as the volume average of the phase indicator function $\alpha^k = V_k/V = \left\langle\chi^k\right\rangle$. The effective governing equations written in terms of local volume fraction and product of the averages are
Conservation of mass:

$$\frac{\partial\left(\alpha^k\rho^k\right)}{\partial t}+\nabla\cdot\left(\alpha^k\rho^k\mathbf{U}^k\right)=\Gamma'^k \tag{2.43}$$

Conservation of momentum:

$$\begin{aligned}\frac{\partial\left(\alpha^k\rho^k\mathbf{U}^k\right)}{\partial t}+\nabla\cdot\left(\alpha^k\rho^k\mathbf{U}^k\otimes\mathbf{U}^k\right)&=-\alpha^k\nabla p^k-p^k\nabla\alpha^k\\&+\nabla\cdot\left(\alpha^k\tau^k\right)-\nabla\cdot\left(\alpha^k\tau^{k''}\right)+\alpha^k\sum\mathbf{F}^{k,body\text{ forces}}+\Omega'^k\end{aligned} \tag{2.44}$$

In the above equations inter-facial terms $\Gamma'^k$ and $\Omega'^k$ represent the Favre-averaging that is performed on the volume-averaged terms $\Gamma^k$ and $\Omega^k$.

The governing equations derived in the previous section, if solved directly, is known as the two-fluid model. There is no closed-form solution to these equations and they have to be solved using numerical techniques. The equations are very similar to their single-phase counterparts, the only noticeable difference being the addition of the volume fraction to the terms and the sources/sinks to account for the inter-phase interaction. The success of the two fluid model depends upon using suitable constitutive equations for the inter-facial terms $\Gamma'^k$ and $\Omega'^k$. There exists no universally applicable model which applies to all topologies and flow patterns. The most common assumption applied in most calculations is that all the phases share the same pressure $p^k = p$.

Now that the two-fluid model has been established we can look at special cases where further simplifications can be made in the following sections. These are based on the governing equations we have developed in this section.

## 2.4 Mixture model

For the special case where the relative behaviour of phases can be prescribed a priori, the mixture formulation may be attained by adding all the phase conservation equations together. The dynamic interaction between the phases does not happen since the inter-facial terms are omitted from the formulation. A more detailed derivation can be found in [YT19, MTK96]. The problem is simplified and the equations look like

Conservation of mass:

$$\frac{\partial\rho^m}{\partial t}+\nabla\cdot\left(\rho^m\mathbf{U}^m\right)=0 \tag{2.45}$$

Conservation of momentum:

$$\begin{aligned}\frac{\partial\left(\rho^m H^m\right)}{\partial t}+\nabla\cdot\left(\rho^m\mathbf{U}^m H^m\right)&=\nabla\cdot\left(\lambda^m\nabla T^m\right)-\nabla\cdot\mathbf{q}_H^{m\prime}+\zeta\\&-\nabla\cdot\sum_{k=1}^{2}\left(\alpha^k\rho^k\mathbf{U}^{dr,k}H^k\right)\end{aligned} \tag{2.46}$$

All the phases are assumed to share the same value for pressure. The mixture density and viscosity are evaluated as

$$\rho^m = \sum_{k=1}^{2} \alpha^k \rho^k, \quad \mu^m = \sum_{k=1}^{2} \alpha^k \mu^k \tag{2.47}$$

The model treats the mixture velocity as a combination of phase-weighted and mass-weighted variables

$$\mathbf{U}^m = \frac{\sum_{k=1}^{2} \alpha^k \rho^k \mathbf{U}^k}{\sum_{k=1}^{2} \alpha^k \rho^k} \tag{2.48}$$

In the equations above the drift velocity is given by $\mathrm{U}^{dr,k} = \mathrm{U}^k - \mathrm{U}^m$. In the absence of surface tension effects the terms $\mathrm{F}_\sigma$ and $\zeta$ can be neglected. The omission of these terms essentially makes the equations single-phase equations.

The volume fractions are distinct in the mixture model. Once the continuous phase volume fraction is determined, the disperse phase volume fraction can be obtained from the algebraic constraint $\sum_{k=1}^{2} \alpha^k = 1$. If further simplification is applied assuming that the phase velocities are equivalent, the mixture model reduces to the homogeneous model.

## 2.5 Free surface flow model

Free surface flows are flows in which the phases have distinct interfaces between them. The phases are usually assumed to have different fluid properties. Such type of flows are characterised by fluid which have large differences in density eg. gas and liquid. For this class of multiphase flows, the free surface introduces added complexities. Free surfaces require special methods to determine their location and motion. Many numerical methods have been proposed to solve for the interfaces in free surface flows. Lagrangian methods can be used when the deformations are not that big. However, Eulerian methods are preferred as they permit large topological changes and allow discontinuities.

In this section two phases are considered and both of them are assumed to be incompressible. A more detailed derivation can be found in [YT19]. As we have seen in the previous section equations for the homogeneous formulation are

Mass:

$$\frac{\partial \rho^m}{\partial t} + \frac{\partial \left(\rho^m u^m\right)}{\partial x} + \frac{\partial \left(\rho^m v^m\right)}{\partial y} + \frac{\partial \left(\rho^m w^m\right)}{\partial z} = 0 \tag{2.49}$$

x-Momentum:

$$\begin{aligned}\frac{\partial\left(\rho^m u^m\right)}{\partial t}+&\frac{\partial\left(\rho^m u^m u^m\right)}{\partial x}+\frac{\partial\left(\rho^m v^m u^m\right)}{\partial y}+\frac{\partial\left(\rho^m w^m u^m\right)}{\partial z}\\ =&\frac{\partial}{\partial x}\left[\left(\mu^m+\mu_T^m\right)\frac{\partial u^m}{\partial x}\right]+\frac{\partial}{\partial y}\left[\left(\mu^m+\mu_T^m\right)\frac{\partial u^m}{\partial y}\right]\\ &+\frac{\partial}{\partial z}\left[\left(\mu^m+\mu_T^m\right)\frac{\partial u^m}{\partial z}\right]+S_{u^m}\end{aligned} \tag{2.50}$$

y-Momentum:

$$\begin{aligned}\frac{\partial\left(\rho^m v^m\right)}{\partial t}+&\frac{\partial\left(\rho^m u^m v^m\right)}{\partial x}+\frac{\partial\left(\rho^m v^m v^m\right)}{\partial y}+\frac{\partial\left(\rho^m w^m v^m\right)}{\partial z}\\ =&\frac{\partial}{\partial x}\left[\left(\mu^m+\mu_T^m\right)\frac{\partial v^m}{\partial x}\right]+\frac{\partial}{\partial y}\left[\left(\mu^m+\mu_T^m\right)\frac{\partial v^m}{\partial y}\right]\\ &+\frac{\partial}{\partial z}\mid\left(\mu^m+\mu_T^m\right)\frac{\partial v^m}{\partial z}\Bigg]+S_{v^m}\end{aligned} \tag{2.51}$$

z-Momentum:

$$\begin{aligned}\frac{\partial\left(\rho^m w^m\right)}{\partial t}+&\frac{\partial\left(\rho^m u^m w^m\right)}{\partial x}+\frac{\partial\left(\rho^m v^m w^m\right)}{\partial y}+\frac{\partial\left(\rho^m w^m w^m\right)}{\partial z}\\ =&\frac{\partial}{\partial x}\left[\left(\mu^m+\mu_T^m\right)\frac{\partial w^m}{\partial x}\right]+\frac{\partial}{\partial y}\left[\left(\mu^m+\mu_T^m\right)\frac{\partial w^m}{\partial y}\right]\\ &+\frac{\partial}{\partial z}\left[\left(\mu^m+\mu_T^m\right)\frac{\partial w^m}{\partial z}\right]+S_{w^n}\end{aligned} \tag{2.52}$$

The source and sink terms are given as

$$\begin{aligned}S_{u^m}=&-\frac{\partial p''}{\partial x}+\frac{\partial}{\partial x}\left[\left(\mu^m+\mu_T^m\right)\frac{\partial u^m}{\partial x}\right]+\frac{\partial}{\partial y}\left[\left(\mu^m+\mu_T^m\right)\frac{\partial v^m}{\partial x}\right]\\ &+\frac{\partial}{\partial z}\left[\left(\mu^m+\mu_T^m\right)\frac{\partial w^m}{\partial x}\right]+\left(\rho^m-\rho^{ref}\right)g_x+F_{\sigma,x}\end{aligned} \tag{2.53}$$

$$\begin{aligned}S_{v^m}=&-\frac{\partial p''}{\partial y}+\frac{\partial}{\partial x}\left[\left(\mu^m+\mu_T^m\right)\frac{\partial u^m}{\partial y}\right]+\frac{\partial}{\partial y}\left[\left(\mu^m+\mu_T^m\right)\frac{\partial v^m}{\partial y}\right]\\ &+\frac{\partial}{\partial z}\left[\left(\mu^m+\mu_T^m\right)\frac{\partial w^m}{\partial y}\right]+\left(\rho^m-\rho^{ref}\right)g_y+F_{\sigma,y}\end{aligned} \tag{2.54}$$

$$\begin{aligned}S_{w^m}=&-\frac{\partial p''}{\partial z}+\frac{\partial}{\partial x}\left[\left(\mu^m+\mu_T^m\right)\frac{\partial u^m}{\partial z}\right]+\frac{\partial}{\partial y}\left[\left(\mu^m+\mu_T^m\right)\frac{\partial v^m}{\partial z}\right]\\ &+\frac{\partial}{\partial z}\left[\left(\mu^m+\mu_T^m\right)\frac{\partial w^m}{\partial z}\right]+\left(\rho^m-\rho^{ref}\right)g_z+F_{\sigma,z}\end{aligned} \tag{2.55}$$

The effects of buoyancy and surface tension have been included in the equations above. The modified averaged pressure is given by $p''=p+\frac{2}{3}\rho^m k^m+\frac{2}{3}\left(\mu^m+\mu_T^m\right)\nabla\cdot\mathbf{U}^m-\rho^{nf}g_i x_i$ where $\rho^{ref}$ is the reference density. The mixture density and viscosity can be determined based on linear dependence of some characteristic function C

$$\begin{aligned}\rho^m &= (1-C)\rho^g + C\rho^l \\ \mu^m &= (1-C)\mu^g + C\mu^I\end{aligned} \tag{2.56}$$

where $l$ and $g$ indicate the liquid and gas phases respectively. A phase indicator function is introduced to track the interface between the phases in the computational domain. In the volume of fluid (VOF) [HN81], method equation for the volume fraction of the liquid phase is given by

$$\frac{\partial \alpha^l}{\partial t} + \frac{\partial \left(u^m \alpha^l\right)}{\partial x} + \frac{\partial \left(v^m \alpha^l\right)}{\partial y} + \frac{\partial \left(w^m \alpha^l\right)}{\partial z} = \alpha^l \left[\frac{\partial u^m}{\partial x} + \frac{\partial v^m}{\partial y} + \frac{\partial w^m}{\partial z}\right] \tag{2.57}$$

The characteristic function $C$ is given by the volume fraction $\alpha^l$. Methods based on VOF guarantee conservation of mass. Successful VOF approaches rely on appropriate evaluation of fluxes in the advection term predicting the shape of the interface.

## 2.6 Trajectory model

As an alternative to the Eulerian-Eulerian approach the disperse phase can be handled differently in the Eulerian-Lagrangian approach. In this approach there is a coupling between a Eulerian field for the solution of motion of the surrounding fluid and a Lagrangian scheme for tracking the motion of individual particles. The Eulerian part of this approach involves solving the Navier-Stokes equations for the surrounding fluid while particles are tracked individually through a Lagrangian model. The interaction of particles with the continuous phase are represented by adding sources/sinks to the equations.

For a detailed derivation please refer to [YT19, **?**, CST+98]. To determine the motion of a particle, the momentum equation can be deduced from Newton's second law of motion as

$$\underbrace{\rho^p V_p}_{m_p} \frac{D\mathbf{V}^p_{ins}}{Dt} = \underbrace{S_{\mathbf{V}^p}}_{\sum \mathbf{F}} \tag{2.58}$$

where $m_p$ is the mass, $\rho^p$ the density, $V_p$ the volume and $\mathbf{V}^p_{ins}$ the instantaneous velocity of the particle. The left hand side of the equation is the Lagragian time derivative following the particle while on the right hand side the source term $S_{\mathrm{V}^p}$ represents the sum of forces acting on a particle. These forces include those that act due to motion of the particle and those that act on the particle due to the motion of the surrounding fluid. The forces that act on a particle include drag, virtual mass, Basset, Magnus, lift, body, buoyancy and pressure gradient forces.

The mathematical expressions for the relevant forces have been introduced here Drag force:

$$\mathbf{F}_{\mathrm{Drag}} = \frac{\pi}{8}\rho^f d_p^2 C_D \left(\mathbf{V}^f_{\mathrm{ins}} - \mathbf{V}^p_{\mathrm{ins}}\right)\left|\mathbf{V}^f_{\mathrm{ins}} - \mathbf{V}^p_{ins}\right| \tag{2.59}$$

Added mass force:

$$\mathbf{F}_{\text{Added}} = K_A \rho^f V_p \frac{d\left(\mathbf{V}^f_{\text{ins}} - \mathbf{V}^p_{\text{ins}}\right)}{dt} \tag{2.60}$$

Basset history force:

$$\mathbf{F}_{\text{Basset}} = K_B d_p^2 \sqrt{\pi \rho_f \mu_f} \int_{t_0}^{t} \frac{d\left(\mathbf{V}^f_{\text{ins}} - \mathbf{V}^p_{\text{ins}}\right)}{dt} \frac{ds}{\sqrt{t-s}} \tag{2.61}$$

Magnus force:

$$\mathbf{F}_{\text{Magnus}} = \frac{\pi}{8} \rho^f d_p^3 \omega_p e_{ijk} n_{1;j} \left(\mathbf{V}^f_{ins} - \mathbf{V}^p_{ins}\right) \tag{2.62}$$

Saffman lift force:

$$\mathbf{F}_{Lift} = K_L \mu^f d_p^2 \left(\mathbf{V}^f_{ins} - \mathbf{V}^p_{ins}\right) \sqrt{\frac{\rho^f G}{\mu^f}} \tag{2.63}$$

Body gravity force:

$$\mathbf{F}_{\text{Body}} = \rho^p V_p \mathbf{g} \tag{2.64}$$

Buoyancy force:

$$\mathbf{F} = -\rho^f V_p \mathbf{g} \tag{2.65}$$

Pressure gradient force:

$$\mathbf{F}_{\text{Pressure}} = -\rho^f V_p \frac{D\mathbf{V}^f_{\text{ins}}}{Dt} \tag{2.66}$$

Now that we have seen the various methodologies that exist to model multiphase flows, it is important to understand the advantages and disadvantages of each. The next section discusses the suitability of each of the methods that have been introduced so that we can make appropriate choices based on the application.

## 2.7 Suitability of multiphase models

In order to choose an appropriate model for the application to be modelled, it is important to determine which regime the flow belongs in. This provides a broad guideline for the degree of coupling involved and appropriate modelling for that regime. As we have seen the approaches can be divided into Euler-Lagrange approach and the Eulerian-Eulerian approach.

### 2.7.1 Eulerian-Eulerian approach

In this approach the different phases are treated mathematically as inter-penetrating continua. Since volume of one phase cannot occupy the other phase, the concept

of volume fraction is introduced. Volume fractions are assumed to be functions of time and space and their sum is always equal to unity. The conservation equations are derived for each phase and all phases have similar structure. These equations are closed by constitutive relationships which are given by empirical formulae. The Eulerian-Eulerian approaches we have seen so far are the free-surface volume of fluid (VOF) model, the mixture model and the two-fluid model.

#### 2.7.1.1 Free surface VOF model

In this model a surface-tracking technique is applied to the Eulerian phases. It is designed for two or more immiscible fluids where the position of the interface between the phases is of importance [F$^+$11, YT19, PT09, CST$^+$98]. In this model a single set of momentum equations is shared by all the phases and the volume fraction is tracked throughout the domain. Applications of this method are stratified flow, free surface flows, sloshing, movement of large bubbles, dam break, jet etc.

#### 2.7.1.2 Mixture model

This model is designed for two or more phases. Since it is an Eulerian-Eulerian approach the phases are treated as inter-penetrating continua. The mixture momentum equation is solved and relative velocities are prescribed to the phases. Applications of this model include particle-laden flows, bubbly flow, sedimentation and cyclone separators [F$^+$11, YT19, PT09, CST$^+$98]. If the mixture model is used without the relative velocities, it reduces to the homogeneous model.

#### 2.7.1.3 Two-fluid model

This is the most complex model. It has a momentum and continuity equation for each phase. Coupling is done through interphase exchange coefficients. The coupling highly depends upon the type of phases involved. For example fluid-solid flow is handled differently from fluid-fluid flow [F$^+$11, YT19, PT09, CST$^+$98]. The momentum exchange depends upon the type of mixture involved. This model is used in bubble columns, risers, particle suspensions and fluidised beds.

#### 2.7.1.4 Choosing between the Eulerian-Eulerian models

To choose the appropriate model, we have to first select the aspect of the flow which is of most interest. Bubbly or droplet flows in which the phases mix might be solved using either the mixture or two-fluid model. Slug flows or stratified flows may be solved using the VOF model. Fluidised beds are best modelled using the two-fluid model. Another thing to consider while choosing a model is the computational time. Since the mixture model and free surface models have only one set of continuity and momentum equations to be solved, they are usually computationally more efficient than the two-fluid model where a set of continuity and momentum equations is solved for each phase. If there is a wide distribution of the dispersed phase and the particles do not separate from the primary flow field the mixture model could be preferred. If the dispersed phase is concentrated in certain positions of the domain, the two-fluid model should be preferred. Another thing to keep in mind is the

level of accuracy required along with the stability. In general the two-fluid model is more accurate than the mixture model. The two-fluid model is less stable than the mixture model [F$^+$11, YT19, PT09, CST$^+$98].

### 2.7.2 Eulerian-Lagrangian approach

In this approach the fluid phase is treated as a continuum by solving the Navier-Stokes equations for it, while the dispersed phase is solved by tracking a large number of particles, droplets or bubbles in the flow domain. The dispersed phase can exchange mass, momentum and energy with the continuous phase. The particle trajectories are computed individually at specific intervals during the fluid phase calculation. The model is suitable for modelling spray dryers, coal and liquid fuel combustion and other particle laden flows. This model is not meant for liquid-liquid mixtures. This model is extremely useful if the particle position is of importance since it can provide details of the motion of the particles. However, if the number of particles in the system is large, this method can be computationally very expensive as the position of each particle is individually calculated [F$^+$11, YT19, PT09, CST$^+$98].

## 2.8 Conclusion

In this chapter we have seen the various approaches towards modelling multiphase flows. The governing equations have been either derived or introduced to give an idea of the techniques available at our disposal. Each approach has its specific use and are designed for different applications. Each also have their limitations based on level of detail, accuracy, stability and speed of computation. We must select the best suited model for our purpose. In the following chapters discussions will ensue based on the preface given in this chapter. Certain models will be looked at again and others applied to specific industrial applications. In the next chapter we focus on a particular Eulerian-Lagrangian technique known as CFD-DEM (CFD coupled with the discrete element method). The chapter proposes a new method to validate CFD-DEM frameworks which could be used as a benchmark. The lack of a proper assessment of drag models used in CFD-DEM is also addressed.

# Chapter 3

# CFD-DEM, drag models and experimental validation

In the previous chapter multiphase flows along with the various classes were introduced. Mathematical models suited for different cases and applications were derived. The approaches can broadly be classified as Eulerian-Eulerian and Eulerian-Lagrangian. In this chapter we focus on the CFD-DEM method which can be classified as an Eulerian-Lagrangian approach. Computational fluid dynamics coupled with discrete element method (CFD-DEM) has been increasingly used over the last three decades to simulate particle-laden flow encountered in nature and industry, such as sand storm, debris flow, combustion, steelmaking and injection moulding. An important technical foundation for CFD-DEM simulation is the drag model, in that the drag force along with pressure-gradient forces often dominate particle-laden flows. Various drag models have been proposed in the literature and are widely used in academic and commercial CFD-DEM codes. These drag models differ greatly in formulation, but independent assessments for their performance in different physical conditions are rare in the literature, raising questions to their suitability in specific practical applications. This chapter presents a systematic evaluation of commonly-used drag models. This is achieved by using a carefully validated in-house code and through a series of comparisons with phenomenological formulations and other well-established numerical codes under specially designed testing configurations. In addition, a new *cross-flow sedimentation* validation test is also introduced for the performance evaluation of CFD-DEM simulation. Designed for the low Reynolds number regime, the new benchmark experiment is convenient for implementation and quantification, and it serves as a complement to the widely used fluidised bed experiment for CFD-DEM validation.

## 3.1 Introduction

CFD can be used to model fluid and particulate phases using the Eulerian-Eulerian approach in which both, are treated as inter-penetrating continua. The assumption of fluid being a continuum is standard and has been successfully used to model flow over the last several decades. However, the assumption is less accurate for the particulate phase and significant detail, especially at the scale of particles, is

lost in the process. On the contrary, CFD-DEM has been developed to accurately model particle motion. A Lagrangian approach, DEM, is used to track particles in space and time while retaining the Eulerian approach of modelling the fluid flow. CFD-DEM can therefore be referred to as an Eulerian-Lagrangian approach.

In CFD-DEM, the fluid phase is assumed to be a continuum. The volume-averaged Navier-Stokes equations are used to describe the flow of fluid while, Newton's laws of motion are used to describe the movement of solid particles. The coupling between both the phases is achieved through the particulate volume fraction and the fluid-particle interaction forces. The coupling is hence, based on the exchange of data between the two phases. At each time-step DEM calculates the position and velocity data for each particle, CFD computes the fluid-velocity, pressure and other fields over the domain and relevant data is then exchanged. An explicit scheme is usually used for the coupling. Sets of equations for both phases are solved to advance the solution in time step-by-step.

Grid-based approaches like the finite volume method (FVM) and the finite element method (FEM) are usually used to solve CFD problems. A CFD-DEM approach is said to be "resolved" if the particle sizes are larger than the cell size of the computational grid, in which case a single particle occupies multiple cells of the grid. A CFD-DEM approach is said to be "unresolved" if the particle sizes are much smaller than the cell size. As the unresolved approach can accommodate much more particles in a simulation than the resolved approach, it is often the preferred strategy for studying industrial processes. This study focuses on the unresolved approach only.

CFD-DEM provides values for quantities including velocity, pressure, particle-position, particle-velocity, volume fraction and force for the duration of the simulation. These variables are difficult to obtain experimentally due to the limitations of technology to monitor them or the expense of conducting them. CFD-DEM thus allows us to investigate fluid-particulate flow with great detail and also enhances our understanding of the associated phenomena such as mixing, segregation, distribution and concentration.

CFD-DEM can be applied to research as well as practical engineering applications. It has been widely used to analyse gas fluidisation, pneumatic conveying, granulation, blending, segregation etc. It has also been extensively used to model industrial processes such as gas cyclones, filtration, solid-liquid mixing and spray coating. Complex processes such as circulating fluidised bed for cracking, blast furnaces, chemical reactors and trickle beds can also be modelled using this numerical method. Due to the variety of applications, CFD-DEM has steadily gained importance in both academia and the industry. The ever increasing computational power makes CFD-DEM promising and extensive research is currently being carried out to improve both speed and accuracy.

## 3.2 The fluidised bed and drag models

In this section the use of the fluidised bed experiment to evaluate CFD-DEM models and the need for an alternative validation technique is deliberated. Also questions surrounding the suitability of drag models are discussed.

### 3.2.1 Literature

The CFD-DEM approach has steadily gained popularity over the last three decades due to increase in computing power. It was used in [TKT93] to simulate a spouting bed where gas is injected from a nozzle at the bottom of the container. An experiment with the same geometry and operating conditions was performed. The particle motion was observed using a video tape recorder and pressure fluctuation was measured. In [HKBvS96], a hard-sphere approach was adopted to simulate bubble and slug formation in a two-dimensional gas-fluidised bed. The methodology was validated experimentally using glass beads in a cold flow set up. In [XY97], a predictor-corrector scheme for collision dynamics was adopted to allow the use of stiffer particles at a reasonable time step size. Coupling between the discrete phase and fluid was achieved by applying Newton's third law of motion directly to the individual particles and fluid phase. The fluidised bed was simulated and the bed pressure drop was studied. In [GGT$^+$98], bubble rise velocity, voidage variation and average particle/fluid velocities were computed in fluidised beds. The findings were compared to those obtained using the continuum theory based simulations. In [XYCZ00], the CFD-DEM approach was applied to study strong localised discrete particle motion in a packed bed caused by lateral gas blasting. It demonstrated that both raceway and fluidisation are results of gas-solid and solid-solid interactions in a packed bed. A numerical study on segregation and mixing of binary mixtures in gas-fluidised beds are presented in [FXZ$^+$04]. The simulation was validated by comparisons with measured results. A computational study on a lab-scale fluidised bed was presented in [CMMH05], where the results from a CFD-DEM approach were compared to those obtained from a multi-fluid CFD model and both were further compared to experimental results. It was assessed in [LCDK05] the capability of a CFD-DEM model to reproduce several regimes observed in a spout-fludised bed experiment. Various drag closures were tested in the model and their suitability was assessed. In [DRDM07], numerical simulations were used to explore the possibility of reproducing particulate and aggregate fluidisation in the absence of cohesive forces. A system of glass beads fluidised by water was used in addition to gas-fluidisation. In [CY08], the applicability of CFD-DEM to such systems as pneumatic conveying bends, cyclone separators and circulating fluidised beds was demonstrated. The numerical results were, either qualitatively or quantitatively shown to be in good agreement with experimental data. In [CWYV09], a CFD-DEM model was developed to describe multiphase flow in dense medium cyclones. The "surging" phenomenon was studied in detail. In [ZKCY10], the origins of various formulations in CFD-DEM were discussed. Their relationships were established and a comparative study was performed by simulating fluidisation, pneumatic conveying and hydrocyclones. In [VBVDD$^+$11], the effect of multiple spouts on the bed dynamics was studied. Particle image velocimetry (PIV) and positron emission particle tracking (PEPT) were used to obtain experimental results which were then compared to the simulation results. A multi-purpose CFD-DEM framework based on open source code was presented in [KGH$^+$12]. The approach was then validated using analytical and experimental data. [AE13] validated their CFD-DEM code using the fluidised bed experiment with emphasis on computing cost and parallelisation. Heat transfer in a gas-solid fluidised bed is simulated

using CFD-DEM in [LMLB17]. [WGY+18] used a smoothed void fraction method to compute void fractions in CFD-DEM and validated it by simulating a spout fluidised bed. Detailed reviews on the CFD-DEM approach can be found in [ZZYY08, DAVdHK07, ZYZ+16].

### 3.2.2 A new validation technique

The fluidised bed experiment has been widely used in the literature to validate various CFD-DEM codes. The experiment is a lab scale version of a very important industrial application, gas-fluidisation, and it offers a wide range of densification regions. Bed pressure drops or particle flux across cross-sections of the fluidised bed have often been used as quantifications to validate numerical codes. Fluidised beds involve high Reynolds number flows and obtaining reproducible results is a challenging task. We propose a new experimental set-up, intended for lower Reynolds number flows, which is easier to reproduce and simpler to quantify. The new experiment, in complement with the fluidised bed, can be used as a standard benchmark to validate the CFD-DEM approach or assess various physical and numerical modules used within its framework. The first main technical contribution of the study in this chapter is thus the *cross-flow sedimentation* validation test as a new benchmark experiment for integrated performance evaluation of CFD-DEM simulation.

### 3.2.3 Evaluation of drag models

In fluid-particle flows, the drag and pressure-gradient forces play a dominant role in determining the movement of particles. An accurate drag model is thus critical to successful CFD-DEM simulation [NZSGM16]. Although the drag on an isolated spherical particle is well-established, the drag in presence of a swarm of particles remains a subject of research without a general consensus. Various drag models have been proposed in the literature and used in CFD-DEM simulations. These models vary greatly in their formulations, and their performance in CFD-DEM simulations has not been systematically assessed, raising questions for their suitability in practical applications. This study presents a detailed evaluation of commonly-used drag models in CFD-DEM simulation, where the performance of various drag models is analysed and their suitability in different conditions is discussed. The second main technical contribution of this study is thus, a systematic and objective evaluation of drag models in CFD-DEM simulation to clarify the suitability and limitation of existing drag models under specific physical conditions.

### 3.2.4 Layout of chapter

The remainder of this chapter is organized as follows. In § 3.3, the CFD and DEM governing equations and the coupling schemes including drag models are explained. In § 3.4, an in-house CFD-DEM code is first carefully validated, after which it is used to evaluate different drag models that have been widely used in the literature. In § 3.5, the *cross-flow sedimentation* test is introduced as an alternative validation

experiment for CFD-DEM codes, and the in-house code is used to simulate the test and results are compared to those obtained from lab experiments. In the final section § 3.6, concluding remarks are drawn from the discussions of previous sections.

## 3.3 CFD-DEM formulation

An in-house code is employed in this study for the evaluation of drag models and CFD-DEM simulation. The development of the code began with this thesis and by the author. In this section, the governing equations of CFD, DEM and the coupling between them are briefly recapped, and the numerical strategies used by the in-house code to solve them are explained. Besides providing a compact overview of CFD-DEM modelling, the main purpose of this section is to provide sufficient technical details for CFD-DEM modelling such that the following comparison study and evaluation can be carried out in a transparent and objective manner. Specifically, the formulations for CFD and DEM are explained in § 3.3.1 and § 3.3.2, respectively, after which their coupling strategies including drag models are explained in § 3.3.3.

### 3.3.1 CFD

We consider the volume-averaged incompressible Navier-Stokes equations to govern the flow of fluid in the presence of a particulate phase [GKD+12]:

$$\frac{\partial \left(\rho_{\mathrm{f}} \alpha_{\mathrm{f}}\right)}{\partial t} + \nabla \cdot \left(\rho_{\mathrm{f}} \alpha_{\mathrm{f}} \boldsymbol{u}_{\mathrm{f}}\right) = 0 \tag{3.1}$$

$$\frac{\partial \left(\rho_{\mathrm{f}} \alpha_{\mathrm{f}} \boldsymbol{u}_{\mathrm{f}}\right)}{\partial t} + \nabla \cdot \left(\rho_{\mathrm{f}} \alpha_{\mathrm{f}} \boldsymbol{u}_{\mathrm{f}} \boldsymbol{u}_{\mathrm{f}}\right) = -\alpha_{\mathrm{f}} \nabla p + \nabla \cdot \left(\alpha_{\mathrm{f}} \boldsymbol{\tau}_{\mathrm{f}}\right) + \alpha_f \rho_f \boldsymbol{g} + \boldsymbol{R}_{\mathrm{f,p}} \tag{3.2}$$

where $\rho_{\mathrm{f}}$ is the density of fluid, $\alpha_{\mathrm{f}}$ is the volume fraction of fluid, $\boldsymbol{u}_{\mathrm{f}}$ is the velocity of fluid, $\boldsymbol{\tau}_{\mathrm{f}}$ is the stress tensor for the fluid phase, $p$ is the fluid pressure and $\boldsymbol{g}$ is the acceleration due to gravity. The term $\boldsymbol{R}_{\mathrm{f,p}}$ represents the exchange of momentum with the particulate phase and plays an important role in CFD-DEM coupling, and it will be discussed further in § 3.3.3. Eqs. (3.1) and (3.2) are often referred as the continuity and momentum equations in the study of fluid mechanics. Numerical techniques to solve the Navier-Stokes equations are well established and will not be discussed in detail in this thesis. The CFD governing equations in the in-house code are solved using cell-centred FVM, and the pressure based SIMPLE algorithm [MMD+16] is used for pressure-velocity coupling.

### 3.3.2 DEM

There are two versions of DEM used in the literature, namely, the hard-sphere or event-driven approach (ED) and the soft-sphere approach. The ED approach is suitable for the cases where collision between particles happen occasionally and the collisions are predominantly binary. The in-house code uses a soft-sphere approach as the intended use is for applications involving high number of collisions with

multiple contacts. In this approach, particles are allowed to overlap with each other and the inter-particle forces are based on the amount of overlap.

In the soft-sphere DEM, equations of motion for each individual particle are solved using an iterative time-integration scheme. Velocities and accelerations are assumed to be constant during each time step. By integrating, the new positions and velocities of particles, and hence their overlaps, are calculated. Based on the new overlaps and the collision history of the particles, the contact forces acting on all particles are calculated. Thereafter, the linear and angular accelerations of particles are calculated and next iteration starts with the integration of the equations of motion.

#### 3.3.2.1 Governing equations and contact laws

We consider all particles to be mathematically represented by a sphere. Particle motion is governed by the Newton's equations for translational and rotational degrees of freedom [Lud08]:

$$m_i \frac{\mathrm{d}^2}{\mathrm{d}t^2} \boldsymbol{r}_i = \boldsymbol{f}_i + m_i \boldsymbol{g} \tag{3.3}$$

$$I_i \frac{\mathrm{d}}{\mathrm{d}t} \boldsymbol{\omega}_i = \boldsymbol{t}_i \tag{3.4}$$

where $m_i$ is the mass of particle $i$, $\boldsymbol{r}_i$ is its position, $\boldsymbol{f}_i$ is the sum of all contact and fluid forces on the particle, and $\boldsymbol{g}$ is the acceleration due to gravity. In Eq. (3.4), $I_i$ is the moment of inertia of particle $i$, $\boldsymbol{\omega}_i$ is its angular velocity, and $\boldsymbol{t}_i$ is the total torque on the particle due to tangential contact forces.

Two colliding particles are shown in Figure 3.1. Normal contact forces are determined by the linear contact model shown in Figure 3.2. Overlap $\delta$ between two contacting spherical particles $i$ and $j$ with radii $a_i$ and $a_j$ respectively is given by

$$\delta = (a_i + a_j) - (\boldsymbol{r}_i - \boldsymbol{r}_j) \cdot \boldsymbol{n} \tag{3.5}$$

where $\boldsymbol{n}$ is the unit vector pointing from particle $j$ to $i$. The magnitude of the normal force $f^n$ for the contact is given by

$$f^n = k\delta + \gamma v_n \tag{3.6}$$

where $k$ is the spring stiffness, $\gamma$ is the viscous damping coefficient and $v_n$ is the magnitude of normal relative velocity given by $v_n = -\boldsymbol{v}_{ij} \cdot \boldsymbol{n} = -(\boldsymbol{v}_i - \boldsymbol{v}_j) \cdot \boldsymbol{n}$

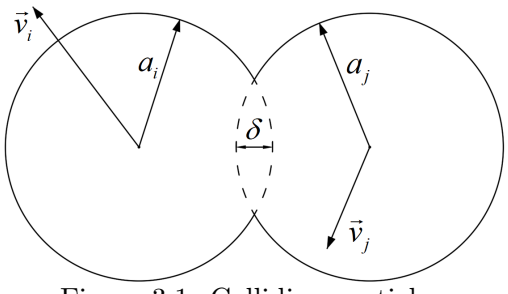

Figure 3.1: Colliding particles

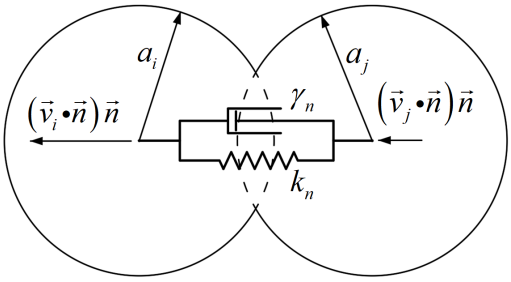

Figure 3.2: Normal contact model

Figure 3.3 shows the tangential contact model for two colliding particles. If the relative tangential velocity between the two particles in contact is $\boldsymbol{v}_t = \boldsymbol{v}_{ij} - \boldsymbol{n}\,(\boldsymbol{n} \cdot \boldsymbol{v}_{ij})$, the magnitude of tangential contact force is given by

$$f^t = \min \left\{ \left| k_\mathrm{t} \int_{t_{\mathrm{c},0}}^{t} \boldsymbol{v}_t dt + \gamma_t \boldsymbol{v}_t \right| , \mu f^n \right\} \tag{3.7}$$

where $k_t$ is the tangential spring stiffness, $\gamma_t$ is the tangential viscous damping coefficient and $\mu$ is the coefficient of friction. The integration term has limits from the time the particles came into contact $t_{c,0}$ to the time particles remain in contact. In addition to the tangential friction, rolling friction is implemented in a similar manner with rolling velocity $\boldsymbol{v}_r$ being used instead of relative tangential velocity.

$$\boldsymbol{v}_r = -a'_{ij} \left( \boldsymbol{n} \times \boldsymbol{\omega}_i - \boldsymbol{n} \times \boldsymbol{\omega}_j \right) \tag{3.8}$$

where $a'_{ij} = a'_i a'_j / \left( a'_i + a'_j \right)$ and $a'_\alpha = a_\alpha - \delta/2$, for $\alpha = i, j$. Parameters $\mu$, $k_t$ and $\gamma_t$ are replaced with $\mu_r$, $k_r$ and $\gamma_r$ respectively.

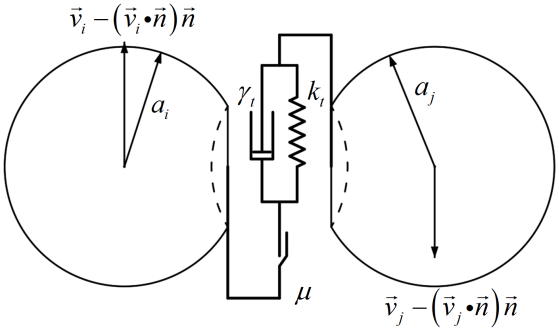

Figure 3.3: Tangential contact model

#### 3.3.2.2 Contact detection algorithm

A simple scheme to detect contacts in a system containing $N$ particles is to check all possible pairs of particles for overlap, which requires a total of $N(N-1)/2$ tests. It is thus an $\mathcal{O}(N^2)$ algorithm and is too slow for most practical applications. There exist more sophisticated and faster algorithms to detect contacts [PW01, WO95]. The time complexity of these algorithms is typically $\mathcal{O}(N \log N)$ and the fastest available is $\mathcal{O}(N)$. The in-house code uses an algorithm based on [WPC04] which places a "bounding box" around each individual particle. It divides the domain occupied

by all particles into "bins" indexed by using their positions. The algorithm then identifies which bins the particles' bounding boxes span over and adds them to the bins. Each particle is checked for overlap with only other particles belonging to the bins it belongs to. If the size of bins is suitably selected, this algorithm is of time complexity $\mathcal{O}(N)$.

#### 3.3.2.3 Time integration algorithm

Eq. (3.3) can be integrated using the Verlet algorithm [AT17]. From time $t$ to time $t + dt$, the particle $i$ is advanced as follows:

$$\boldsymbol{r}_i^{t+dt} = 2\boldsymbol{r}_i^t - \boldsymbol{r}_i^{t-dt} + dt^2 \boldsymbol{a}_i^t \tag{3.9}$$

where $t$ is the current time, $dt$ is the time step size and $\boldsymbol{a}_i$ is the acceleration of the particle given by:

$$\boldsymbol{a}_i = (\boldsymbol{f}_i + m_i \boldsymbol{g})/m_i \tag{3.10}$$

The velocity of the particle may be obtained by:

$$\boldsymbol{v}_i^t = \frac{\boldsymbol{r}_i^{t+dt} - \boldsymbol{r}_i^{t-dt}}{2dt} \tag{3.11}$$

Eq. (3.4) can be integrated in time in a similar fashion.

### 3.3.3 CFD-DEM coupling

The coupling between CFD and DEM is achieved by determining the appropriate hydrodynamic forces on the particles due to fluid flow and adding it to the $\boldsymbol{f}_i$ term in Eq. (3.3). Following Newton's third law of motion, the same force is applied back on the fluid through the $\boldsymbol{R}_{\mathrm{f},p}$ term in Eq. (3.2). The volume fraction $\alpha_f$ needs to be determined. At every time step, the following scheme is used to achieve CFD-DEM coupling:

1. Beginning of time step.
2. New particle positions and velocities are calculated by the DEM iteration.
3. Particle positions and velocities are passed to the CFD solver.
4. For each FVM cell the fluid volume fraction is determined.
5. The hydrodynamic forces on the particles are calculated.
6. The momentum exchange term for each FVM cell is computed.
7. Fluid forces on the particles are passed back to the DEM solver.
8. The CFD solver advances the solution in time.

Note that usually DEM time steps are smaller than CFD time steps. This is because DEM uses a fully explicit scheme which is subject to stability issues unlike the CFD solver. Thus several DEM sub-time steps are performed for a single CFD time step. This study takes a conservative approach and uses a time step size that is well within the critical limits of the DEM scheme and CFD solver. Since the paper focuses more on accuracy of results rather than speed, no sub-time steps are used in any CFD-DEM simulation.

#### 3.3.3.1 Determining cell volume fraction

In step 4 of the coupling scheme, the fluid volume fraction in CFD cells must be determined. Therefore, the volume of particles, which is a Lagrangian property, must be mapped as a volume fraction in CFD, which is an Eulerian property. The contact detection algorithm introduced in § 3.3.2.2 can be used to determine the FVM cells occupied by individual particles. A simple way to determine the volume fraction of solid particulate in a FVM cell is to sum up the volume of particles whose centres lie within the cell and divide it by the total volume of the cell. However, this approach would not give appropriate volume fraction values as a single particle could span across multiple cells. In the in-house code, a particle is divided into many parts with equal volumes and the location of the centre of these parts is used to determine the volume fraction within a FVM cell. This gives a much smoother distribution of volume fraction. In the unresolved version of CFD-DEM, it is important that the size of cells used is much larger than the size of particles. This avoids unnaturally high and thus unrepresentative values of volume fraction. In this study, the ratio of particle volume to cell volume of about 1 : 33 has been targeted and used in all CFD-DEM simulations.

#### 3.3.3.2 Hydrodynamic forces and drag models

In step 5 of the coupling scheme, the fluid forces on particles are computed. Drag force is the force resulting from relative velocity between the particle and fluid. Magnus forces arise from the rotation of the particle. Saffman force is the lift on a particle due to shear flow. The virtual mass force is applied on a particle when it accelerates in a fluid.

In the in-house code only the drag and pressure-gradient forces are considered as they are found to be the dominant forces in most applications. The pressure gradient force on a particle $i$ is given by

$$\boldsymbol{f}_i^{\nabla p} = -\nabla p \cdot V_i \tag{3.12}$$

where $V_i$ is the volume of the particle. The drag force on particle $i$ is given by the formula

$$\boldsymbol{f}_i^{D} = \frac{V_i \beta}{\alpha_p} \left( \boldsymbol{u}_f - \boldsymbol{v}_i \right) \tag{3.13}$$

where $\alpha_p = 1 - \alpha_f$ for the cell the particle is contained in, $\boldsymbol{u}_f$ is the velocity of fluid in that cell, $\boldsymbol{v}_i$ is the velocity of the particle, and $\beta$ is the inter-phase momentum transfer coefficient due to drag. The pressure-gradient and drag forces,

once determined, can be added to $\boldsymbol{f}_i$ in Eq. (3.3). Although drag on a single particle has been studied extensively, the drag on a particle in the presence of other particles is still a subject of research. Several drag relations have been proposed to calculate $\beta$ in the literature. The most widely used drag model in CFD-DEM modelling is a combination of the Ergun equation [EO49] and the Wen and Yu relation [Wen66]. For $\alpha_f < 0.8$

$$\beta = 150\frac{\alpha_p^2}{\alpha_f}\frac{\mu_f}{d^2} + 1.75\alpha_p\frac{\rho_f}{d}\left|\boldsymbol{u}_f - \boldsymbol{v}\right| \tag{3.14}$$

where $\mu_f$ and $\rho_f$ are the viscosity and density of the fluid respectively and $d$ is the diameter of the particle. For $\alpha_f > 0.8$

$$\beta = \frac{3}{4}C_D\alpha_p\frac{\rho_f}{d}\left|\boldsymbol{u}_f - \boldsymbol{v}\right|\alpha_f^{-1.65} \tag{3.15}$$

where $C_D$ is the coefficient of drag on a single particle given by [Sch33]

$$C_D = \begin{cases} \frac{24}{Re_p}\left(1 + 0.15Re_p^{0.687}\right) & \text{if } Re_p < 1000 \\ 0.44 & \text{if } Re_p \geqslant 1000 \end{cases} \tag{3.16}$$

$Re_p$ is the Reynolds number for the particle

$$Re_p = \frac{\alpha_f\rho_f\left|\boldsymbol{u}_f - \boldsymbol{v}\right|d}{\mu_f} \tag{3.17}$$

A drag model obtained from lattice-Boltzmann simulations was proposed by Koch and Hill [KH01]

$$\beta = \frac{18\mu_f\alpha_f^2\alpha_p}{d^2}\left(F_0\left(\alpha_p\right) + \frac{1}{2}F_3\left(\alpha_p\right)Re_p\right) \tag{3.18}$$

where $F_0$ and $F_3$ are given by

$$F_0\left(\alpha_p\right) = \begin{cases} \frac{1+3\sqrt{\frac{\alpha_p}{2}}+\frac{135}{64}\alpha_p\ln(\alpha_p)+16.14\alpha_p}{1+0.681\alpha_p-8.48\alpha_p^2+8.16\alpha_p^3} & \text{if } \alpha_p < 0.4 \\ \frac{10\alpha_p}{\alpha_f^3} & \text{if } \alpha_p \geqslant 0.4 \end{cases} \tag{3.19}$$

$$F_3\left(\alpha_p\right) = 0.0673 + 0.212\alpha_p + \frac{0.0232}{\alpha_f^5} \tag{3.20}$$

Another drag model was proposed by Di Felice [DF94] and is given by

$$\beta = \frac{3}{4}C_D\alpha_p\frac{\rho_f}{d}\left|\boldsymbol{u}_f - \boldsymbol{v}\right|{\alpha_f}^{2-\chi} \tag{3.21}$$

where $\chi$ and $C_D$ are given by

$$\chi = 3.7 - 0.65\mathrm{e}^{\left(-0.5(1.5-\log_{10}Re_p)^2\right)} \tag{3.22}$$

$$C_d = \left(0.63 + 4.8Re_p^{-0.5}\right)^2 \tag{3.23}$$

Beetstra et al. [BvdHK07] proposed a drag model as follows:

$$\beta = 18\frac{\mu_f \alpha_f \alpha_p \hat{f}^D}{d_i^2} \times \left( \left( \frac{180\alpha_p}{18\alpha_f^2} \right) + \alpha_f^2 \left(1 + 1.5\sqrt{\alpha_p}\right) + \left( \frac{0.413}{24\alpha_f^2} \right) \left( \frac{\alpha_f^{-1} + 3\alpha_p\alpha_f + 8.4Re_p^{-0.343}}{1 + 10^{3\alpha_p} Re_p^{-(1+4\alpha_p)/2}} \right) Re_p \right) \tag{3.24}$$

A more recent drag was proposed by Cello et al. [CDRDM10] as:

$$\beta = 18\frac{\mu_f \alpha_f \alpha_p \hat{f}^D}{d_i^2} \left( k_1 + k_2\alpha_f^4 + k_3 \left(1 - \alpha_f^4\right) \right) \tag{3.25}$$

where $k_0$, $k_1$, $k_2$ and $k_3$ are given by

$$k_0 = \frac{(1 - \alpha_f)}{1 + 3\alpha_f} \tag{3.26}$$

$$k_1 = \frac{1 + 128k_0 + 715k_0^2}{\alpha_f^2 \left(1 + 49.5k_0\right)} \tag{3.27}$$

$$k_2 = \frac{1 + 0.13Re_p + 6.66 \times 10^{-4} Re_p^2}{1 + 3.42 \times 10^{-2} Re_p + 6.92 \times 10^{-6} Re_p^2} - 1 \tag{3.28}$$

$$k_3 = \left( \frac{2Re_p^2}{1 + Re_p} \right) \times \left( \frac{-410\alpha_f + 9.2 \times 10^7 \,\mathrm{Re}_p\, k_0^{20} + 1900\alpha_f^2 - 6.6 \times 10^{-2}\,\mathrm{Re}_p}{6600\alpha_f + 4.92 \times 10^{-4}\,\mathrm{Re}_p - 4.3 \times 10^4\alpha_f^2 - 1.31 \times 10^{-4} Re_p^2 + 7.38 \times 10^4\alpha_f^3} \right) \tag{3.29}$$

Other drag models (e.g. [Gil01]) are available in the literature, while the aforementioned models are most widely used in CFD-DEM simulations.

Figure 3.4 shows the drag on a particle using various drag models against particulate volume fraction at a Reynolds number of $Re = 1$. The particle diameter is $200\mu m$. At low volume fractions, the drag models give similar drag forces. As the volume fraction increases, the difference between drag models increases, but still follow the same general trend. Koch-Hill, Beetsrta and Cello models follow each other more closely than the other two. Figure 3.5 shows the drag versus Reynolds number for a particulate volume fraction $\alpha_s = 0.25$. For lower Reynolds number, all drag models are similar, however for higher Reynolds numbers the difference between them increases rapidly. The Ergun-Wen-Yu model particularly deviates by a higher margin from the other models. Koch-Hill, Beetstra and Cello models again follow each other more closely.

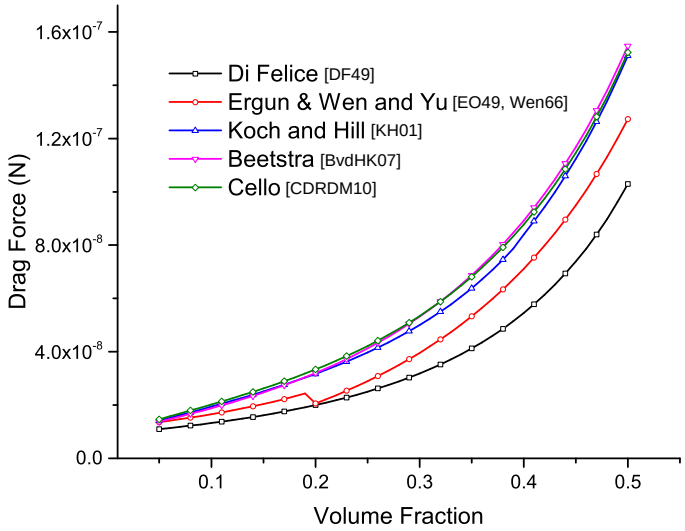


Figure 3.4: The relationship between drag force and particulate volume fraction at a fixed Reynolds number $Re = 1$

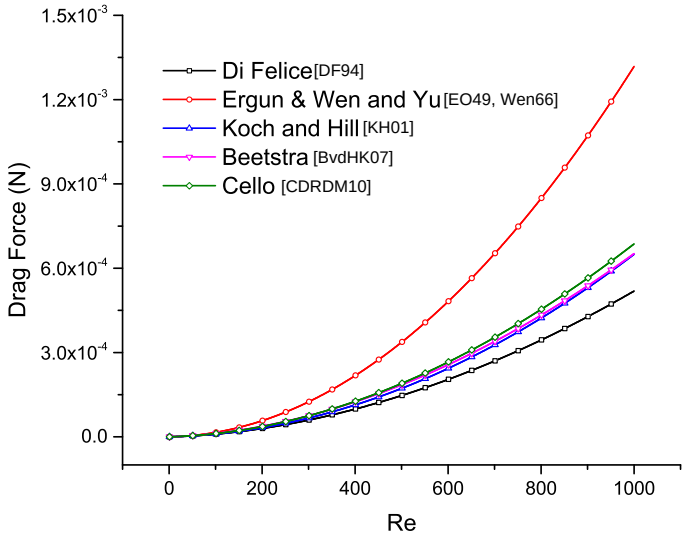


Figure 3.5: The relationship between drag force and Reynolds number at a fixed particulate volume fraction $\alpha_s = 0.25$

#### 3.3.3.3 Computing the momentum exchange term

Step 6 of the CFD-DEM coupling scheme is to compute the momentum exchange term for each finite volume cell. For a FVM cell, the term can be written as

$$\boldsymbol{R}_{\mathrm{f,p}} = K_{\mathrm{f,p}}\boldsymbol{u}_{\mathrm{f}} - K_{\mathrm{f},p}\left\langle \boldsymbol{v} \right\rangle \tag{3.30}$$

where $\langle \boldsymbol{v} \rangle$ is the ensemble averaged particle velocity for all particles in that cell. $K_{f,p}$ is given by

$$K_{\mathrm{f,p}} = -\frac{\left|\sum_i \boldsymbol{f}_i^D\right|}{V_{\mathrm{cell}}\left|\boldsymbol{u}_{\mathrm{f}} - \left\langle \boldsymbol{v} \right\rangle\right|} \tag{3.31}$$

where $V_{cell}$ is the volume of the FVM cell and $\boldsymbol{f}_i^D$ is the drag force on the particle calculated from any of the drag models introduced in the previous section.

## 3.4 Evaluation of drag models

As discussed in § 3.3, the CFD-DEM formulation comprises of three technical elements: the CFD, the DEM, and their coupling. Based on Navier-Stokes equations, the CFD formulation is mathematically rigorous with proven numerical solution schemes. Based on Newton's second law, the DEM governing equations are also mathematically sound and have robust numerical solution schemes. The contact laws in DEM are of an empirical nature, but they are simple and relatively easy to tune for specific applications. In addition, the particle-particle contact rarely dominates in practical particle-laden flows, with the exception of particles packed at extremely high volume fraction. Hence, the main modelling uncertainty lies with the CFD-DEM coupling, especially the phenomenological drag models. As summarised in § 3.3.3.2, there are at least five popular drag models proposed in the literature, all well cited and widely used in CFD-DEM codes. But these drag models have very different formulations, and depending on the flow regime their evaluations for drag forces can differ greatly. Hence, to avoid systematic mistakes in practical CFD-DEM applications, it is essential to examine the performance of different drag models and justify their suitability under specific physical conditions.

An in-house code is used to evaluate the performance of different drag models. As CFD-DEM coupling including drag models is an integrated part in CFD-DEM simulation, we must first fully verify the CFD and DEM modules before applying the code to investigate drag models. It is to be noted that comprehensive tests have been performed to confirm the accuracy of the CFD and DEM formulations and associated solution schemes in the code. But in order to keep the text brief and to the point, their validations are only demonstrated with two classic benchmark tests in § 3.4.1 and § 3.4.2, respectively. The focus is on the drag model evaluation, which is described in detail in § 3.4.3 and § 3.4.4.

### 3.4.1 CFD solver validation

The lid-driven cavity is a common benchmark often used to test the accuracy of CFD code. The test is well documented in the literature [GGS82] and therefore not repeated here. The CFD module in the in-house code is validated by simulating the lid-driven cavity. The data-set provided by [GGS82] is used for comparison. Figure 3.6 shows the dimensionless velocity in the X direction (made dimensionless by dividing with velocity of the lid) along the cavity's centre-line. The Reynolds number is 100. The results from the code closely match the data from [GGS82]. This indicates the CFD module in the code works as intended. Note that the CFD code was subjected to a further thorough validation. The lid-driven cavity is chosen as a representative example in this study.

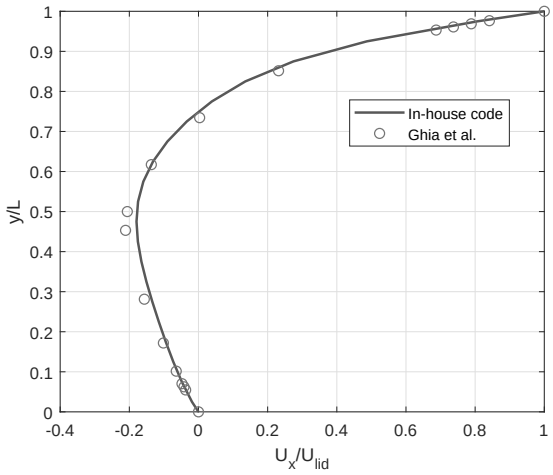


Figure 3.6: Dimensionless velocity in X direction along the centre line of the cavity for $Re = 100$

### 3.4.2 DEM solver validation

To validate the DEM module, particles are filled into a cylinder. The cylinder walls are then taken off and particles are allowed to settle into a heap under self-weight. The initial configuration of the particles is shown in Figure 3.7. The angle of repose for the fallen heap is then measured. If the contact models in DEM have been accurately modelled, this slope should be close to $tan^{-1}(\mu)$, where $\mu$ is the friction coefficient from Eq. (3.7). Properties of the particles used in the simulation are given in Table 3.1. Figure 3.8 shows the final configuration of the heap in the simulation. The angle of repose is found to be around 20.5° which closely matches the expected value of 21.8°. This result confirms the DEM module in the in-house code functions correctly. Note that the DEM solver was subjected to further checks and that the angle of repose test is chosen as a representational example.

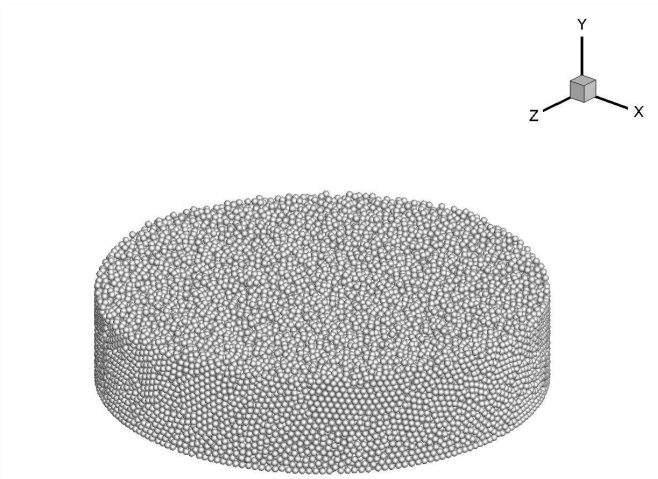


Figure 3.7: Initial configuration of set-up for DEM validation

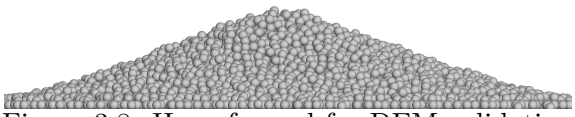

Figure 3.8: Heap formed for DEM validation

Table 3.1: Properties of particles used in DEM validation

| **Property** | **Value** | **Unit** |
|---|---|---|
| Radius | 0.0015 | $m$ |
| Density | 2505 | $kg/m^3$ |
| $\mu$ | 0.4 | |
| Coefficient of Restitution | 0.66 | |

### 3.4.3 Validation of drag on a single particle

In this section we validate the capability of the in-house code to accurately model drag in the case of a solitary particle. In this case, the volume fraction of the solid phase is close to zero and its influence on the fluid phase is minimal, making it an ideal scenario to test the code's ability to capture hydrodynamic forces on a particle. This validation also serves the purpose of testing the performance of drag models introduced in § 3.3.3.

A single particle is allowed to fall through water under the influence of gravity in a rectangular domain. The simulation is run until the particle achieves terminal velocity and is repeated with all drag models. The values obtained are compared to those computed from an empirical expression. The expression used to find terminal velocity $u_t$ is a function of $C_D$, the coefficient of drag. However, $C_D$ is itself a complex function of the Reynolds number $Re$, which in-turn is a function of velocity. In [HL89], it was suggested the use of an explicit expression to give the terminal velocity of a sphere proposed in [TC87]. The dimensionless terminal velocity $u_*$ is given by

$$u_* = \left[ \left( \frac{18}{d_*^2} \right)^{0.824} + \left( \frac{0.321}{d_*} \right)^{0.412} \right]^{-1.214} \tag{3.32}$$

where $d_*$ is the dimensionless diameter given by

$$d_* = d \left[ \frac{g\rho_f \left( \rho_\mathrm{s} - \rho_\mathrm{f} \right)}{\mu^2} \right]^{1/3} \tag{3.33}$$

where $d$ is the diameter of the particle, $g$ is acceleration due to gravity, $\rho_f$ is the density of the fluid, $\rho_s$ is density of the particle and $\mu$ is the viscosity of the fluid. The terminal velocity is obtained from

$$u_t = u_* / \left[ \frac{\rho_\mathrm{f}^2}{g\mu \left( \rho_\mathrm{s} - \rho_\mathrm{f} \right)} \right]^{1/3} \tag{3.34}$$

The density of particles used in the simulations is $1500 kg/m^3$ and the water

properties are given in Table 3.4. Figure 3.9 shows the terminal velocity obtained from the code using Di Felice, Koch-Hill, Ergun-Wen-Yu, Beetstra and Cello drag models. It is compared to the terminal velocities obtained from the expression (3.32). For a smaller particle with lower terminal velocity, all five drag models closely match the empirical expression. When the particle gets bigger, Di Felice and Ergun-Wen-Yu models still closely follow the empirical expression, however, Koch-Hill and Beetsrta models tend to deviate from it. The Cello model appears to follow a straight line which eventually deviates from the expression. This finding suggests that Di Felice and Ergun-Wen-Yu models are better suited to capture drag on a single particle than the others with the former slightly under-predicting the terminal velocity and the later marginally over-predicting it. It is worth noting that the in-house code is able to achieve a terminal velocity with all drag models which also confirms that the coupling in the code is working properly and can, with reasonable accuracy, capture the drag on a single solitary particle.

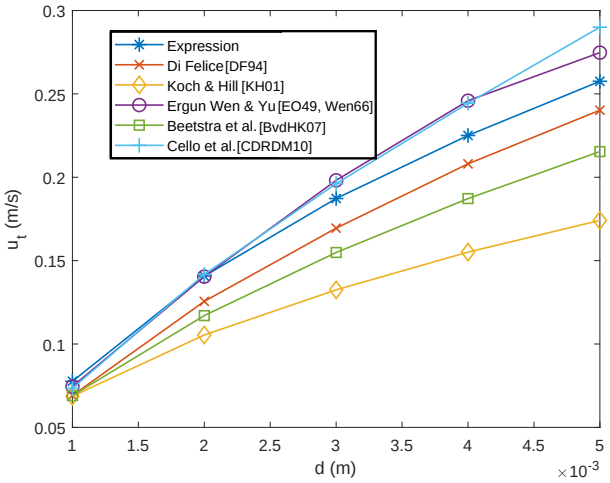


Figure 3.9: Terminal velocity from in-house code using various drag models and expression (3.32) for different particle diameters

### 3.4.4 Validation of drag on particles in the presence of significant volume fraction

In the previous section, the in-house code and the drag models are only assessed with the presence of a single particle. In this section, the code performance and drag models are examined in the case of a swarm of particles, which are closely spaced such that the particle volume fraction is significant and considerably affects the fluid flow. In this scenario, the drag force on each particle is also affected by the presence of neighbouring particles, while a good drag model should account for this effect and correct the drag accordingly.

The test is set up in an enclosed channel of rectangular cross-section. As shown in Figure 3.10, particles are artificially fixed in the middle section of the channel and are equally spaced. Water is injected at one end and flows out through the other. The water flow is thus forced through the particulate region and applies drag on the particles that are fixed in the space. In the laminar flow regime, it is expected that

a steady state will be achieved eventually. In this controlled particle-laden flow, the volume fraction of particles can be freely adjusted by varying the amount of particles fixed in the channel. Recreating the case experimentally is not a trivial task. We therefore use results from pure CFD simulations with the particles completely resolved as wall boundaries, as the basis for comparison. The commercial solver, *ANSYS Fluent*, is used for this purpose. In addition, to achieve objective and unbiased evaluation, comparisons with an independent third-party CFD-DEM code [KGH$^+$12] are also conducted.

As shown in Figure 3.10, three different particle configurations, named *Config1*, *Config2* and *Config3*, are considered, and their particle volume fractions are 0.0654, 0.1309 and 0.2818, respectively. The test channel has dimensions of $6cm \times 2cm \times 2cm$ and the particles have the same diameter of $200\mu m$. The channel walls are all modelled as *slip walls* without shearing resistance to the flow and the gravity is set to zero. Mesh convergence analysis is first conducted for the *ANSYS Fluent* simulation to ensure that the mesh used is adequately refined for the purpose of our comparative study. As an illustration for the mesh convergence study, the total drag force on all particles is plotted against the number of cells used in the simulation in Figure 3.11, where the inlet velocity is set as $0.05024m/s$ for all three configurations. Following mesh convergence analysis, high-fidelity CFD simulation results are obtained with *ANSYS Fluent*, by using $7,925,251$ cells for *Config1*, $10,597,400$ cells for *Config2*, and $12,721,100$ cells for *Config3*.

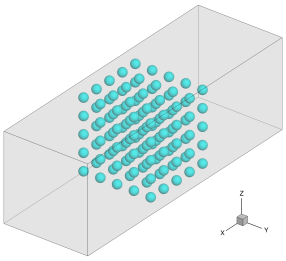

*Config1*

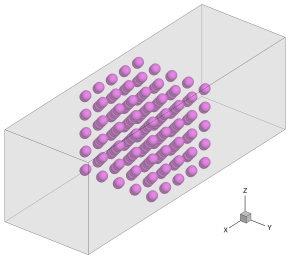

*Config2*

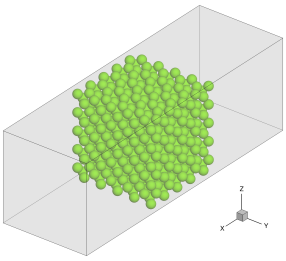

*Config3*

Figure 3.10: The test configurations

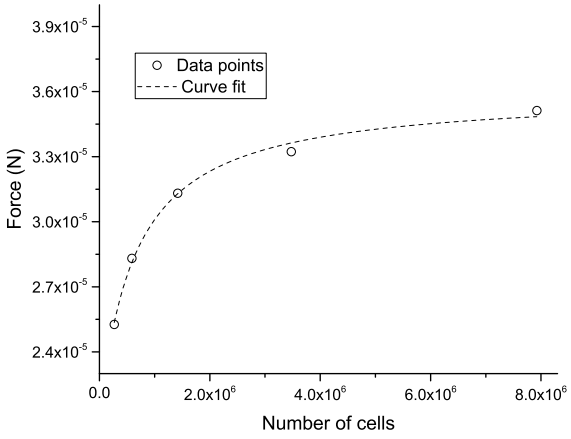


*Config1*

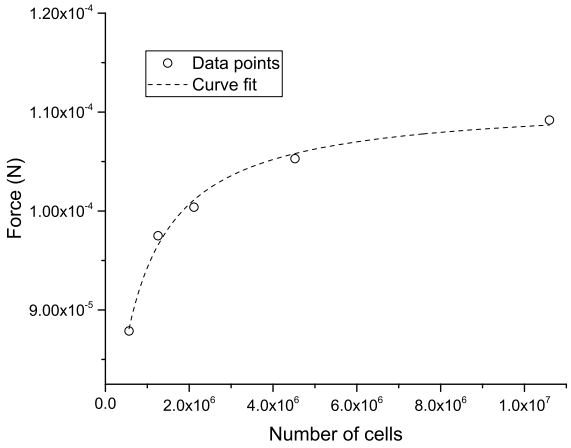


*Config2*

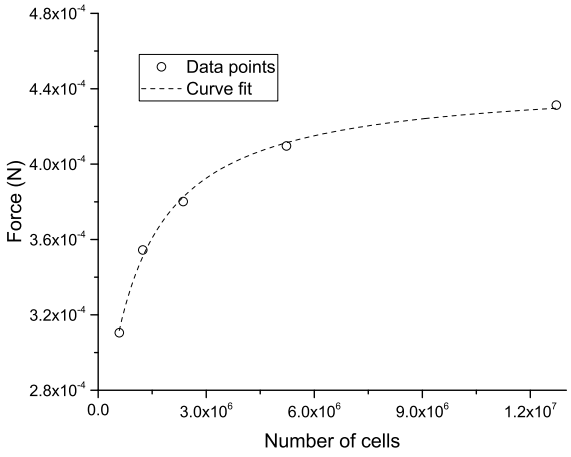


*Config3*

Figure 3.11: Total drag forces obtained by *ANSYS Fluent* simulations

The average velocity of the fluid in the particulate region can be estimated by a simple formula:

$$u_f^{middle} = \frac{u_f^{inject}}{\alpha_f^{middle}} \tag{3.35}$$

where $u_f^{inject}$ is the injection velocity and $\alpha_p^{middle}$ is the volume fraction of particles

in the particulate region. If the governing equations in the code have been correctly modelled, the volume averaged velocity in the particulate region should be close to $u_f^{middle}$. It is found that the choice of drag model does not affect this particular result much. This is because the fluid flow in this case is mostly influenced by the continuity equation. Validation is performed by running CFD-DEM simulations for each configuration with an inlet velocity of $0.05024m/s$. We also include the volume averaged velocity of the particulate region obtained from the pure CFD simulations for additional validation. Figure 3.12 shows the fluid velocity in the X direction on a slice through the centre of *Config1* obtained from the result of the CFD-DEM simulation. Similarly, Figure 3.13 shows the same results obtained from the pure CFD simulation. It can be observed that the velocity of fluid in the particulate region first increases on average and then reduces. The volume averaged velocity in the particulate region from simulations of all configurations are listed in Table 3.2. The average velocities in the particulate region, obtained from both the pure CFD and CFD-DEM simulations closely match the values obtained from Eq. (3.35). This result confirms that the fluid governing equations in the in-house code have been properly implemented.

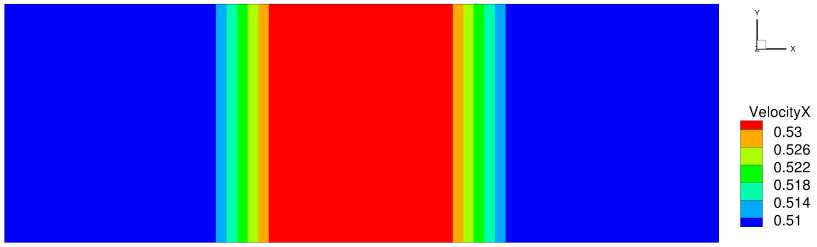


Figure 3.12: X direction velocity in $m/s$ on a slice through the centre of the *Config1* (In-house code result)

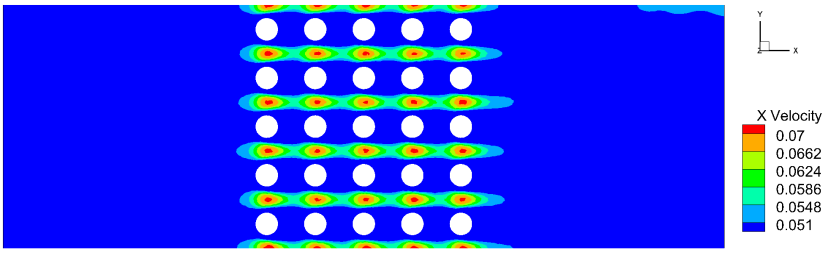


Figure 3.13: X direction velocity in $m/s$ on a slice through the centre of the *Config1* (*ANSYS Fluent* result)

Table 3.2: Averaged X velocity for the particulate region of all configurations using *ANSYS Fluent*, the in-house code and Eq. (3.35)

| **Configuration** | $\alpha_f$ | **Eq. (3.35)** | ***ANSYS Fluent*** | **In-house code** |
|---|---|---|---|---|
| *Config1* | 0.9346 | $0.0537m/s$ | $0.0535m/s$ | $0.0539m/s$ |
| *Config2* | 0.8691 | $0.0578m/s$ | $0.0576m/s$ | $0.0580m/s$ |
| *Config3* | 0.7382 | $0.0680m/s$ | $0.0676m/s$ | $0.0687m/s$ |

Next, drag forces on the particles obtained from the pure CFD simulations and CFD-DEM simulations using different drag models are compared. Inlet velocities are chosen such that the Reynolds numbers, using the particle diameter as the characteristic length, are 0.01, 0.1, 1, 10 and 100. These values correspond to an inlet velocity of $0.00005024m/s$, $0.0005024m/s$, $0.005024m/s$, $0.05024m/s$ and $0.5024m/s$ respectively. Figure 3.14 shows the comparison of drag models for all configurations using results from *ANSYS Fluent* as the basis. Relative difference ($RD$) is plotted against Reynolds number and is given by

$$RD = \frac{D_{DM} - D_{AF}}{D_{AF}} \tag{3.36}$$

where $D_{AF}$ is the total magnitude of drag force on all particles obtained using *ANSYS Fluent* results and $D_{DM}$ is the same obtained using CFD-DEM results by incorporating a particular drag model. In addition to results obtained from the in-house code, $RD$ is calculated for results obtained from the open source code *CFDEM* [KGH$^+$12] and has been included in the figure to serve as further verification.

It can be observed in Figure 3.14 that results from *CFDEM* and the in-house code closely match with each other. Since these two CFD-DEM codes are totally independent, the good agreement confirms their correct implementation of drag models. Hence, the relative difference $RD$ between CFD-DEM and *ANSYS Fluent* results can be trusted for evaluating drag models. As shown in Figure 3.14, the relative difference $RD$ is more or less constant for all three configurations at lower Reynolds number ($Re < 1$). All drag models under-predict the drag on the particles. The relative error is around $-30\%$ for Koch-Hill, Beetrstra and Cello models and is not affected much by the increase in volume fraction. The value is around $-50\%$ for Di Felice and Ergun-Wen-Yu models. However at higher Reynolds numbers ($Re > 1$) the relative error loses the constant value and begins to increase with increasing $Re$ for all drag models in all three configurations. In doing so, at a particular $Re$, the relative error assumes a value of zero, but beyond that it continues increasing rapidly.

The drag models thus have a behaviour which is independent of $Re$ only if $Re < 1$. For this case, results from Koch-Hill, Beetstra and Cello models are closer to the values obtained from *ANSYS Fluent* than Di Felice or Ergun-Wen-Yu models. It is not surprising that Koch-Hill, Beetstra and Cello models follow each other very closely as similar trends are observed in Figures 3.4 and 3.5. The results for $Re > 1$ show that the drag models diverge from the *ANSYS Fluent* results and the difference increases at an exponential rate. All drag models, thus, do not model drag on particles at high flow rates very well. Although the relative difference changes slightly on account of increasing volume fraction, its sensitivity to flow rate is the deciding factor. From the results it is inferred that at $Re < 1$, all drag models display performance independent of $Re$ with Koch-Hill, Beetstra and Ergun-Wen-Yu models performing better than the other two. For $Re > 1$, the relative difference with the pure CFD results increases exponentially with the Reynolds number for all drag models. For the relative error of drag models, the influence from particulate volume fraction is secondary compared to the effect of flow rate.

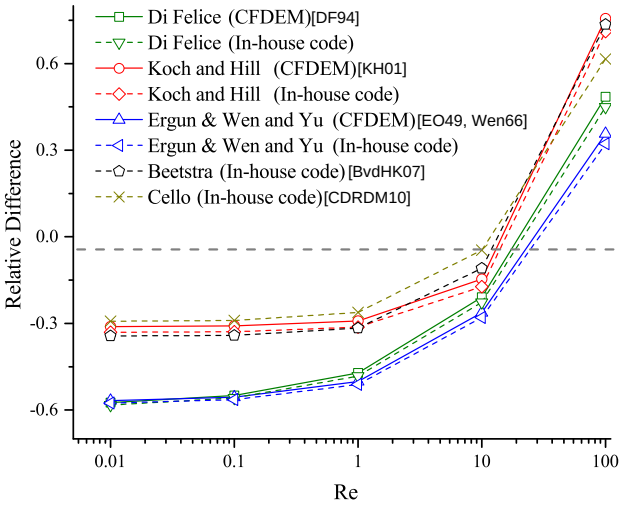


*Config1*

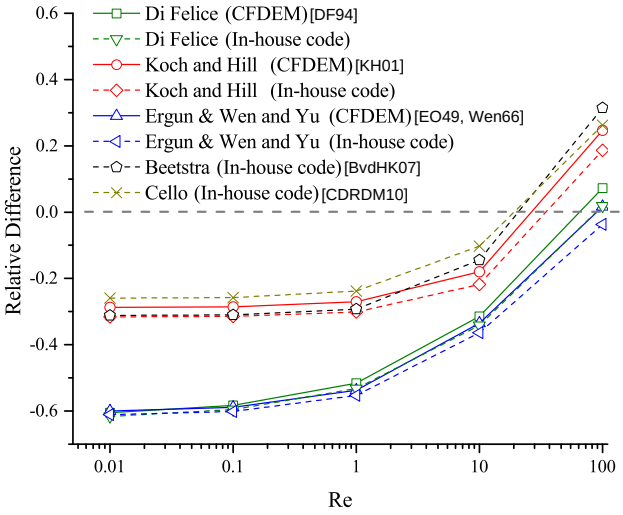


*Config2*

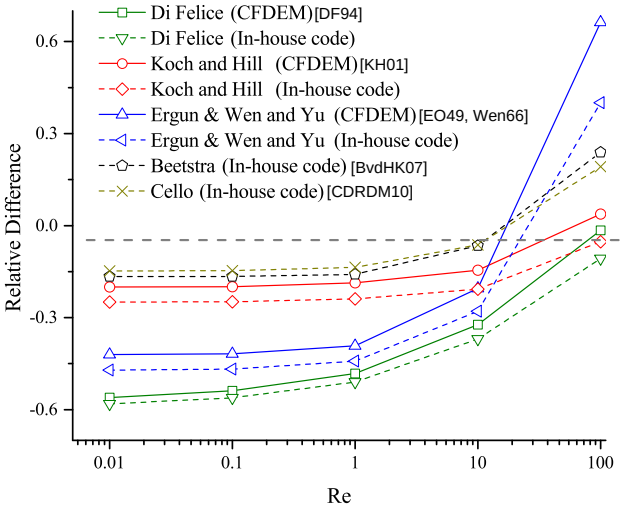


*Config3*

Figure 3.14: Comparison of drag models in the presence of significant particulate volume fraction

## 3.5 The *cross-flow sedimentation* validation test

For a more integrated and unbiased evaluation of CFD-DEM simulation, we introduce a new validation experiment, termed the *cross-flow sedimentation* test. With a main focus on the laminar flow regime of relatively low Reynolds numbers, the *cross-flow sedimentation* test is designed to evaluate the ability of CFD-DEM codes and, in general, multiphase codes to accurately model fluid-particle flows in which both phases have significant influence on each other.

The geometry of the domain used in the *cross-flow sedimentation* validation test is shown in Figure 3.15. It is shown schematically with dimensions in Figure 3.16. Water is pumped through the inlet at a constant flow rate, flows across the horizontal channel, and discharges from an outlet at the other end. With water flowing steadily in the channel, particles are introduced at the particle inlet and allowed to sediment under gravity in the cross-current fluid flow through the horizontal channel. Without the imposed fluid flow, the particles settle and form a pile directly under the inlet. With the imposed fluid flow, the particles are partially carried away by the flow, and a pile forms some distance downstream from the inlet. A lab experiment is set up to generate data for validation. Experimental validation is performed with a device based on the Hele-Shaw cell apparatus typically used to experimentally assess quasi-2D fluid flow [ST58]. To fabricate the cell interior, a $1mm$ thick polyethylene terephthalate (PET) sheet was laser cut with the desired flow geometry. Plates of $12mm$ polycarbonate were then fixed either side of the PET to create a closed cell. The flow channel is therefore $5mm$ in height with a $1mm$ inlet above for grain entry. Water is injected at a controlled volume flow rate into one end of the channel with a Harvard PHD ULTRA pump. A closed supply of silica glass beads, sieved to a range of $200\mu m$ to $250\mu m$, in water is attached to the inlet above the cell where they can fall due to gravity into the flowing channel. The behaviour of the beads upon entering the channel is captured with a high-speed camera fitted with a $60mm$ macro lens at 60 and 400 frames per second for the purposes of visual characterisation and particle tracking.

The experiment is carried out for three inlet flow rates of $1.0ml/min$, $2.5ml/min$ and $5.0ml/min$. The particle injection rate is found to be around 20000 particles per minute. Figures 3.23, 3.25 and 3.27 show the results from the experiments. As expected, in each run, the particles are carried downstream by the flow and settle to form a bed. This bed grows in height over time and gradually narrows the cross-section of the channel. The water is thus forced to flow at a greater velocity above the bed. As the bed reaches a certain critical height, the flow velocity approaches a value such that the bed does not continue to grow in height. Instead, newly injected particles are carried downstream and settle at the end of the bed where the flow velocity is low. As a result, the bed continues to grow horizontally in the direction of fluid flow. For higher inlet flow rates, the formation of the bed takes place further down the channel and maximum height of the bed decreases. It is worth mentioning that the achievement of critical height in this experiment bares close resemblance to the critical Shields number which is used to calculate the onset of grain motion in sediment transportation. The critical Shields number is the ratio between shear stress at the top of the particle bed and the apparent weight of a

single particle. For more information refer to [HODJ15, HODJ16, CSOO17, AK17].

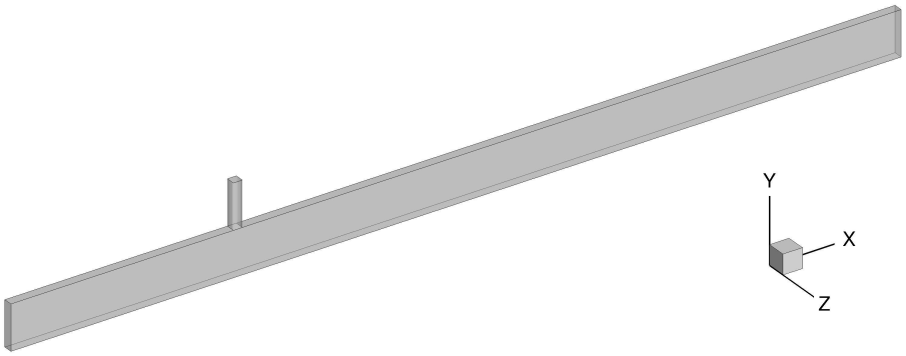


Figure 3.15: Geometry of domain in *cross-flow sedimentation* validation test

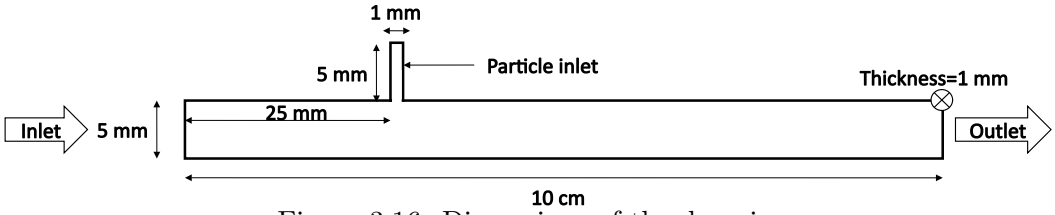


Figure 3.16: Dimensions of the domain

The growth of the particle bed and subsequent achievement of the critical height involves significant two-way fluid-particle interaction. A properly implemented CFD-DEM simulation system should be able to capture the phenomena involved. The Reynolds number of the flow is $< 1$ in the experiment. From the previous section, it is evident that all drag models, in this regime, perform well and only differ from the *ANSYS* results by a constant factor $< 1$. The drag model only forms a part of the entire CFD-DEM coupling and thus it can be expected that simulations yield accurate results even with this factor of difference. The choice of drag model, in this case, should not significantly affect the results.

The in-house code is used to simulate the experiment using the Di Felice drag model. The properties of water and particles used in the simulation are given in Table 3.4 and Table 3.3, respectively. Note that the properties of the glass particles were obtained from the manufacturer specifications. Figures 3.24, 3.26 and 3.28 show the results from the code. It can be observed that the particles initially form a bed which grows in height and eventually reaches a critical value. After that, the bed continues growing in the horizontal direction. For greater inlet velocities the bed is formed further down the channel and the maximum height achieved by the bed decreases. The sequence of events matches that of the experiment and confirms that the in-house code is able to model the physical phenomena involved in the *cross-flow sedimentation* test. However, to fully validate the code, quantitative evidence needs to be provided.

Table 3.3: Properties of spherical particles

| **Property** | **Value** |
|---|---|
| Diameter | $200 - 250\mu m$ |
| Density | $2500kg/m^3$ |
| Coefficient of restitution | 0.67 |
| Friction coefficient | 0.3 |

Table 3.4: Properties of water

| **Property** | **Value** |
|---|---|
| Density | $997kg/m^3$ |
| Viscosity | $0.00089Pa.s$ |

It should be emphasized that the sedimentation process is a result of significant fluid-particle interaction. Thus, to compare the simulation and experiment quantitatively, parameters which are sensitive to both the fluid and particle motion should be used. Although data from the simulation results is readily available and can be post-processed as desired, the comparison is mainly limited by the techniques to extract useful information from video records of the experiment. When focusing on the sedimentation process, the most interesting is the critical height. As shown in Figure 3.17, the top of the bed is uneven, therefore while measuring the bed height it is necessary to take an average of a few readings. It is also noticed that there are blurry moving particles on the top. These particles are disregarded while determining the bed height and only settled particles are considered. The bed height in the experiment is determined by averaging the values from a set of 5 points, while the height value for simulation results is obtained in the same way based on the videos created by post-processing.

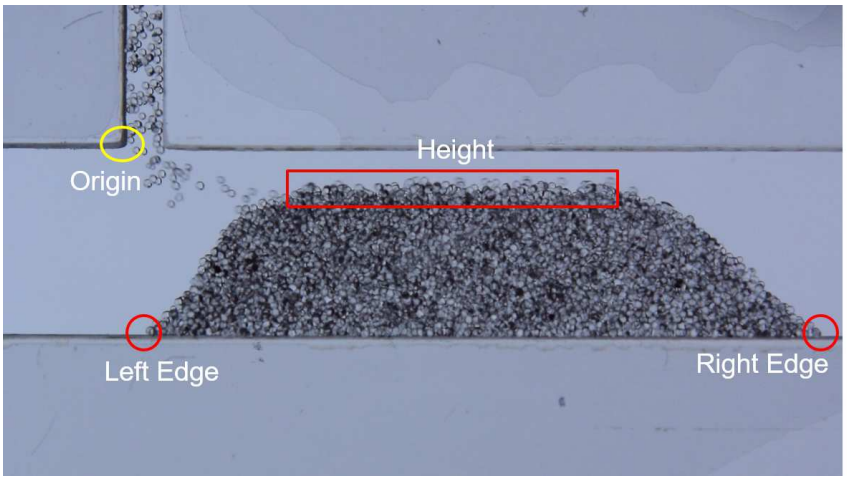

Figure 3.17: Definition of compared indices

Height data from all cases are summarized in Figure 3.18a. The solid lines are generated from experiment results, and the dashed lines are from the simulations. Various colours distinguish the cases with different flow rates at the inlet. It can be seen that the sedimentation process can be divided into three stages: the first is the

initial linearly growing stage, the third is the final steady stage and the second is the transition stage between them. In the first stage ( $0-5s$), all six curves overlap each other with only minor differences between them, which is quite understandable. In this stage, the bed height is low and horizontal fluid flow has a limited effect on the particle movement. The particles are mainly driven by gravity. As the injection rate of particles is constant in all six cases, the corresponding curves are close to each other. In the third stage ($10-20s$), there is only a narrow gap left for fluid to flow above the bed, which means that the fluid is forced to flow at a higher velocity in this zone. The change is enough to not allow particles to settle on top of the pile. Thus, in this stage, the particle movement is mainly dominated by fluid velocity and the resultant drag force, and the height of bed fluctuates around a constant value. This value indicates a certain critical height for which the drag force and the resistance between particles are in the balance. Therefore, Figure 3.18a shows that the critical height decreases when flow rate increases because drag forces increase. The second stage ($5-10s$) is where both fluid velocity and gravity affect particle movement significantly and neither dominate. In this stage, the bed is high enough to disturb the fluid velocity but drag force on the particles is still smaller than the forces between particles. Due to the complexity, the curves still overlap in this stage, but the trends indicate that the growth rate of height decreases gradually. The curves produced by the experiment and simulation follow each other quite well, reinforcing the claim that the simulations reproduce experimental results with a high degree of accuracy.

Besides the height, there are two other meaningful parameters which can be obtained directly: left and right edges of the bed (defined in Figure 3.17). The left edge is the starting point of the bed. This value is affected by the inlet flow rate. As described earlier, under higher flow rate, the bed will form further down the channel and along with it the left edge. To determine the value (only horizontal coordinate) of the two edges, the left edge of the particle inlet is set to be the origin (the yellow circle in Figure 3.17). The data for the left and right edges are shown in Figures 3.18b and 3.18c respectively. It can be clearly observed in Figure 3.18 that simulation results match very well with experimental results when comparing with all three parameters. Therefore, it can be concluded that the in-house code is capable of reproducing the *cross-flow sedimentation* test quantitatively. In addition, it is worth mentioning that, the *cross-flow sedimentation* test is able to generate stable output when repeated several times in the lab. The reproducibility and easy-to-obtain parameters of the test make it a suitable benchmark validation for CFD-DEM strategies. The simulations were carried out using the other drag models mentioned in this paper and results obtained were very similar to ones obtained using the Di Felice drag model. These results look identical with only subtle differences and therefore have not been included in this paper. This too matches our expectations that the choice of drag model doesn't play a crucial role in the case of low Reynolds number problems like in the *cross-flow sedimentation*.

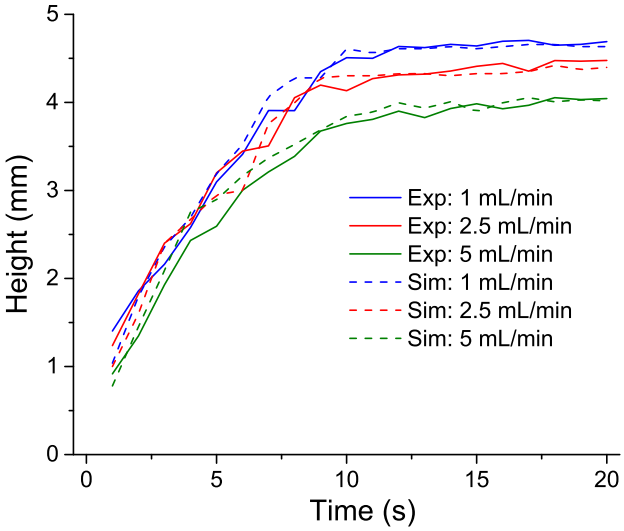


(a) History of height

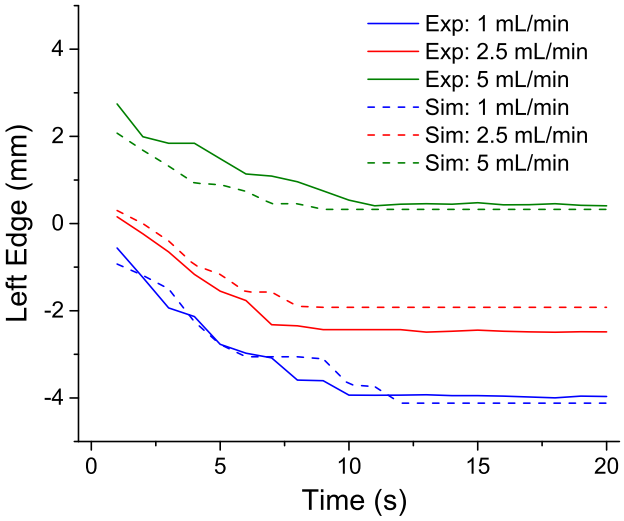


(b) History of left edge

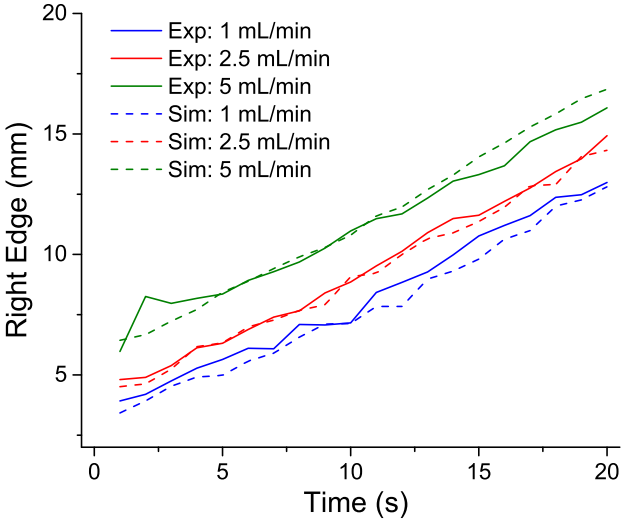


(c) History of right edge

Figure 3.18: History comparison of experiment and simulation

In order to obtain a useful comparison of grain trajectory and velocity between the experimental and simulated flows, particle tracking velocimetry (PTV) is employed with the open-source algorithm TracTrac [Hey19]. Images of the experiment captured at 400 frames per second and video output of the simulation obtained at 500 frames per second are subjected to PTV at selected stages of flow, with analysis taking place over one second of real-time data. Figure 3.19 displays the trajectory and average velocity magnitude of grains flowing over a duration of a second in both experimental and simulated flows at four stages of time. The flow rate is $5ml/min$. Good agreement is observed with regards to velocity magnitudes and trajectories. Interestingly, there are subtle differences, notably that the grain flow paths have a greater spread in the experiment, with slightly more variation in velocity. This is possibly due to the presence of a grain size distribution in the experiment that is not accurate represented in the simulation, with larger particles being less influenced by fluid drag. Another possible reason is that particles in the simulation are released at regular intervals in time from predefined locations evenly distributed over the cross-section of the particle inlet. Thus the particles tend to stay away from the inlet walls reducing the spread.

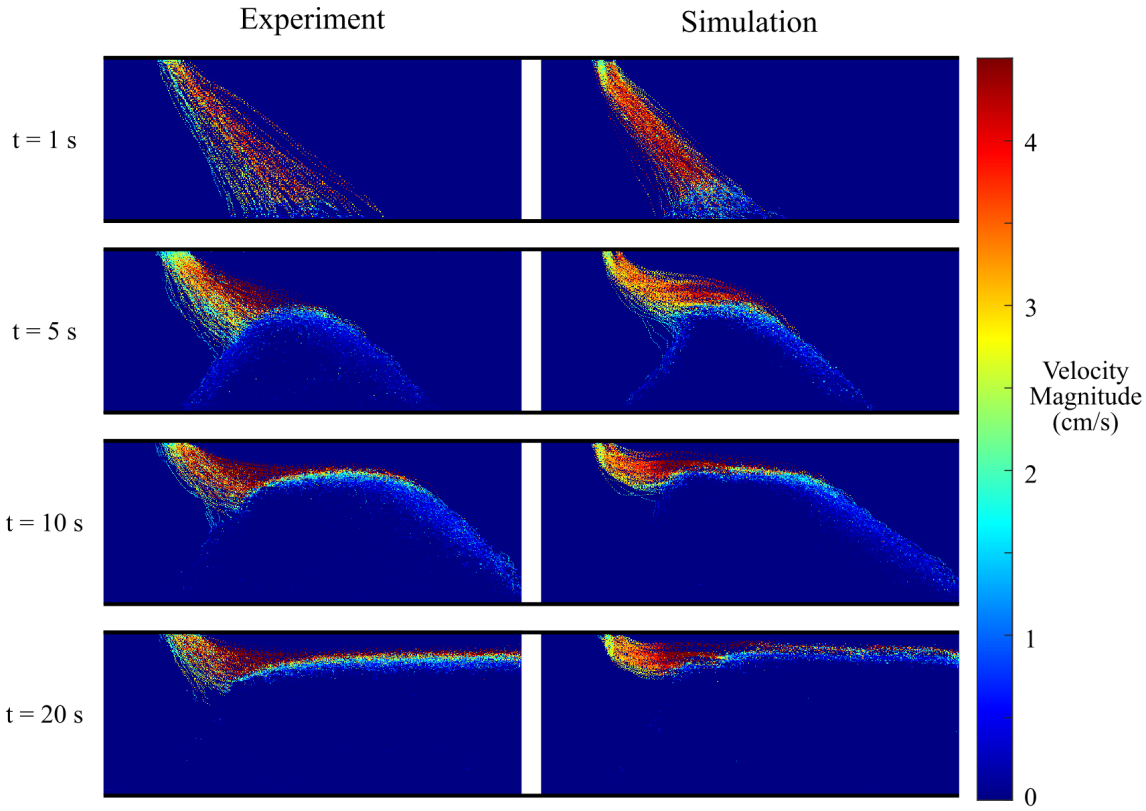


Figure 3.19: Velocity magnitude and trajectory at various stages in simulation and experiment ($5ml/min$)

The simulation results can also be comprehensively presented by means of particle residence time, which are given in Figures 3.20, 3.21 and 3.22. The residence time of a particle is defined as the time elapsed since the particle is injected into the system. From the figures it is clear that the oldest particles are found where the initial bed

was formed with a few being pushed downstream (blue colour). A layer of slightly newer particles (green colour) is formed on either side of the oldest particles. The newest particles (yellow and red) were introduced into the system when the bed had grown to its maximum height and were carried downstream towards the end of the formed bed and hence settled downstream. Red particles found at the top were being carried downstream when the simulation was stopped at $20s$.

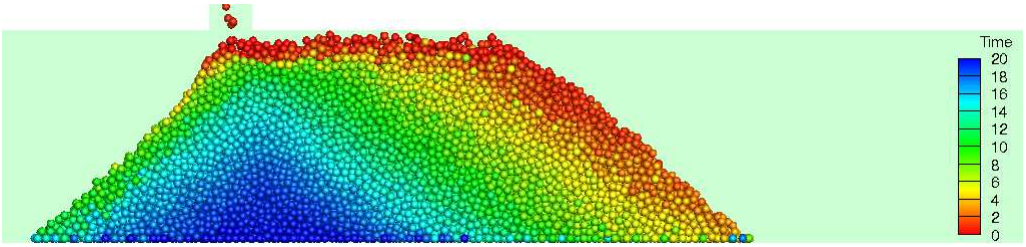


Figure 3.20: Particle residence time for flow rate 1 ml/min

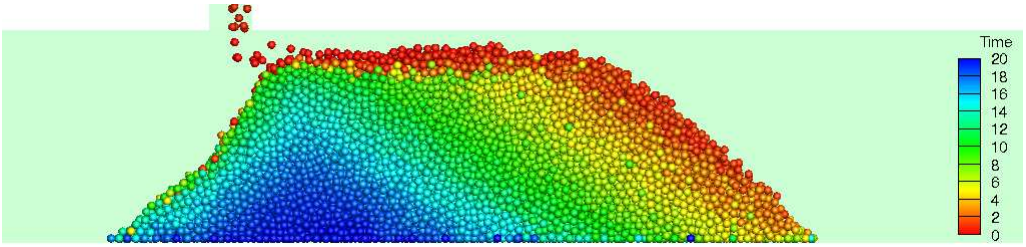


Figure 3.21: Particle residence time for flow rate 2.5 ml/min

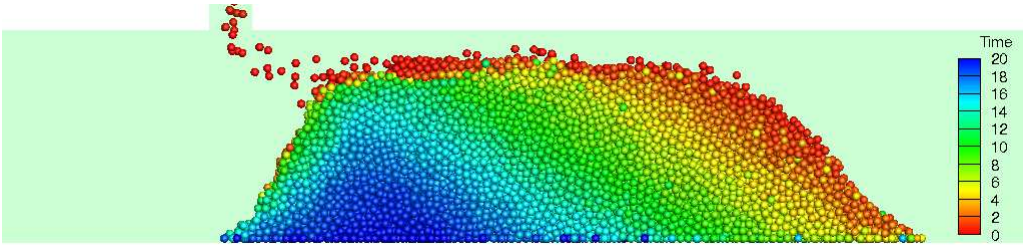


Figure 3.22: Particle residence time for flow rate 5 ml/min

The above results and analysis confirm that the in-house code can provide physically accurate simulation results even in conditions where fluid flow and particulate movement have a large influence on each other and interact with each other to produce highly complex phenomena. In addition, the proposed *cross-flow sedimentation* validation test is simple and easy to reproduce, adjust and take quantified measurements. The new test is designed mainly for the laminar flow regime with low Reynolds numbers, and it serves as a good complement to the popular fluidised bed experiment for CFD-DEM validation.

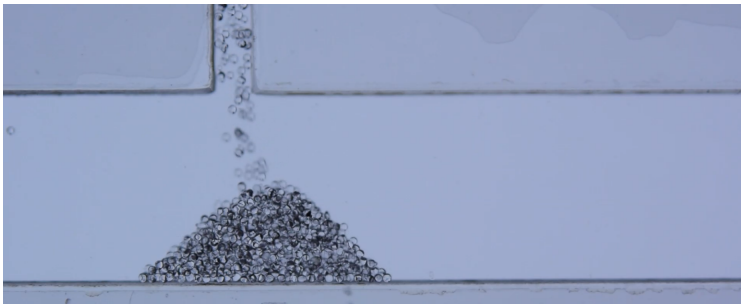

$4s$

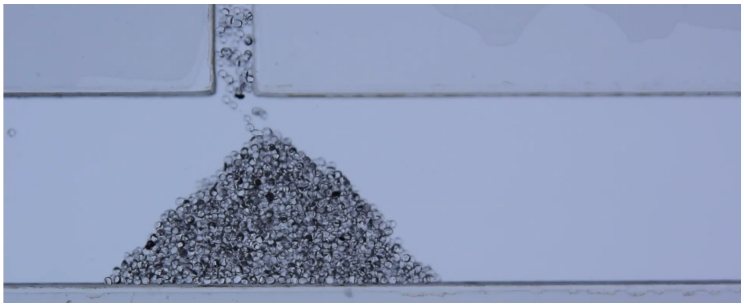

$8s$

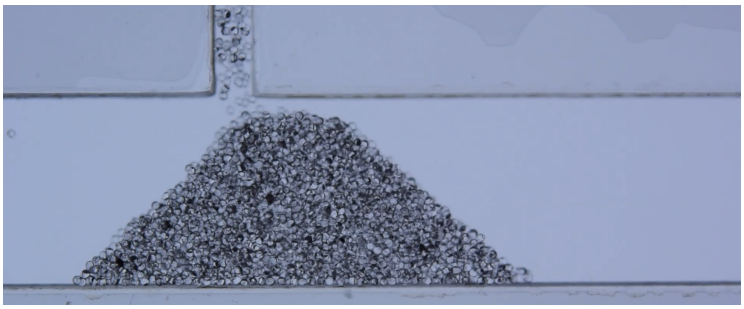

$12s$

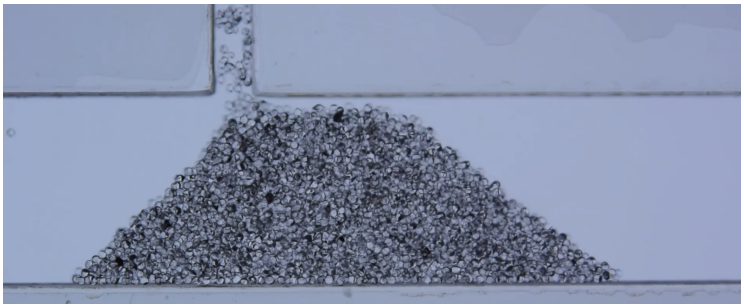

$16s$

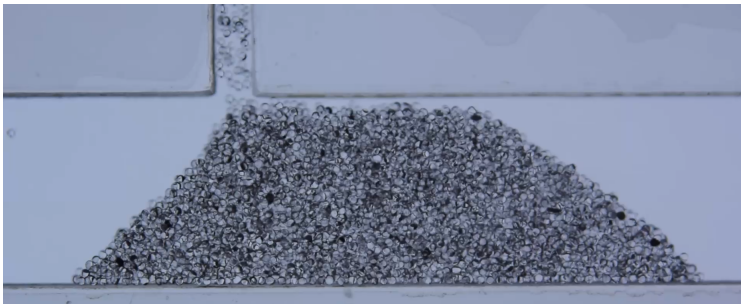

$20s$

Figure 3.23: Results of the *cross-flow sedimentation* lab experiment for inlet flow rate of $1ml/min$

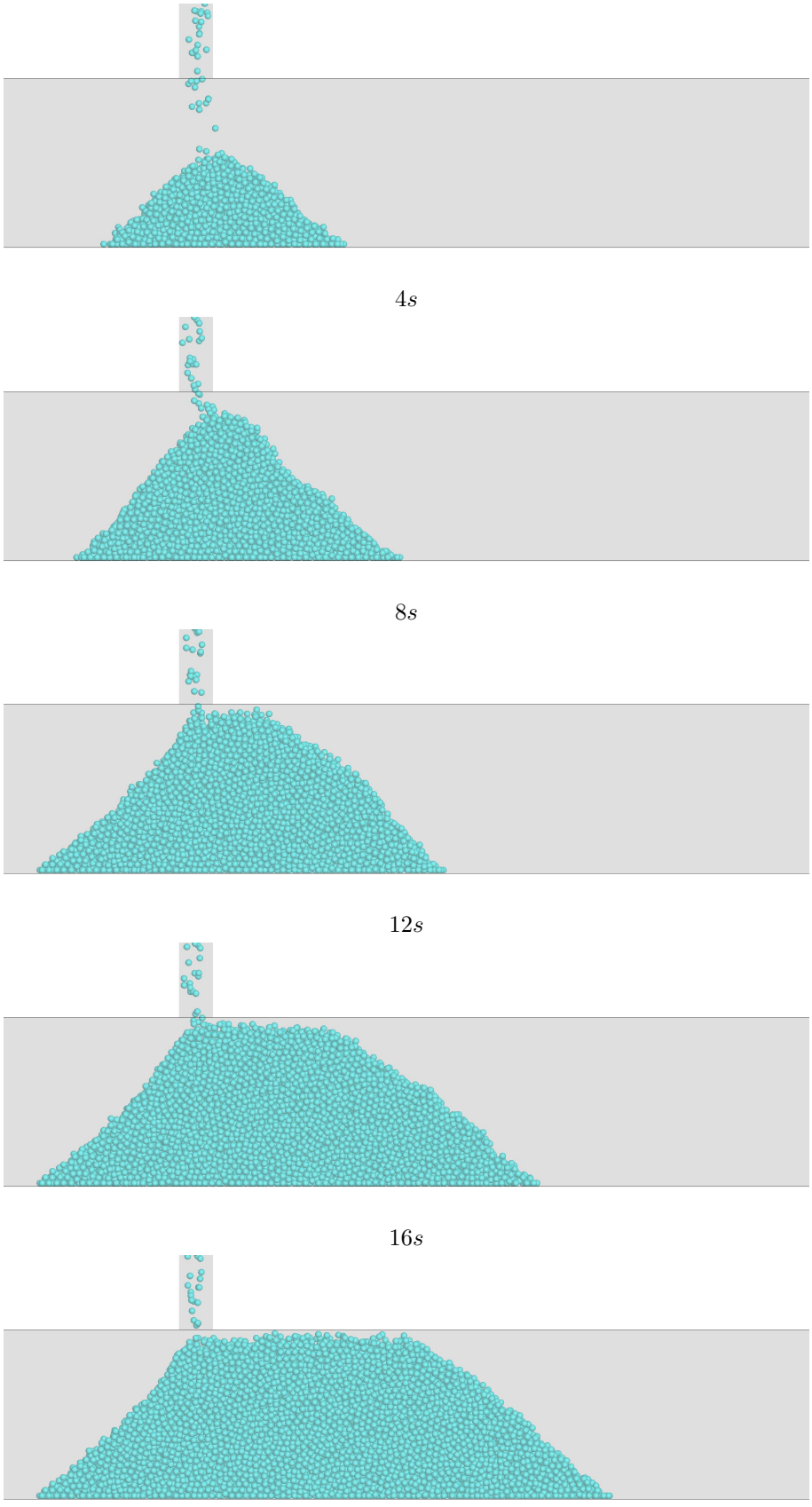


Figure 3.24: Results of the *cross-flow sedimentation* simulation for inlet flow rate of $1ml/min$

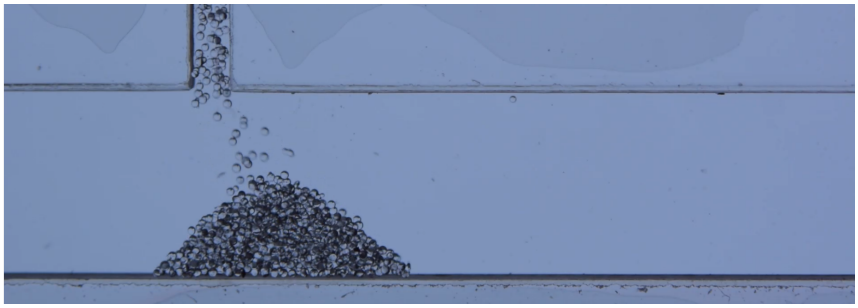

$4s$

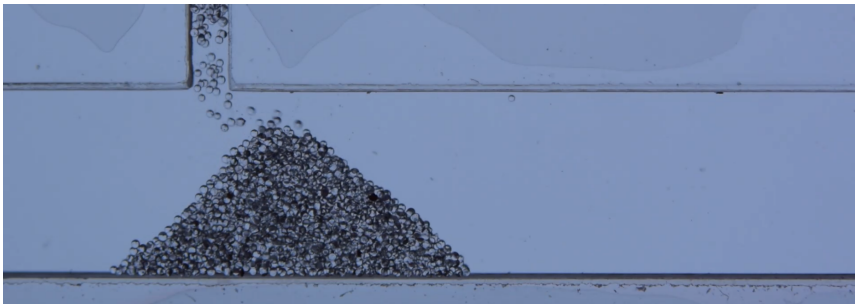

$8s$

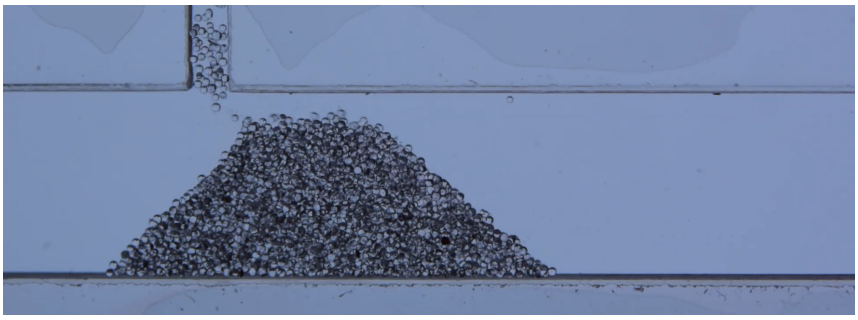

$12s$

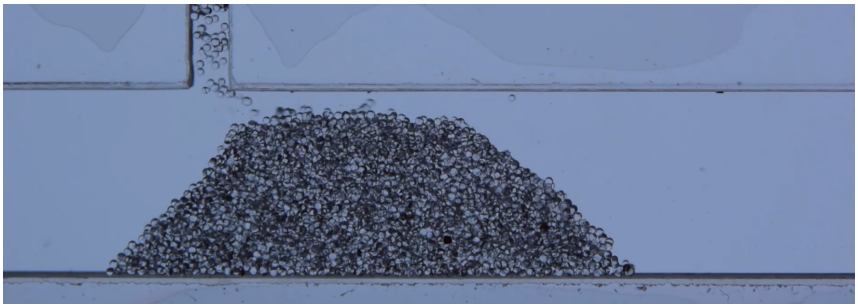

$16s$

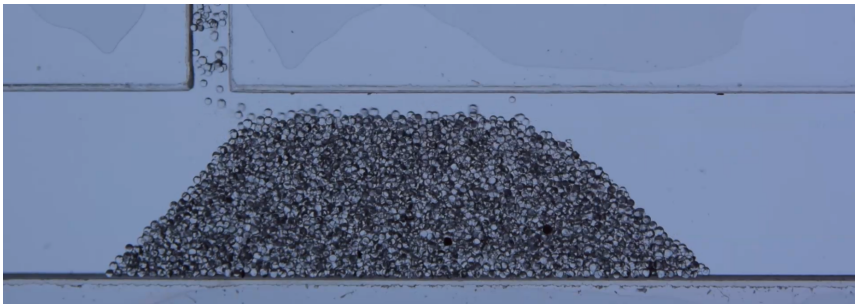

$20s$

Figure 3.25: Results of the *cross-flow sedimentation* lab experiment for inlet flow rate of $2.5ml/min$

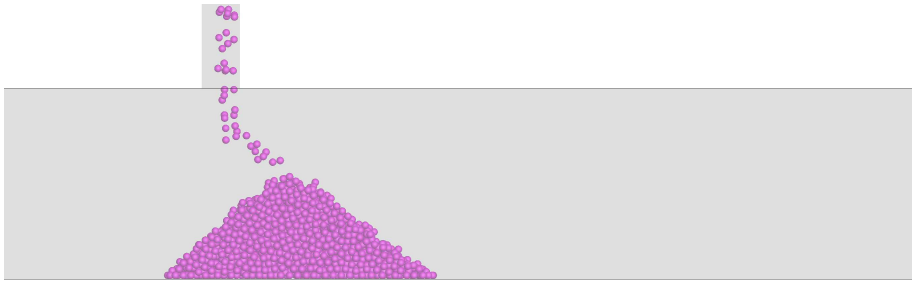

$4s$

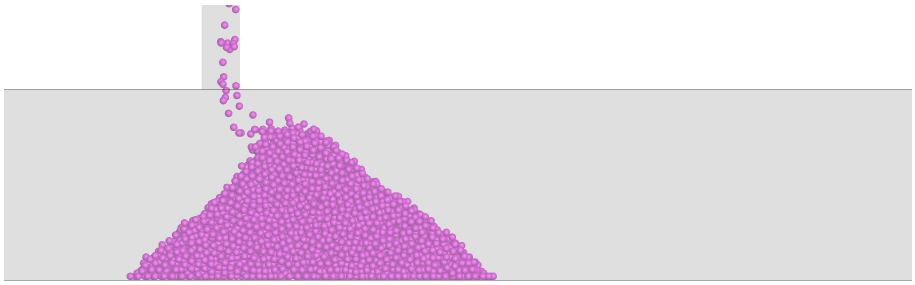

$8s$

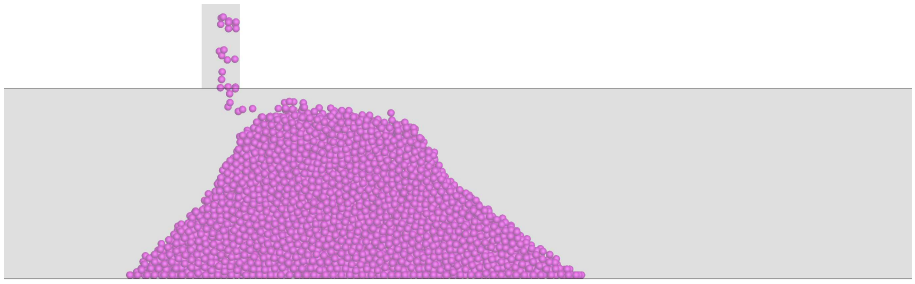

$12s$

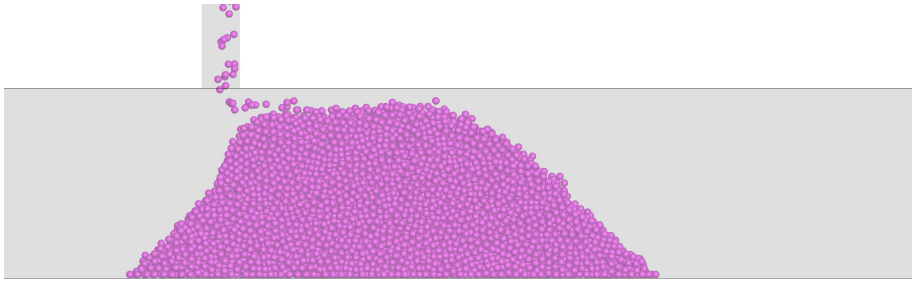

$16s$

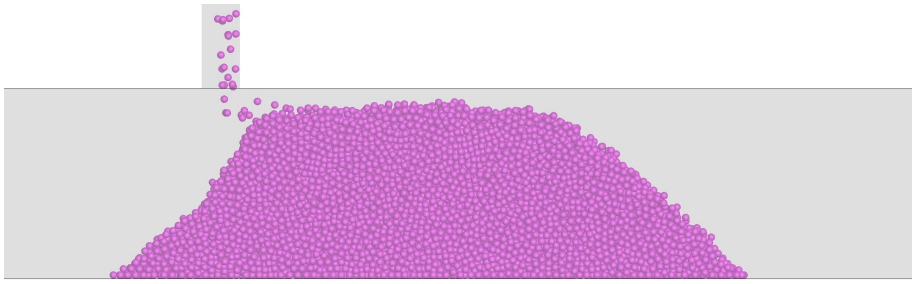

$20s$

Figure 3.26: Results of the *cross-flow sedimentation* simulation for inlet flow rate of $2.5ml/min$

$4s$

$8s$

$12s$

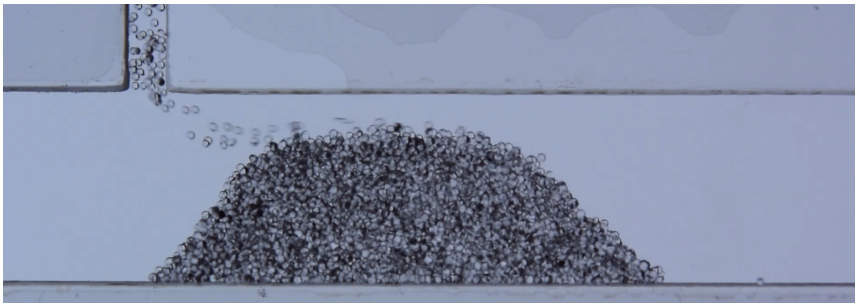

$16s$

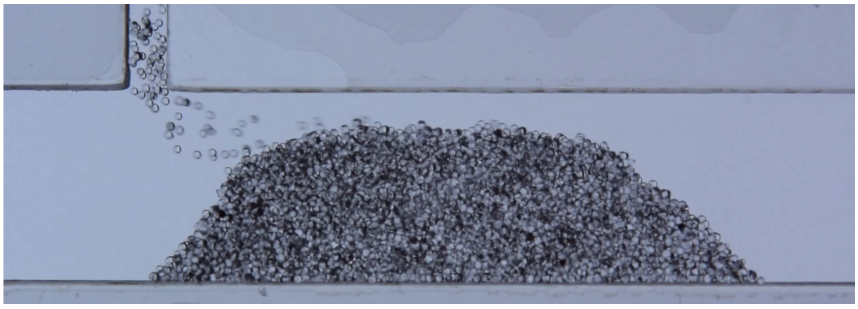

$20s$

Figure 3.27: Results of the *cross-flow sedimentation* lab experiment for inlet flow rate of $5.0ml/min$

$4s$

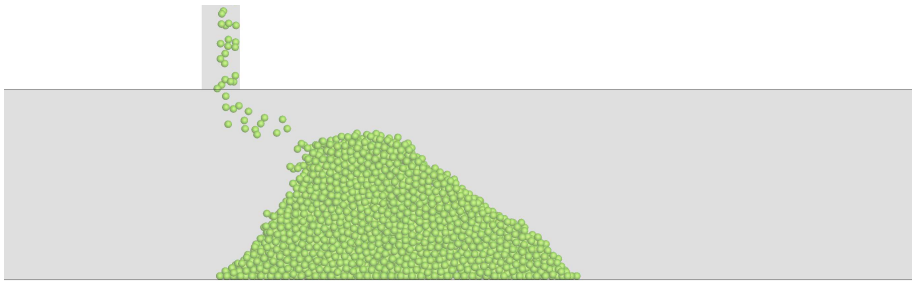

$8s$

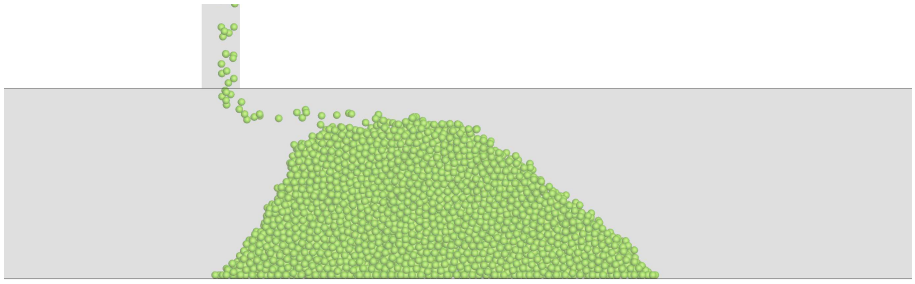

$12s$

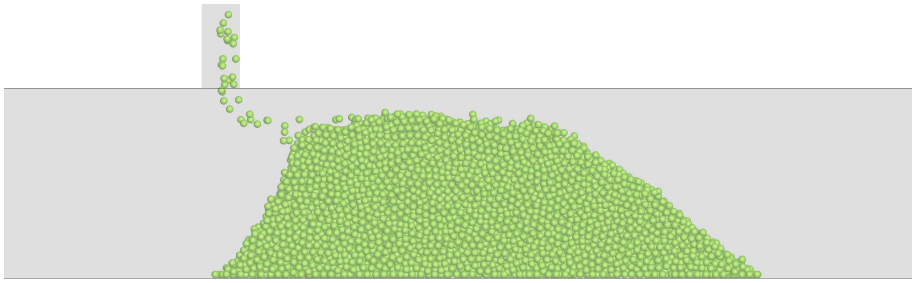

$16s$

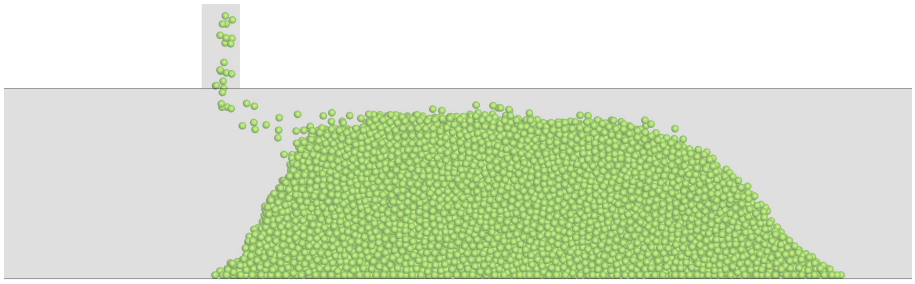

$20s$

Figure 3.28: Results of the *cross-flow sedimentation* simulation for inlet flow rate of $5.0ml/min$

## 3.6 Conclusions

CFD-DEM is a numerical methodology to model fluid and solid particulate multiphase flow problems. It has important applications in many natural and industrial processes. The drag models, which dominate the fluid-particle interaction in many practical multiphase flows, differ greatly in their formulations, but independent assessments on their applicability in different physical conditions are rare. In addition, the complex nature of CFD-DEM simulation makes it difficult to conduct integrated and unbiased performance evaluation. As a result, significant modelling uncertainties are encountered in the practical use of CFD-DEM simulation. Through a series of comparisons with well-established phenomenological formula, proven CFD solver, independent CFD-DEM codes and experimental tests, this study systematically evaluates commonly used drag models and clarifies/eliminates some of the modelling uncertainties of CFD-DEM simulation. The main findings are listed below:

1. Although all drag models perform well in the case of drag on a single particle, the Di Felice [DF94] and Ergun-Wen-Yu [EO49] models were found to better follow the well established empirical expression for terminal velocity than the other three models.

2. With the presence of a swarm of particles and low Reynolds number $Re < 1$, all drag models under-predict the drag force by a constant factor, which may not cause a real concern in practical applications as the error can be easily compensated via straightforward model calibration.

3. With the presence of a swarm of particles and Reynolds number greater than unity, the errors of all drag models grow exponentially with the Reynolds number, while the particle volume fraction is of secondary importance for the performance of drag models.

4. A new validation experiment, termed the *cross-flow sedimentation* test, is proposed for integrated performance evaluation of CFD-DEM simulation. Designed for low Reynolds number scenarios, the *cross-flow sedimentation* test is easy to implement, control and quantify measurements, providing a good complement to the popular fluidised bed experiment for CFD-DEM validation.

In this chapter we have seen the CFD-DEM approach of modelling fluid-particulate muliphase flow in detail. In the next chapter we will shift our focus to potential applications of multiphase flow modelling. In particular, the modelling of fresh concrete flow will be looked at in great detail. The scope of modelling concrete flow using multiphase techniques is huge as the industry has been largely unsuccessful in coming up with solutions to the many problems it faces by purely performing experiments. There is now a consensus within the industry that numerical modelling is the only way forward in the research of fresh concrete flow technology. With that in mind concrete rheology and research surrounding it is introduced in the next chapter.

# Chapter 4

# State-of-the-art review on numerical modelling of fresh concrete rheology

This chapter introduces one of the potential industrial applications where multiphase flow modelling could be used to gain a better understanding of the underlying physics. The ultimate goal is to answer questions or find solutions to the common challenges faced by the industry using numerical simulations especially in circumstances where experimental approaches fail to deliver. The application in concern is the modelling of fresh concrete flow and will be looked at in detail in this chapter. It is important to understand the basics of fresh concrete rheology and the problems faced by the industry during the placement process. This chapter covers various commonly-observed construction defects associated with the behaviour of concrete flow and the complex physical-chemical interactions occurring in the concrete mix. It visits the existing lab based experiments or tests used to understand and/or quantify its behaviour. There has been a considerable amount of research surrounding the numerical modelling of fresh concrete flow and a detailed analysis on it is presented in this chapter. The literature is rigorously classified following specific rules, with critical comments drawn from evidenced-based discussions. The correlation between various research works are analysed to clearly depict the progress of this fast-growing research field.

## 4.1 Introduction

Concrete is one of the most widely used materials in the world. Ancient Egyptians used calcined impure gypsum. The Greek and Romans then used calcined limestone and added lime, water, sand and crushed stone to form the first concrete in history [Nev95]. Over thousands of years this composite has been improved and mixed with other materials eventually transforming into modern concrete widely used today in almost all construction works. The first reinforced concrete structure was built in 1875 in the United States at Port Chester, New York [MB15]. Reinforced cement concrete (RCC) enabled engineers to design structural components using concrete which could withstand high tensile forces, leading to a revolution in

the infrastructure industry. Modern RCC structures are constructed by installing temporary works into which concrete is placed and left to harden. Freshly poured concrete has to flow around reinforcement bars, take the shape of the formwork and form a level surface. However concrete, in the fresh state, is a highly viscous material and requires the application of compaction techniques for it to flow freely. Concrete vibrators like formwork vibrators, jumpers and internal vibrators are used to achieve this. Durability of the RCC structure depends on the amount of compaction, the inadequacy of which can lead to serious defects. However, the compaction operation is not always feasible in practice due to restriction in access or skilled labour, which pushed the construction industry to design concrete requiring no or minimum compaction. In 1988, self compacting concrete (SCC) was introduced [OOO00]. It is a highly flowable variant characterised by high dosages of admixtures and super-plasticisers. Compaction of SCC occurs by virtue of self-weight, avoiding the need of additional compaction.

This thesis focuses on the flow behaviour of such highly flowable variants of concrete. SCC is used for pre-cast applications as well as for on site casting. Tremie concrete is widely used in deep foundation construction. These highly flowable concretes are typically prepared in a site batching plant or a ready mix concrete plant and delivered to the site by truck. They are placed in the formwork by pumping or pouring. Various versions of highly flowable concrete exist based on the application it is used for. A high slump version of pre-cast concrete is being promoted in the industry as many products have small reinforcement spacing and difficult dimensions where vibrators cannot be used to promote compaction [BSS11]. Pre-stressed bridge girders with effective spans ranging from 10m to 150m are being cast using SCC. The advantages of using SCC to construct tunnels is also evident. Concrete is required to be filled in the slot between covers of the formwork. Due to the limited access, it is difficult to get concrete to fill the form. Thus a concrete with higher slump is required in such applications. An interesting variant of concrete called shotcrete, i.e. concrete which is sprayed pneumatically at high velocity onto a surface, is being used to line tunnel walls [Bea94]. Dimensions of tunnels can range from tens of metres in diameter to tens of kilometres in length. A typical concrete lined tunnel is shown in Figure 4.1. As time progressed, structures became taller, heavier and increasingly complex. Any structure ultimately passes its load to the earth, making the substructure a crucial component. To support the increased loads of modern structures, foundations got deeper. Ordinary concrete cannot be used in the case of deep foundations where it is difficult or even impossible to execute standard compaction techniques. Hence, tremie concrete, a close relative to SCC was introduced. It is designed to achieve full compaction when placed using a tremie-pipe in deep foundations, under submerged conditions [ED18]. It is thus used to cast bored piles with radii ranging from 1m to 3m and depth of 10m to even 100m. Figure 4.3(a) shows the placement process of a bored pile. Tremie concrete is also used to cast diaphragm wall panels of width ranging from 600mm to 1500mm and lengths of 2.5m to 7.5m as shown in Figure 4.3(b). SCC can also be used as a replacement for ordinary concrete in usual applications like casting of slabs, beams and columns especially when compaction techniques are not available due to lack of equipment or skill. Figure 4.2 shows a slab being cast using SCC.

Figure 4.1: Concrete lined tunnel

Figure 4.2: Application of SCC

Although SCC and other highly flowable concretes are widely used in the construction industry, their flow behaviour is very poorly understood and much less researched compared to other widely used engineering materials. In reality concrete is a very complex material which exhibits time dependent properties and unusual behaviour determined by the complicated physical-chemical interactions among its ingredients. As structures get bigger, foundations deeper and the reinforcement denser it has never been more important to understand better the behaviour of this common material. Understanding the rheology of concrete and the flow behaviour during practical constructions is critical for improving the mix design, the placement method and the construction quality.

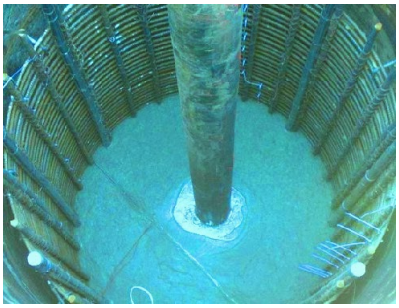

(a) Pile

(b) Diaphragm wall

Figure 4.3: Applications of tremie concrete

Lab-scale experiments and field tests have been carried out to study the rheology of concrete [BPLH13]. Standard industrial or specially designed lab tests are often used to study the workability of fresh concrete and the quality of mix design. Although rare, large scale field tests have been performed to investigate the bulk flow of fresh concrete during the construction process. Experiments at the field scale are expensive to conduct and also hard to gain reliable information due to the lack of technology to monitor concrete flow during construction. Numerical simulations offer an alternative approach to study concrete flow [GS11]. Flow behaviour and phenomenon such as blocking and segregation of aggregates can be studied using modelling [RGD+07]. It also has the capability to offer better understanding of concrete rheology and the effect of mix design on the construction practice.

Since the advent of SCC, admixtures and highly flowable concretes have been under rapid development, and they have completely changed the design practice of

concrete mix. Better understanding the rheology of concrete becomes increasingly more important for both construction practice and structural quality. The limitations of experimental research have led to an increasing interest in numerical simulations of concrete flow. Figure 4.4 shows the number of papers published each year on concrete flow research. The research field began in the late 1980s and the number of papers published has been increasing steadily, with a rapid growth in the past few years. Figure 4.5 shows the publications according to the country of authors. Most of the numerical research has been carried out in Europe and Asia. In summary the field of concrete flow simulations is at its early stage but is growing rapidly in the industry as well as in the research community [RGC+16].

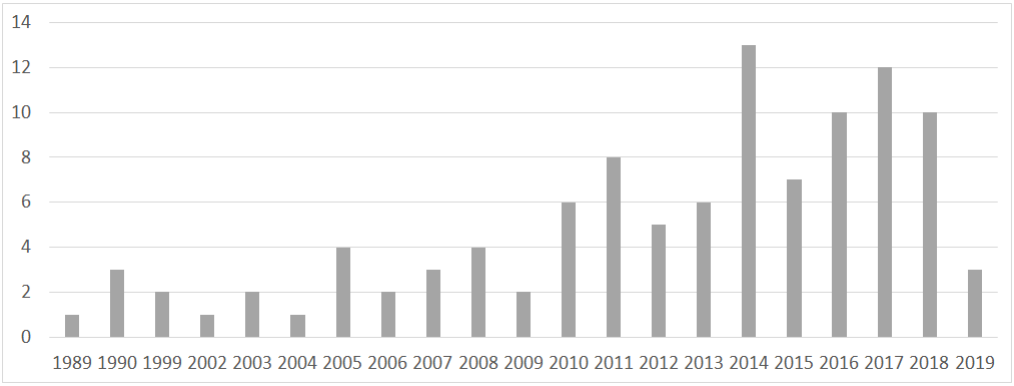

Figure 4.4: Number of papers vs year of publication

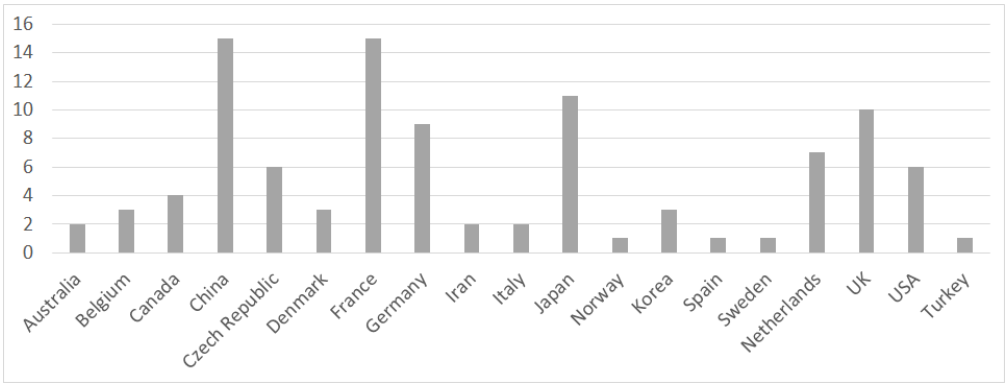

Figure 4.5: Number of papers vs country of research

In the following section self-compacting concrete as a material is introduced and the defects associated with its placement are explored. Further the behaviour of fresh concrete and the physics which govern it are discussed. The need to model it using mathematical expressions is emphasised upon. The Bingham fluid model is formally introduced. In the third section, lab and field based experiments and tests to study fresh concrete property and their limitations are stated. In the fourth section, use of numerical modelling and simulation technology as an alternative to study fresh concrete flow is introduced and the various numerical techniques used in literature are investigated. A thorough literature review surrounding fresh concrete numerical modelling is conducted. In section five the literature is classified based on various criteria and is critically analysed. In the final section, conclusions are drawn based on the discussion.

## 4.2 Problem and physics

In this section, concrete and its basic properties are first discussed from an engineering perspective, where the practical problems encountered during the placement process are highlighted. Then the behaviour of fresh concrete and the underlying physics are elaborated and a few models to describe certain aspects of fresh concrete behaviour are introduced.

### 4.2.1 Description of concrete and defects during its placement

Concrete is a man-made material consisting of inert particulate matter called aggregate that is bound together by cement and water. Water makes the concrete mix easily flowable and therefore affects an important property of fresh concrete called workability. A concrete mix said workable if it can be easily transported and placed. However the addition of water compromises another important property of concrete called strength. A high water-cement ratio (w/c) can cause flaky cement pastes, reducing the final strength of hardened concrete. Cement or Portland cement is composed of alumina, silica, lime, iron and gypsum. Cement hardens when these substances exothermically react with water. This process is known as the hydration of concrete. Once hardened, cement acts as a binder, binding all ingredients of concrete together. Hydration of cement is an infinitely long process the rate of which decreases exponentially with time. However, concrete achieves 99% of its strength in the first 28 days [Li11]. Aggregates can be further classified as coarse and fine, both of which help increase the strength of concrete above what cement can provide on its own. The size, texture and shape of aggregates have a huge influence on the workability and strength of concrete. Smooth rounded aggregates make the concrete more workable, however the use of rough angular aggregates increases the final strength. Modern concrete also consists of admixtures, which change the property of concrete to accomplish a variety of goals. These include faster curing time, increasing final strength, improving the flowability, delaying the onset of hydration process etc. Such additions as fly ash and silica fume are also commonly used in modern concrete mix to improve or achieve certainty aspects of concrete properties, e.g. to improve corrosion resistance and to reduce heat generation during hydration. The quality and quantity of the constituents also affect an important property of concrete known as durability. Durability is the ability to resist weathering action, chemical attack and other environmental factors. Concrete is thus a mix of relatively simple ingredients that interact with each other to form a material with complex behaviour involving multiple physical phenomena.

It is clear that the property and quantity of various constituents of concrete determine its basic properties namely, workability, strength and durability. Mix design is a process of selecting suitable ingredients and determining their relative quantities to achieve, as economically as possible, the required basic properties. The main characteristic of highly flowable concrete like SCC is its high workability. The fluid nature is not achieved by the addition of high proportion of water, but rather the high proportion of fine aggregate combined with super-plasticisers and viscosity

enhancing admixtures. The high viscosity gives SCC good resistance to separation of particulate matter. This property is known as the stability of concrete.

Despite the best efforts by engineers to produce mix designs which match all workability and strength requirements, imperfections in concrete are witnessed on a regular basis. Imperfections, by definition, are deviations from the design quality and regular continuity of the cast in-situ concrete. They are caused by concrete which does not have appropriate flow properties or adequate stability for the placement procedure. It can also be caused due to poor workmanship. Imperfections are not necessarily defects but can turn into them if they are frequent [ED18]. Although a single cause does not exist for the formation mechanism of imperfections they can usually be attributed to dense reinforcement obstructing the flow, cover zone thickness, mixing of other materials, irregularities during the placement process, insufficient workability time and the instability of concrete. Systematic imperfections in tremie concrete placement can fall into one of the three categories, namely inclusions, channelling and mattressing. Figure 4.6 shows an example of inclusions in piles. They consist of entrapped material with the foundation that does not conform to the reference concrete. This anomalous material may be a mixture of the support fluid, excavated material and the concrete from the interface layer or cementitious material originating from segregated concrete. If inclusions are extensive and frequent, they may affect bearing capacity and durability by occupying wide parts in the cover zone. Inclusions of these dimensions are classified as defects. Channelling or bleed channels are vertical narrow zones with lightly cemented aggregate that lack fines and cement matrix. They are usually found at the surface of the structure. It is mainly caused because of poor segregation resistance i.e. insufficient stability for placement conditions. Figure 4.7 shows an example of channelling in pile. Mattressing describes vertical and horizontal linear features extruding from reinforcement bars. The feature emanates at the reinforcement with material trapped in the shadow zone of the rebars. Mattressing can interrupt the entire depth of concrete cover to the reinforcement affecting durability and bearing capacity. They are formed because of restricted horizontal flow through reinforcement combined with insufficient vertical flow due to lack of free flow around the reinforcement bars. Energy applied to concrete, flowability, stability and passing ability together with cage congestion and concrete cover dimension contribute to mattressing. Figure 4.8 shows an example of mattressing in a panel.

Figure 4.6: Inclusion

Figure 4.7: Channelling

Figure 4.8: Mattressing

Other surface imperfections found in almost every type of concrete structure are blowholes, crazing, dusting, flaking and honeycombing (Figure 4.9). Blowholes are

rounded cavities that are formed against formwork and become visible when taken off. They are more prevalent at the top of placement than at the bottom, due to the increased pressure at the bottom. They are caused by poorly proportioned sticky concrete mix and insufficient vibration. Crazing is a network of cracks at the surface of structures. They can lead to structural and serviceability problems and there lies no repair method. It is caused due to overly wet mixes, delayed commencing of curing process and removal of bleeding water. Dusting of floors occurs when bleed water is still rising to the surface after placement of concrete and is associated with inadequate compaction. Flaking occurs when discrete pieces or flakes detach from the structure surface leaving an indentation behind and are caused by the same factors as that of crazing. Honeycombing refers to voids caused by mortar not filling spaces between aggregates. Extensive honeycombing severely affect durability and strength. They are caused by lack of fines in the mix, inadequate workability, stability issues and blocking. Defects lead to delays in construction costing the industry a lot of money. More alarmingly, they put public safety at risk as structures becoming larger, more complex and heavier. All these are evidences that a better understanding of fresh concrete rheology is urgent.

(a) Blowholes

(b) Crazing

(c) Dusting

(d) Flaking

(e) Honeycombing

Figure 4.9: Other defects

### 4.2.2 Behaviour of fresh concrete and the underlying physics

To accurately understand the behaviour of fresh concrete is not a trivial task. Multi-physics processes take place within the mix and they give fresh concrete complex rheological properties. Interaction between the individually simple ingredients is at the heart of this unusual behaviour. Thus understanding these interactions can lead to a better comprehension of concrete rheology. The various physical-chemical interactions affecting concrete rheology include cement-water, aggregate-suspension and admixture-concrete etc. These interactions may either be macroscopic or microscopic. Hence concrete rheology is also a multi-scale problem.

The mortar-gravel interactions occur at the macro-scale and various phenomena associated with concrete defects are related to this type of interaction. Dense inert non-colloidal gravel is suspended in a comparatively less dense mortar paste. The volume fraction, shape and size of the coarse aggregate have a vital influence on the properties of fresh concrete. When a shear is applied to concrete, the shear stress developed is an addition of the shear resisted by the mortar matrix and the aggregate. Friction and collision between the coarse particles make the mixture less fluid. Also interlocking of angular aggregates resists the flow of concrete. The density difference between the mortar and gravel results in the heavier phase segregating from the suspension. Segregation can be classified as either dynamic or static [RG14]. Static segregation occurs when the concrete is at rest. This happens when the force applied on the mortar by aggregates, getting pulled down due to gravitational forces, is close to the yield stress of the mortar. A low viscosity mortar contributes to this effect. Dynamic segregation happens when the concrete is flowing. If the drag force applied by the mortar on aggregates is not high enough, the particles are not carried with the mortar. Also particles tend to migrate from high shear zones to low shear zones and lead to segregation. Friction of aggregates with the walls can also cause them to separate. Lastly, since aggregates are rigid, they cannot flow around reinforcement bars as easily as mortar. Systematic blocking is thus witnessed along with the formation of granular arches when the rebar configuration is congested. The physics between mortar and aggregate is more or less similar to the physics between fine aggregate and cement paste and is also at the macro-scale level.

The cement-water interactions occur at the micro-scale level. Many non-contact forces occur in the suspension. They include short distance van der Waals force, electrostatic forces due to ions adsorbed at the surface of the particles and Brownian motion because suspended particles are of the micro-metre scale. Due to Brownian motion, cement particles diffuse through water. As they get close, Van der Waal forces dominate the repulsive forces. Brownian motion is not enough to overcome the short range attractive forces and hence the particles agglomerate. Agglomeration of particles is considered to be at the origin of yield stress of cement paste. The network of attractive particle-particle interactions enable the suspension to resist shear without flowing [RLFC10]. A network breakage occurs when a large enough force is applied. Interactions between chemical admixtures and concrete usually happen at the micro-scale. They have five functions, namely air-retaining, water-reducing, retarding, accelerating and plasticizing. Water-reducing admixtures reduce the water requirement by 5-10%. When cement comes in contact with water, opposite charges on the surface of cement particles make them attract each other and lead to flocculation. Water is adsorbed in the process. Water reducing admixtures neutralise these charges, and particles tend to remain separated. However this reduces the viscosity. Retarding admixtures delay the hydration of cement by forming a protective skin on the particles. Plasticizers are used to decrease the viscosity of concrete. Molecules of lignin, napthalene and melamine sulfonate wrap themselves around the cement particles giving them a high negative charge leading to repulsion of particles [Li11].

The physics involved in concrete behaviour is complex due to its multi-scale and

multi-physics nature. To develop mathematical or computational models to describe concrete behaviour, it is necessary and essential to make simplifying assumptions. Models need to be developed such that they serve their purpose of describing concrete behaviour for a particular scenario. The "bulk flow" of fresh concrete can be modelled by a fluid which flows only when a shear stress, above certain value called yield stress, is applied to it. If the shear stress developed in concrete is below the yield stress, it behaves like a solid. Once concrete starts flowing, shearing is resisted by viscosity of the fluid. This is termed as the plastic viscosity of concrete. The Bingham fluid model which uses these two parameters to describe the rheology of such a fluid is widely accepted and applied to the flow of fresh concrete [TB79]. Mathematically this is defined as follows:

$$\begin{aligned} \tau &= \tau_0 + \mu\dot{\gamma} \quad \text{if } \tau \geq \tau_0 \\ \dot{\gamma} &= 0 \quad \text{if } \tau \leq \tau_0 \end{aligned} \tag{4.1}$$

where $\tau$ is the shear stress of fresh concrete, $\tau_0$ the yield stress, $\mu$ the plastic viscosity, and $\dot{\gamma}$ the shear strain rate. Figure 4.10 shows the graphical representation of the Bingham model. The Bingham model treats the concrete mix as a homogeneous material, and it is the simplest model used to describe the concrete rheology.

However it is also seen that the yield stress of concrete goes on increasing as it is kept at rest. This happens because of structural build-up at mirco-scale and this time-dependence property is called thixotropy. The build-up can be broken down if a large enough shear force is applied on the concrete. Such type of thixotropy is termed as reversible. Yield stress also goes on increasing due to the advent of hydration and the original yield stress cannot be recovered. This is known as irreversible thixotropy. The use of retarders makes hydration irrelevant during the placement process and hence can be neglected when dealing with fresh concrete. A simple model which considers reversible thixotropic effects was proposed in [Rou06b]. In this model the Bingham model is adjusted slightly, and is given by the following set of equations:

$$\begin{aligned} \tau &= (1+\lambda)\tau_0 + \mu\dot{\gamma} \\ \frac{\partial\lambda}{\partial t} &= \frac{1}{T} - \alpha\lambda\dot{\gamma} \end{aligned} \tag{4.2}$$

where $\lambda$ is the flocculation parameter, $T$ is the characteristic time for flocculation and the term $1/(\alpha\dot{\gamma})$ is the characteristic time for deflocculation. Thus a minimum of two more parameters are required to consider reversible thixotropy. The Bingham fluid model can be used to describe the bulk flow of concrete where the flow pattern is required. However it has its drawbacks. The Bingham model treats the entire concrete as a single homogeneous fluid and hence fails to capture interaction between its various constituents. At the macro-scale this means blocking, segregation and bleeding cannot be modelled, thus disabling the use of the model to capture defects associated with these phenomena.

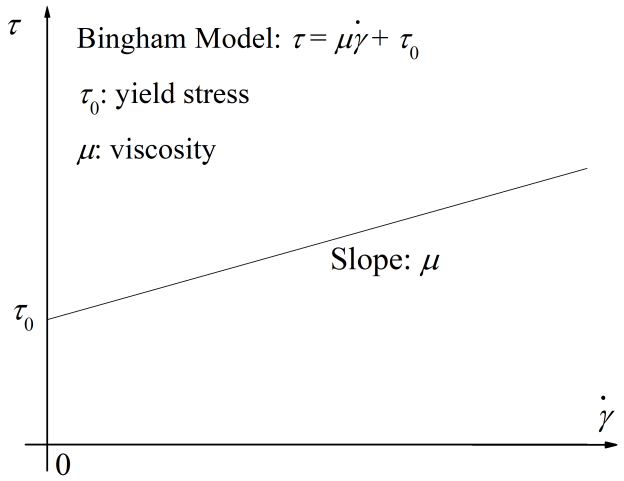

Figure 4.10: Graphical representation of Bingham model

## 4.3 Experiments

Research on fresh concrete has largely been based on experiments and tests. There exist numerous tests for determining the quality of fresh SCC which have been specified in standards and guides. Literature on fresh concrete research also reports the use of many non-standard experiments designed to study concrete flow behaviour. Apart from small scale tests and lab experiments, field tests have been performed in order to study the bulk flow of concrete at the industry scale.

### 4.3.1 Standard tests for fresh concrete

In this section, some of the most commonly used tests as suggested by design standards or practice guides are summarized. The list is not exhaustive and the readers are referred to the relevant industrial guides for more detailed information.

#### 4.3.1.1 Slump flow test

The slump flow test is a simple test to determine the workability of fresh concrete. In this test a standard Abrams cone is filled with wet concrete and then lifted. The final spread diameter and the T500 time (the time required for the spread diameter to reach 500mm) are the measured quantities. For more details can be found in BS-EN-12350-8. The slump flow diameter is considered to be an indicator of the yield stress of the fresh concrete. Figure 4.11 shows the set-up of the slump flow test.

#### 4.3.1.2 V-funnel test

The V-funnel test is used to measure the flowablity of fresh concrete. A funnel of 12 litres is filled with wet concrete and the time taken to empty the funnel is measured. For more details it is referred to BS-EN-12350-9. The flow time is thought to be most affected by the plastic viscosity of the fresh concrete. Figure 4.12 shows the apparatus used for the V-funnel test.

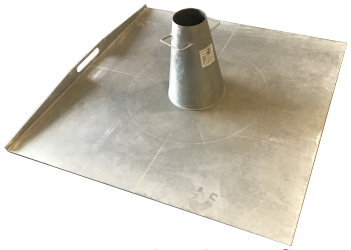

Figure 4.11: The slump flow test

Figure 4.12: The V-funnel test

#### 4.3.1.3 L-box test

The L-box test is used to assess the extent to which the fresh concrete is subject to blocking by reinforcement bars. The vertical section of an "L" shaped box is filled with concrete and then a gate is lifted to allow the concrete to flow into the horizontal section. Once the flow has stopped, the passing ability ratio, which is the ratio of height of concrete at the end of the horizontal section to the height of concrete remaining in the vertical section, is calculated. The horizontal section is marked at the 200mm and 400mm mark. Time required for concrete to reach these marks are measured respectively as T20 and T40 times. For more information it is referred to BS-EN-12350-10. The apparatus used for L-box test is shown in Figure 4.13.

#### 4.3.1.4 Column segregation test

This test is used to determine the static segregation resistance in fresh concrete. Wet concrete is filled in a cylinder and allowed to segregate for 15 minutes. The top and bottom section of the cylinder is then removed and sieved to find the amount of course aggregates by weight. Segregation ratio is calculated as the difference in weight of the top and bottom sections divided by the average weight. For more information it is referred to ASTM-C1610/C1610M-17. Figure 4.14 shows the cylindrical apparatus used to perform the column segregation test.

Figure 4.13: The L-box test

Figure 4.14: The segregation column

#### 4.3.1.5 Rheometers

Specialized rheometers have been used to measure rheological properties of fresh concrete. The most common rheological model used by these instruments is the Bingham model although some also use more advance models like Herschel-Bulkley.

Thixotropy can be measured using these set-ups. Examples of common rheometers used by researchers are the BML viscometer, BTRHEOM and ICAR rheometer. Figure 4.15 shows an ICAR rheometer.


Figure 4.15: The ICAR rheometer

The list of experiments mentioned above are not exhaustive. They are merely the most widely used ones for rheological characterization of fresh concrete. Some other standard tests include the J-ring, inverted-cone, mini-cone and flow-table tests, to name a few.

## 4.3.2 Non-standard tests

Tests and experiments summarized in this section are not documented in any standard or practice guide. They are found in literature and have been designed by researchers to facilitate the study of fresh concrete flow. Only a few have been mentioned here as examples.

### 4.3.2.1 LCPC box

The LCPC box is a test designed for yield stress measurement of fresh concrete [Rou07]. The test consists of a rectangular box in which 6 litres of wet concrete is poured from one end. The final spread length of the flow is measured. This measurement is used to identify the yield stress of the material using a pre-calibrated curve. Dimensions of the LCPC box are shown in Figure 4.16.

### 4.3.2.2 Slipping resistance test

An experimental set-up was used [MT90] to measure the slipping resistance between fresh concrete and steel board. This apparatus is also calibrated according to the Bingham model and is shown in Figure 4.17.

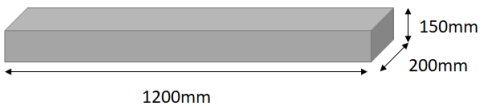


Figure 4.16: The LCPC box [Rou07]

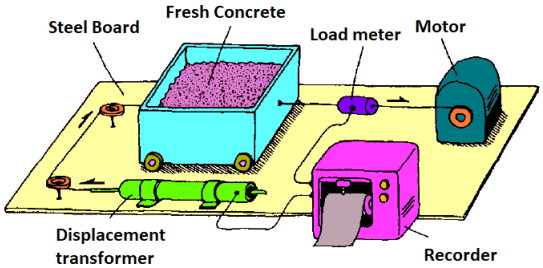


Figure 4.17: The slipping resistance tests [MT90]

#### 4.3.2.3 Normal and shear contact test

To study the interaction between aggregate particles in fresh concrete and to obtain force-displacement relationships (FDR) between them, an experiment set-up called the normal contact test (NCT) and shear contact test (SCT), was designed in [NGF+16]. The NCT test is shown in Figure 4.18.

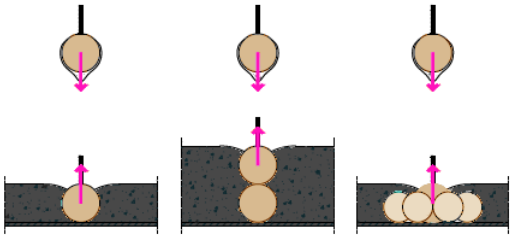

Figure 4.18: The normal contact test

The above experiments are a few of the experimental research examples to study the behaviour of fresh concrete. Others include modified J-ring, modified inverted cone and modified L-box tests, to name a few.

### 4.3.3 Field tests

The bulk flow of fresh concrete is studied at the industrial scale by performing field experiments. To understand the flow mechanisms of tremie concrete, field trials were conducted on bored piles by Bohle and Pulsfort [BPLH13]. Each batch of concrete was dyed with a different colour before being sent through the tremie pipe. Figure 4.19 shows the cut cross section of the pile. Also in a separate study to monitor concrete flow, temperature sensors were attached to the reinforcement cage during the filling process. Based on the temperature of old and new concrete, an estimate of the flow pattern could be achieved [SAR13].

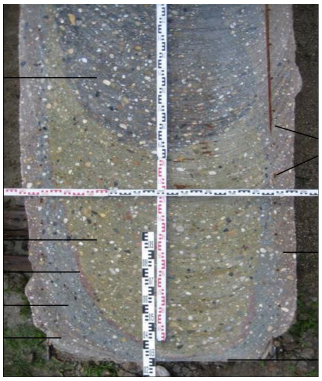

Figure 4.19: Dyed concrete from a bored pile field trial [BPLH13]

## 4.4 Numerical modelling

As an alternative to tests and experiments, numerical simulations can be used to better understand concrete rheology and to assist mix proportioning if it can

be correlated to rheology. More importantly, computer modelling can be used to simulate industrial scale problems. This will enable engineers to better specify the workability required and predict the formation of placement defects in structures before the actual construction process is carried out. Various numerical techniques have been used to model concrete flow in literature. These methods are well established modelling strategies in computational engineering and have been applied to simulate fresh concrete flows. They include the discrete element method (DEM), the smoothed-particle hydrodynamics (SPH), the lattice Boltzmann method (LBM), the finite element method (FEM) and the finite volume method (FVM). Literature on the use other methods like dissipative particle dynamics (DPD) [MF02] exist but are not widely used for the purpose of concrete flow simulations. These approaches are summarized in the following sections in the context of fresh concrete flow simulations and the relevant research is reviewed.

### 4.4.1 Discrete element method (DEM)

DEM is widely used in soil mechanics problems and simulating processes of loose materials or components which are considered particulate, granular or discrete in nature. Concrete too has granular properties and DEM could be used to simulate its flow. In DEM the material is divided into distinct rigid particles. Interaction of the particles is a dynamic process where the neighbourhood of an individual particle may vary over time. These interactions exist only between particles that are in contact and they are defined by constitutive relationships. Newton's law of motion is applied to each particle to determine its motion arising from forces acting on it. The force displacement relationships (FDR) are used to update the contact forces resulting from the motion. These forces are used again to compute the motion and thus the process repeats. Contact forces are generally resolved in normal and tangential directions. The FDR relates these forces to the relative displacement at the point of contact. Thus, in a DEM simulation of fresh concrete, the mechanical behaviour of concrete is fully controlled by the FDR. Appropriate FDR models need to be chosen to mimic concrete-like behaviour. The Bingham model is used as the constitutive relationship for fresh concrete in most literature and it has been implemented through the FDR. Figure 4.20 shows the contact model in the normal and tangential directions. It consists of spring, slider and dashpot elements the parameters of which determine the forces on particles. However, rheological behaviour is controlled by the element "contact" which can be user defined.

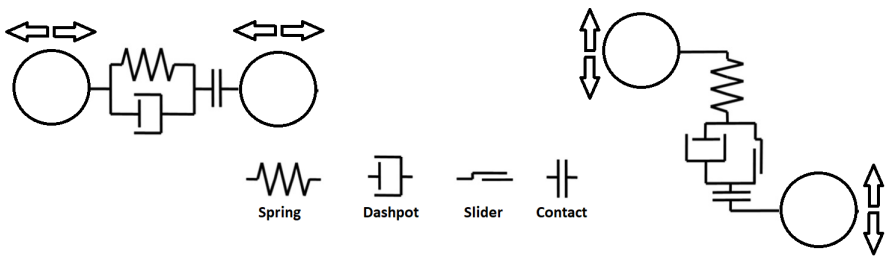


Figure 4.20: DEM contact model in normal and tangential directions [MS15]

An FDR for the contact element is shown in Figure 4.21. The "bond strength"

parameter is linked with the yield stress. In most literature, DEM is used to model fresh concrete using the "hard core, soft shell" approach. The hard core represents a rigid aggregate particle and the soft shell the mortar paste surrounding the aggregate. The soft shell does not exist as a material but is accounted for in the FDR, which is usually selected such that it mimics the Bingham model. Figure 4.22 shows a simulation of slump flow test using DEM.

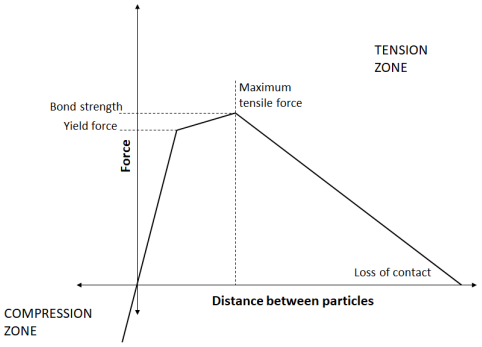


Figure 4.21: Force-displacement relationship of contact element [MS15]

Figure 4.22: Slump flow simulated with DEM [RP14]

An overview is provided in [MGK+14] on the DEM modelling of concrete flow. To estimate parameters for contact models and to establish relations between contact models and rheological properties of concrete are recognized as the major challenge in DEM. One of the earliest studies in DEM concrete simulations used a three dimensional approach to model the slump flow, V-funnel and L-box tests [NU99]. Particle packing was obtained naturally by simulating the pour of concrete into the mould and the equivalent density was used to maintain continuity. The reference [MS15] aimed at determining the bond strength parameter for a given yield stress. An equation for stress as a function of height in a standard slump cone was used to find the height at which stress is equal to the yield stress of the material. DEM was then used to model the slump cone without lifting the cone. The average compressive force between particles at the height found in the previous step gives the bond strength which corresponds to the materials yield stress. LCPC box test was simulated to verify the results against experiments using the obtained bond strength. [NGF+16] used experimental methods to determine the FDR between particles. A standard normal contact test and a shear contact test were used to obtain relationships for Carabol liquid, mortar and cement paste. The shear contact test was designed by modifying a rheometer with glass balls attached to its vanes. In [PU02] DEM was used to model shotcrete. A lifting ball viscometer was used

to determine the FDR for mortar, concrete and dry gravel. Formulae to relate DEM parameters with Bingham constants were implemented. The slump flow test was simulated. The calibrated FDR model was then used to simulate the shotcrete process, and it was observed that viscosity does not affect performance but increasing the yield stress increases the attaching of concrete to the wall. DEM simulations using the hard-core soft-shell approach was employed in [PU99]. Normal adhesion was retained while tangential adhesion was neglected. The effect of accelerating agent was considered by a factor that increases DEM parameters as a function of time. It was found that there exists an optimal pressure such that decent amount of compaction is achieved while rebound loss is kept to a minimum. A rheological simulation of Couette flow was carried out in [RP14]. A direct relationship between rheological characteristics of mortar and the simulated concrete was used in the force model. The FDR of particles was investigated experimentally in [SM13] with an objective of applying it to DEM concrete simulations. FDR for Bingham like fluids displayed the same shape however the characteristic points changed dependent on the rheological parameters. A simplified graphical representation of FDR for tensile and compressive loading was found to be good enough for DEM implementation if the elastic and viscous components of the contact force are considered separately. The reference [SM10] also aimed at establishing a link between bond strength and yield stress. DEM with elliptical particles instead of spheres was used to model the slump test in [YG11]. The contact thickness model was implemented. Aggregate blocking of mortar during extrusion was studied both experimentally and numerically in [ECRKA17]. DEM with hard-core soft-shell was used to compare a blocked system with an unblocked one. It was concluded that the ratio of opening and particle diameter have a greater effect in blocking than yield stress or plastic viscosity. A 2D DEM simulation of the slump flow test with elliptical aggregates was performed in [GYSF10]. DEM was used to simulate slump test in [HK12b] where volume fraction was calculated based on the area that is considered to be paste. DEM with polyhedral shape was implemented to simulate slump flow and L-box test in [CJLW17]. The aggregates shapes were matched by overlapping multiple spheres to form a clump. DEM with excess paste approach was used to simulate a flow test and slump test in 2D [HK14], [HK12a]. Rheology was linked with the mix proportion in the model. DEM was employed to simulate flow in a pump [CZT$^+$15]. Concrete particles and aggregates were separately modelled and a density difference exists between the two. Parameters were first verified by simulating a rheometer and were fine tuned. It was observed that the yield stress increases with the increase in volume fraction of coarse aggregates. Realistic shapes of aggregates were considered in [HSPC15] which may be implemented in DEM. Normal interaction between two glass beads in cement paste was experimentally observed in [HKvB11] with the aim of applying it as an FDR. In [HK12b] DEM was utilised to simulate the slump flow test and mixes from which very pasty to less pasty were compared. Concrete flow was simulated by DEM and the physical effect of flocculation and hydration were taken into account [LCT16]. Flocculation was considered by implementing the parallel bond model while formation of clumps was used to capture the effect of hydration. For verification, flow table and funnel flow tests were simulated and compared to experiments. Discrete element model was applied to compaction of

pervious concrete and a new model for contact in the normal direction was proposed [PCA16]. Compression test was performed both numerically and experimentally. The effect of volume fraction was considered in stage one while the effect of size and shape of aggregates was considered in stage two. DEM simulations of transport process in truck mixers were performed in [FLT+15]. Two phases were used to simulate aggregate and mortar distinct interactions were set up between them. ICAR rheometer was simulated to verify behaviour of concrete against experiments and the mixing process was analysed at the micro and macro scale. Two phases were used to simulate concrete flow in [ZLZ17] using DEM. Granular blocking model was verified and extended and a physical test which evaluates blocking was performed. A method similar to DEM called the suspension element method (SEM) used rigid particles connected by cylindrical elements [TMW90a]. These elements are viscoplastic in nature and disappear once the particles are far apart. L-box, vibration box and beam casting were simulated using this method. In [CLX19], DEM was used to model SCC and the pumping behaviour was simulated. A parametric study was carried out where the influence of pipe geometry, material property and pumping conditions was studied. In [LCG18], DEM was used to simulate SCC and time dependent behaviour (thixotropy) was modelled by considering cement hydration and flocculation. A viscometer was simulated. Polyhedral shaped DEM particles were used in [ZLZL18] to model aggregates of different shapes and the slump and L-box tests were simulated. Blocking in SCC was studied using DEM in [CYSW18] and irregular shaped particles were used.

### 4.4.2 Smoothed-particle hydrodynamics (SPH)

SPH is a particle-based method used for continuum scale simulations [LL10]. It was first used to solve astrophysical problems since movement of particles are similar to those of gases or liquids. Due to its simplicity and meshless nature it can be used to model concrete flow. In SPH, the fluid continuum is discretized into a finite number of particles which have mass and other material properties associated with them. Most literature on SPH-based concrete flow simulations have used the Bingham constitutive equation. This together with the Lagrangian form of momentum conservation equation form the governing equations:

$$\tau = \tau_0 + \mu\dot{\gamma} \tag{4.3}$$

$$\frac{1}{\rho}\frac{D\rho}{Dt} + \nabla \cdot \boldsymbol{v} = 0 \tag{4.4}$$

$$\frac{D\boldsymbol{v}}{Dt} = -\frac{1}{\rho}\nabla P + \boldsymbol{g} + \frac{1}{\rho}\nabla \cdot \boldsymbol{\tau} \tag{4.5}$$

where $\rho$ denotes the density of concrete, $\boldsymbol{v}$ the velocity, $P$ the pressure, $\boldsymbol{g}$ the gravity, and $\boldsymbol{\tau}$ the deviatoric stress tensor. In [KKG11] a projection method based on a predictor-corrector time stepping scheme was used to solve the governing equations. An intermediate particle velocity was obtained without enforcing incompressibility as follows:

$$\boldsymbol{v}^*_{n+1} = \boldsymbol{v}_n + (\boldsymbol{g} + \frac{1}{\rho}\nabla \cdot \boldsymbol{\tau})\Delta t \tag{4.6}$$

where $\Delta t$ denotes the simulation time step and the subscript the time stepping index. Correction step is performed by considering pressure term in Eqn. (4.5) and enforcing the incompressibility condition in Eqn. (4.4). Pressure can be obtained from the following equation:

$$\nabla^2 P_{n+1} = \frac{\rho}{\Delta t}\nabla \cdot \boldsymbol{v}^*_{n+1} \tag{4.7}$$

Particle velocity is updated from the computed pressure gradient. The particle position is updated using the velocity:

$$\boldsymbol{v}_{n+1} = \boldsymbol{v}^*_{n+1} - (\frac{1}{\rho}\nabla P_{n+1})\Delta t \tag{4.8}$$

Field variables and their gradients are interpolated from values at particles within the domain of influence. The governing equations are integrated over particles using the interpolation function. This is called the kernel estimate of the field variable. Specifically, a continuous quantity $A(\boldsymbol{x})$ at the point $\boldsymbol{x}$ can be estimated by interpolation among the surrounding SPH particles:

$$A(\boldsymbol{x}) = \sum_j \frac{m_j A_j}{\rho_j} W_{ij}(\boldsymbol{x}_i - \boldsymbol{x}_j, h) \tag{4.9}$$

where $A_j$ is the variable value at particle $j$, $m_j$ is the mass of particle $j$, $\rho_j$ is particle density, $W_{ij}$ is a symmetric kernel function, $h$ is the smoothing radius and $\boldsymbol{x}_j$ is the position of particle $j$; $j$ runs over the nearby particles. Most common kernel functions are cubic spline. Spatial derivatives at a particle can be approximated using:

$$\begin{aligned} \nabla A_i &= \rho_i \sum_j m_j \left( \frac{A_i}{\rho_i^2} + \frac{A_j}{\rho_j^2} \right) \nabla W_{ij}(\boldsymbol{x}_i - \boldsymbol{x}_j, h), \\ \nabla \cdot \boldsymbol{B}_i &= -\frac{1}{\rho_i} \sum_j m_j (\boldsymbol{B}_i + \boldsymbol{B}_j) \cdot \nabla W_{ij}(\boldsymbol{x}_i - \boldsymbol{x}_j, h). \end{aligned} \tag{4.10}$$

where $\boldsymbol{B}(\boldsymbol{x})$ denotes a vector-valued variable. Figure 4.23 shows a simulation of V-funnel test using SPH.

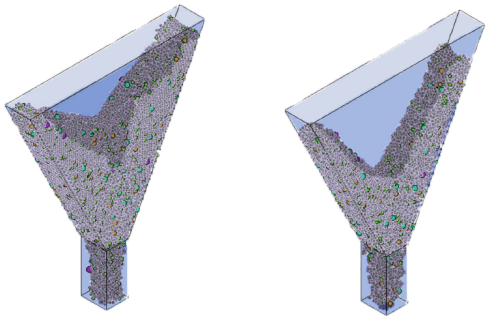

Figure 4.23: V-funnel simulation using SPH [AKK17]

SPH was used to model homogeneous concrete in 2D asymmetrically [KKG11], where dummy particles were used for wall boundary conditions and the slump flow and L-box tests were simulated. The V-funnel test was simulated using 3D SPH in [AKK17]. Discharge time was compared with experiments. Aggregates were modelled by introducing particles that are larger and denser than homogeneous concrete but with the same rheological properties of concrete. Aggregate distribution was observed for segregation but was found to be minimal. The V-funnel test was modelled using SPH in 2D and an appropriate range for viscosity and yield stress for SCC was determined by repeating simulations with various combinations of the two parameters [LHC14]. Based on guidelines for discharge time, proper ranges of viscosity and yield stress were suggested. The L-box test was simulated by implementing SPH in 2D [LCHP13]. Appropriate range of plastic viscosity for SCC was decided based on the passing ratio by performing numerous simulations with a wide range of plastic viscosity and yield stress values. 2D SPH was used to simulate slump flow and L-box in [WLXD16] but mirror particles were used instead of wall particles. 3D SPH was applied to L-box test and larger denser aggregate particles with the same rheological properties of concrete were added [ARKK17]. Experiments with coloured aggregate were used to compare the simulation results. The slump test was simulated with SPH in [DKK14a]. Viscosity was predicted based on concentration of constituents and the value was modified considering the influence of fibre volume fraction. Fibres were represented by two particles at the end of fibre with a set distance between the particles. They were passive markers which move together with the fluid flow. A similar strategy of modelling fibres was used in [DKK14c] to simulate the L-box test [DKK14b]. The concept of fibre orientation factor was introduced in [DKK14b] and was defined as the ratio between the projected length along the normal to the cut plane and the actual length of fibre. The slump flow test was modelled using SPH in [BKK16a] with the aim of determining whether T500 or Tstop time can be used to measure yield stress knowing the viscosity which is determined from a micro-mechanical process. Also the distribution of aggregates was measured by tracking aggregate particles. SPH was used to simulate the L-box test in [CL17], but instead of the Bingham model a new rheological model called the viscous granular material model was used. Deformation was time dependent while deformation resistance was pressure dependent on account of friction between the particles. J-ring test was modelled with SPH in [DKK16]. The slump flow test was modelled with SPH in [BKK16b]. The cone lift rate was changed and the effect of that on the T500 time was observed. It is found that the T500 value decreases as the cone lift rate was increased. The reduction was not monotonic but exhibited a bilinear response. SPH was used in [TLZ19] to model SCC with flexible fibres and the slump flow test was used as validation. The cross rheology model was used. In [GDM19], Folgar-Tucker fibre orientation model was coupled with SPH and used to simulate casting fibre reinforced concrete. SPH was used to simulate SCC and the boundary restraint model was used to treat openings boundary restraint to the flow [CLX19].

### 4.4.3 Lattice Boltzmann Method (LBM)

LBM has its roots in the kinetic theory of gases and treats fluid as particle distributions. LBM, unlike the other methods to simulate fluid dynamics, is based on Boltzmann equations which is related to the theory of ideal gases. The problem is defined in terms of particles distribution functions which can be interpreted as clouds of microscopic particles. Discrete particle distribution functions are used to discretise the particle distribution. LBM supplies rules for collisions and propagation of the particle distributions and computation of macroscopic quantities. In LBM, space is discretized by a set of Eulerian cells of uniform size. Time steps are used to march through time. Space, time and reference density are set to unity and the real problem is then scaled. Each cell has a lattice node at the centre. Lattice nodes hold $N$ discrete particle distributions for various lattice velocities. Rate of deformation of particle distribution is introduced by a relaxation time which is derived from apparent macroscopic viscosity (constitutive model). The LBM equation is as follows:

$$f_\alpha(\boldsymbol{x} + \boldsymbol{c}_\alpha \Delta t, t + \Delta t) = f_\alpha(\boldsymbol{x}, t) + \Omega_\alpha(\boldsymbol{x}, t) \tag{4.11}$$

where $f_\alpha(\boldsymbol{x}, t)$ represents the probability of finding a particle at position $\boldsymbol{x}$ and time $t$ with velocity $\boldsymbol{v} = \boldsymbol{c}_\alpha$, $\boldsymbol{c}_\alpha$ is a microscopic lattice velocity of the particle distribution and $\Omega_\alpha(x, t)$ is the collision operator. Local density can be computed as a sum of particle distributions in one node:

$$\rho(\boldsymbol{x}, t) = \sum_{\alpha=1}^{N} f_\alpha(\boldsymbol{x}, t) \tag{4.12}$$

Local velocity is calculated as the sum of particle distributions in one node multiplied by their respective lattice velocities

$$\boldsymbol{u}_f(\boldsymbol{x}, t) = \frac{1}{\rho(\boldsymbol{x}, t)} \sum_{\alpha=1}^{N} f_\alpha(\boldsymbol{x}, t) \boldsymbol{c}_\alpha \tag{4.13}$$

Thus LBM has a relatively simple implementation logic. The code can also be parallelized since the LBM core requires local information only. Figure 4.24 shows a simulation of slump flow using LBM.

LBM was used to simulate homogeneous concrete in [SSS+11]. The immersed boundary method was used to form a force field to model particles of any shape. A mass tracking algorithm was used to track the free surface. It was then applied to simulate the slump flow test. A modified LBM was employed to simulate Herschel-Bulkley fluids by splitting the constitutive equation [WHY+17]. Poiseiuille flow was used for testing and was applied to 3D printer extrusion. The LBM was used to simulate the flow in a modified rheometer [FGMM07]. The numerical results showed that small changes in rheometer design can have a significant impact on how the rhelogical data should be extracted from experimental results. A multiple-relaxation time lattice Boltzmann method (MRT-LBM) with D3Q27 discrete velocity model was applied to concrete flow in [QH18]. Herschel-Bulkley model was used and mass tracking algorithm was used for gas-liquid interface, and

the L-box, slump flow and modified L-box tests were simulated.

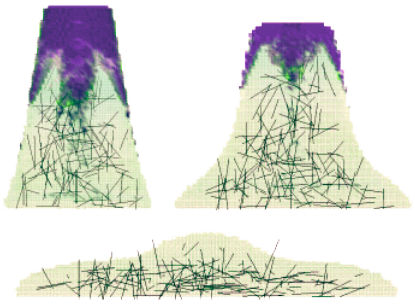

Figure 4.24: Slump flow simulated with LBM [SSS+11]

### 4.4.4 Finite element method (FEM)

FEM uses patch-wise polynomial approximations of unknown variables to convert partial differential equations, the governing equations of the problem, into algebraic equations. It is widely used to solve problems in areas of structural analysis, heat transfer, fluid flow, and electromagnetic potential etc. A finite element strategy consists of a variational formulation, discretisation strategy, solution algorithms and post-processing. Discretisation of space is done by meshing the domain, i.e. dividing the domain into various elements. Shape functions are defined and reference elements are mapped onto elements in the mesh. The original boundary value problem is written in the weak form, i.e. the form which does not require to hold absolutely and has weak solutions with respect to test functions. This form is discretised in space and appropriate shape functions are chosen. The problem is then written in the matrix form and solved. Concrete can be considered as a solid which undergoes large deformations or as a fluid which flows when a large enough shear stress is applied on it. Thus a Lagrangian or Eulerian approach could be used to model its behaviour. In literature both of these approaches have been used when using a finite element strategy. Incompressible Navier-Stokes equations can be solved in an Eulerian framework using FEM and appropriate constitutive models can be implemented to simulate concrete behaviour. The continuity and momentum equations in this framework are given as follows:

$$\nabla \cdot \boldsymbol{u} = 0 \tag{4.14}$$

$$\rho(\frac{\partial \boldsymbol{u}}{\partial t} + (\boldsymbol{u} \cdot \nabla)\boldsymbol{u}) - \nabla \cdot (\boldsymbol{\tau} - P\boldsymbol{I}) = \rho \boldsymbol{f} \tag{4.15}$$

where $\boldsymbol{u}$ is velocity, $\rho$ is density, $\boldsymbol{\tau}$ is the deviatoric tensor, $P$ is the pressure, $\boldsymbol{I}$ is the unity tensor, and $\boldsymbol{f}$ is the body force. Two shape functions, $\Psi_i(\boldsymbol{x})$ and $\Phi_i(\boldsymbol{x})$ are introduced to interpolate pressure and velocity respectively. Approximation for $P$ and $\boldsymbol{u}$ are given as:

$$P_h = \sum_{j=1}^{m} P_j \Psi_j(\boldsymbol{x}) \tag{4.16}$$

$$\boldsymbol{u}_h = \sum_{j=1}^{3n} \boldsymbol{u}_j \Phi_j(\boldsymbol{x}) \tag{4.17}$$

These approximations are then substituted into the governing equations (4.14-4.15), which can be transformed into the matrix form through a variational formulation (or the equivalent Galerkin method):

$$\boldsymbol{SU} + \boldsymbol{N}(\boldsymbol{U}) - \boldsymbol{L}^T\boldsymbol{P} = \boldsymbol{F} \tag{4.18}$$

$$\boldsymbol{LU} = \boldsymbol{0} \tag{4.19}$$

where $\boldsymbol{U}$ is the vector of unknown velocities, $\boldsymbol{P}$ is the vector of unknown pressure. $\boldsymbol{SU}$ is the discretisation of the viscous term, $\boldsymbol{N}(\boldsymbol{U})$ is discretisation of the convective terms, $\boldsymbol{LU}$ is discretisation of the divergence of $\boldsymbol{U}$ and $-\boldsymbol{L}^T\boldsymbol{P}$ is the discretisation of gradient of pressure. $\boldsymbol{F}$ is the source term and the contribution of the boundary conditions. An iterative solution procedure is usually needed to solve the algebraic equations (4.18-4.19). The constitutive model is applied through the term $\boldsymbol{\tau} - P\boldsymbol{I}$ and in the case of concrete flow simulations, the Bingham model is usually applied. Figure 4.26 shows a simulation of slump flow test using a Lagrangian formulation. Figure 4.25 shows the simulation of a Marsh cone test on cement paste using an Eulerian approach.

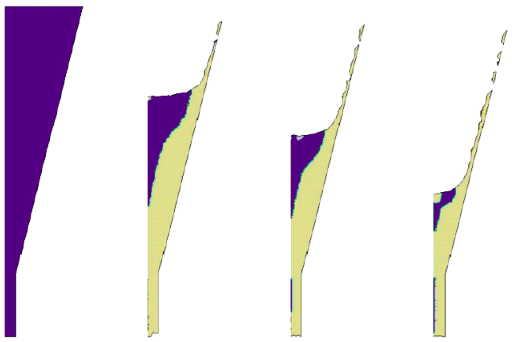

Figure 4.25: FEM simulation of Marsh cone using an Eulerian approach [FCT+12]

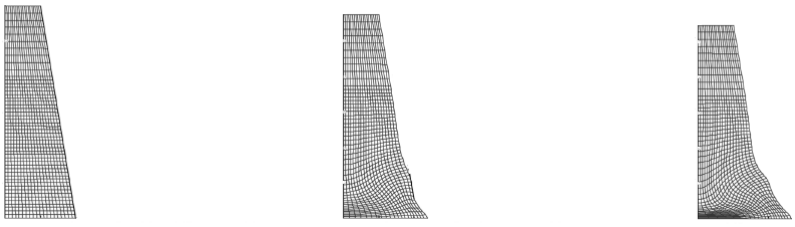

Figure 4.26: FEM simulation of slump flow using a Lagrangian approach [CH05]

Eulerian FEM with Lagrangian integration points (FEMLIP) was used in [DPC05] to model free surfaces. LIPs are Gaussian points, and can move within an element and carry material properties with them. Slump and L-box tests were simulated and compared to experiments on ordinary concrete, high performance

concrete and SCC. A fully Lagrangian approach with FEM was used to model homogeneous concrete with the free surface tracked by remeshing [CFFP10]. Continuous retriangulation was done by using particles that are added or removed based on how close they are. The L-box, marsh cone and slump flow tests were simulated and compared to analytical and experimental results. A 3D FEM approach was used in [TSG$^+$04]. Volume of fluid method (VOF) was used to track free surfaces and the L-box test was simulated. A computational homogenisation approach was used to model non-Newtonian flow through perforated domain (rebar area) in [KPZ18]. Stokes-Darcy system was obtained by homogenisation of Stokes flow at porous sub-domain level. FEM discretisation in the Eulerain framework was used and fully resolved results were compared to homogenised results. Two extra parameters were required: friction between the interface of porous region and the obstacle radius. A similar porous medium approach was used in [KPZ16]. A numerical algorithm was proposed in [KPT15] to predict fibre orientation in SCC. Orientation was described by probability distribution function with which the knowledge of velocity field was required. A Lagrangian viscoplastic finite element was used to model the slump test and vibration test in [MT90], [TMW90b]. Slip elements with spring and damper elements were used in the area of contact with the surface. A node in contact with the surface was fixed using such an element. An apparatus was designed to obtain the "slipping yield stress" and the "slipping viscosity". The viscoplastic finite element strategy is used in [TM89] to model the slump flow test. An FEM based CFD solver with VOF (volume of fluid) surface tracking algorithm was used to model L-box and slump flow in [PB09]. Slump flow test simulations with Lagrangian FEM were performed and the effect of yield stress on slump was analysed in [CH05]. Rheology of cement paste was investigated using a Lagrangian FEM based CFD solver. Rheological parameters were obtained from rheometers and the mini cone and flow cone test were simulated. FEM in the Eulerian framework was employed to model fresh concrete flow in [LSCT07]. A level-set method was used to simulate the free surface. The fibre orientation was modelled as an orientation evolution equation and the slump cone test was simulated. Eulerian FEM with level-set method was utilised to simulate concrete flow and the benchmark tests of lid driven cavity and standing wave were simulated in [Svá08]. The mini-conical test was simulated in [BGB10] using FEM where interface tracking was considered using an scalar transport equation. FEM was used to simulate SCC in [KPZ18]. Reinforced domain was modelled as a porous medium. Homogenisation techniques were combined by the Darcy Law with an inter-facial coupling with Stokes and Darcy flows.

### 4.4.5 Finite volume method (FVM)

Like FEM, FVM converts partial differential equations into algebraic equations for numerical solutions. FVM is used to solve problems in fluid dynamics, thermal analysis, solid mechanics etc. The space domain is divided into cells and the term "finite volume" refers to the small cell volume surrounding a point on the mesh. Volume integrals of the governing partial differential equations are converted into surface integrals using the divergence theorem. The terms are then treated as

fluxes at surfaces of cells. A flux leaving one volume enters into adjacent volumes making the formulation conservative. FVM is widely used to solve the Navier-Stokes equations in the Eulerian framework. Using a proper constitutive relationship makes the strategy suitable for simulating concrete flow. The Navier-Stokes equations can be written in the following form:

$$\frac{\partial \rho}{\partial t} + \nabla \cdot (\rho \boldsymbol{u}) = 0 \tag{4.20}$$

$$\frac{\partial}{\partial t}(\rho \boldsymbol{u}) + \nabla \cdot \rho \boldsymbol{u}\boldsymbol{u} = -\nabla P + \nabla \cdot \boldsymbol{\tau} + \boldsymbol{f}_b \tag{4.21}$$

where $\rho$ is the density of the fluid, $\boldsymbol{u}$ is the velocity of the fluid, $P$ is the pressure, $\tau$ is the stress tensor of fluid and $\boldsymbol{f}_b$ is the body force. By application of the divergence theorem, using backward Euler time discretisation in time and explicit evaluation of certain terms, the discretised version of these equations can be written as:

$$\sum_{f=1}^{n} \rho \boldsymbol{u}_f \cdot \boldsymbol{A}_f = 0 \tag{4.22}$$

$$\frac{\rho \boldsymbol{u}_c^{t+\delta t} V_c}{\delta t} - \frac{\rho \boldsymbol{u}_c^{t} V_c}{\delta t} + \sum_{f=1}^{n} \dot{m}_f \boldsymbol{u}_f = -(\nabla P)_c V_c + \sum_{f=1}^{n} \boldsymbol{\tau}_f \cdot \boldsymbol{S}_f + \boldsymbol{f}_b V_c \tag{4.23}$$

where $f$ and $c$ subscripts denote the value at the face and cell centre respectively and the superscripts denote the time step. $V_c$ is the volume of the cell, $\dot{m}_f$ is the mass flux at the face centre, $\boldsymbol{S}_f$ is the surface vector of the face and $\boldsymbol{A}_f$ is the area vector of the face. These equations can be converted into algebraic equations of the form:

$$a_c \boldsymbol{\Phi}_c + \sum_{F=1}^{n} a_F \boldsymbol{\Phi}_F = \boldsymbol{b}_c \tag{4.24}$$

where $\boldsymbol{\Phi}_c$ is the cell centred value of the variable to be determined and $\boldsymbol{\Phi}_F$ is the value of the same for neighbouring cells. $a_c^v$, $a_F^v$ and $\boldsymbol{b}_c$ represent the coefficients obtained during the reduction into this form. Figure 4.27 shows a simulation of slump flow using FVM.

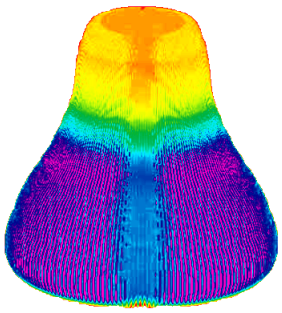

Figure 4.27: Slump flow simulation using FVM [Rou06a]

Rebars in FVM simulations of concrete were replaced by porous medium which

offers resistance to the flow [VMKR11]. This was done to replace fully resolved rebar geometry, thus reducing the number of elements used. An extra source term was added to the momentum equation containing permeability, shift factor and local apparent viscosity all of which had to be determined. This methodology was tested in [VRMK10] and [VSK+16]. A tank was divided into zones with different density of rebars and concrete was poured from one end. The final distribution of the surface obtained through simulations was compared to the surface obtained by experiments. A model for thixotropy was proposed in [Rou06b]. It was then implemented using FVM to simulate multi-layer casting phenomena. FVM was used to simulate Marsh cone for cement paste and slump cone for concrete in [Rou06a]. Slump versus dimensionless yield stress were plotted for both tests using numerical simulation to find a correlation between them. In [RC05] an analytical solution for slump in two asymptotic flow regimes for any cone geometry was derived. Numerical simulations were performed for the slump flow using an FVM solver and graphs of slump versus yield were drawn for both analytical and numerical solutions. SCC flow in walls and columns during the filling process was modelled in [TVDMV+10], [TVDMV+14] using FVM. Pressure was measured at various heights and these measurements were compared to those obtained through actual experiments. The same simulations performed by including presence of rebars in [TDST+15]. The discontinuity in Bingham model was tackled in [ZAW15] by proposing a new algorithm. The cement paste was first computed as a Newtonian fluid and then a pressure threshold judgement was used to modify motion state of cement paste cells. Lastly an iterative correction process was used to determine the unyielded and yielded region. FVM with tangent of hyperbola method was used for surface tracking and the slump flow was simulated. A 1D partial differential equation which describes the relation between velocity, time and distance was solved using finite differences in [ABL12] and an analytical solution for the same was derived. The two solutions were compared. FVM was employed to simulate flow of high performance concrete in a slipform machine [dLR11]. L-box test was simulated with FVM and the values of plastic viscosity and yield stress were changed to see their effect on the simulations [HKY17b], [HKY17a]. General moving object (GMO) was used to simulate the suspended bodies. Pipe flow of pumped concrete was simulated using FVM in [CKK13], [CKK14] and the effect of volume fraction on the yield stress and viscosity was considered by equations obtained from literature. The shape of aggregates was also considered. Effect of particles on the boundary layer were observed. FVM with VOF was utilised in [SKH17] to simulate slump flow and L-box test. A new test called "flow test" was devised to correlate yield stress with final flow length and flow time with plastic viscosity [GSL14]. FVM was used to simulate flow in the flow test. FVM was used to model flow of homogeneous concrete in a box [BBX+17]. Steel fibres were modelled as two spheres connected to each other on which drag laws apply. An analytical theory called the 'dam break' theory was evaluated using FVM in an L-box and effect of static segregation on flow profiles was evaluated [HYK19]. The Herschel-Bulkley equation was used as the constitutive model. A CFD discrete phase model was used to simulate SCC [KÇY+18]. Blockage risk and segregation was studied.

## 4.5 Critical discussions on numerical modelling of fresh concrete flow

In the previous section, literature on numerical modelling of fresh concrete flow is summarized. In this section information from the previous research works will be critically analysed. The first subsection categories research works from various perspectives, while critical opinions are addressed in the second subsection.

### 4.5.1 Classification

Various numerical strategies have been employed to simulate fresh flow, including DEM, SPH, LBM, FEM and FVM. The literature can be classified according to the simulation strategy. Figure 4.28 shows the percentage of paper publications for each method, where DEM is the most popular approach followed by FVM, FEM, SPH and LBM.

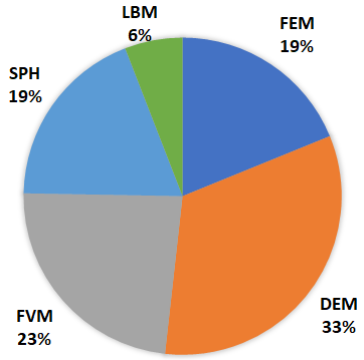


Figure 4.28: Distribution of numerical strategies based on paper publications

SPH, FEM and FVM all use the governing equations established from continuum mechanics as their starting point and they are all discretisation methods to solve the same governing equations. Hence these approaches can be classified as continuum based methods. DEM and LBM are not strictly used to solve problems in continuum mechanics and involve dividing the continuum into distinct particles. These are therefore non-continuum based approaches. The papers can be classified according to whether they use a continuum or non-continuum based approach. Figure 4.29 shows a pie chart based on this classification, where 61% of the papers use continuum based methods and 39% use non-continuum based approaches.

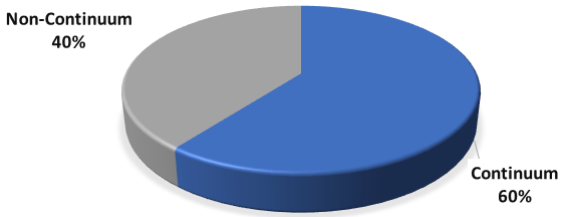


Figure 4.29: Continuum versus non-continuum approaches

Various scenarios of concrete flow have been investigated in the literature. Standard lab tests are widely simulated and instances of full-scale simulations are also seen. The number of papers which simulate these are shown in Figure 4.30. The L-box and slump are the most simulated lab tests while V-funnel and J-ring tests have also been simulated. Apart from these, other standard lab tests like marsh-cone and non-standard lab tests like the LCPC box have been classified under miscellaneous. There have also been attempts to simulate filling of form work and are grouped under "full-scale".

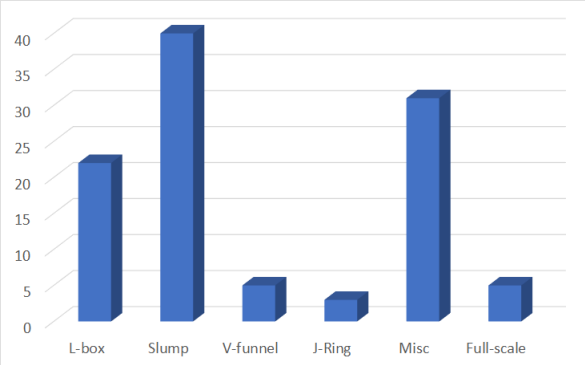

Figure 4.30: Papers based on object of simulation

### 4.5.2 Discussions

As mentioned previously, understanding fresh concrete rheology can enable engineers to fully utilise the advantages of self compacting concrete and other highly flowable concretes by determining accurate specifications required for particular applications. Simple lab tests and experiments are conventionally used for this purpose. Some of these tests and experiments are briefly recapped in Section 4.3. Tests like slump, L-box, V-funnel and rheometers all deal with analysing the "bulk" properties of concrete implying that the tests attempt to evaluate the property of fresh concrete based on the Bingham fluid model. Most of these tests are easy to perform and provide quick readings making them extremely popular for use on site to accept or reject mix batches. However, it is clear that a sophisticated understanding of concrete rheology would involve more than just relative measures of the properties. Measurements associated with these tests are unable to quantify rheological properties. Although rheometers attempt to determine values of yield stress and plastic viscosity, it is seen that the values obtained from different rheometers vary greatly for the same mix. Thus, even rheometers, at best, can only be used to classify concrete mixes. Standard concrete tests are performed at a fraction of the scale of full-scale applications. Thus flow behaviour of concrete at the industrial-scale cannot be directly predicted using these tests. Many large-scale experiments to determine concrete flow behaviour have been performed, examples of which are provided in Section 4.3. It is however a difficult task to measure flow properties at this scale due to unavailability of technology or difficulty in designing a practical set-up to do so. For example thermal methods or the use of dyes have been used to monitor concrete flow during the piling process, however data obtained from such experiments is not continuous in time or space. Scale of the experiments

are often compromised such that obtaining data is practical. Also the costs incurred to perform large-scale experiments is high. The only alternative to analyse and predict concrete rheology and flow behaviour is the use of numerical methods. Simulations can provide a much better understanding due to exact quantification of flow properties and availability of continuous data in space and time. They are also much cheaper to perform and can serve as a vital tool for engineers to predict placement defects and recommend better mix specifications.

The Bingham model is introduced in Section 4.2. The model describes flow by the use of two parameters namely yield stress and plastic viscosity. The model has been widely used to describe fresh concrete flow and nearly all research works in numerical modelling, introduced in Section 4.4, assume this model or its variants. The Bingham model successfully captures the yield property of concrete i.e. the resistance to flow below a certain critical value of stress and the resistance to flow once the critical value is surpassed. Standard labs tests like slump, L-box and V-funnel can be simulated to great accuracy using the Bingham model. The flow of concrete at the full-scale can also be modelled and many questions regarding pattern of placement can be answered. However, the Bingham model assumes that the concrete is homogeneous in nature. In Section 4.2 we have seen that concrete in the fresh state is a rather complex material involving interactions at multiple scales between its constituents. Many of the defects and rheological properties of fresh concrete behaviour arise due to these interactions and are not captured by the Bingham model, due to the homogeneous material assumption. Capturing the interaction between mortar and coarse aggregates enables modelling phenomena like segregation and granular blocking. Similarly capturing the interaction between fine aggregates, cement and water would enable us to model bleeding. The Bingham model is unable to answer major questions surrounding segregation, blocking, bleeding and defects associated with them. The Bingham model has been adopted as the constitutive model of choice and the flow problem has been solved using various methods as seen in Section 4.4. SPH, FEM and FVM are numerical strategies to solve continuum problems. Thus the basis for these methods are the Navier-Stokes equations. The Bingham model can be easily implemented as the constitutive model with a continuum based method. If the methods are implemented correctly SPH, FEM and FVM should give the same results as they are all based on the same governing equations. As seen in Figure 4.10 there is a sharp change in stress versus strain graph once the yield stress is crossed. This is a discontinuity which is slightly challenging to implement with continuum based approaches. The issue is tackled by either regularisation methods or the use of Lagrangian multipliers. The regularisation approach assumes that concrete never really stops flowing although the flow rate is small enough for it to be considered negligible. Lagrangian multipliers have been developed in [Wac07] and [WHY$^+$17] to ensure that no flow below the yield stress occurs. However, Lagrangian multipliers introduce increased complexity in the problem. Regularisation approaches are simple and there seems to be no need for the flow to completely stop in the application of fresh concrete flow.

DEM is a non-continuum based method and its formulation is not based on the Navier-Stokes equations. Until recently DEM has been the most used numerical method to model fresh concrete flow. Its advantages lie in the natural capture of

free surface and the ease of implementation. Simulating shotcrete using continuum based approaches is a challenge due to the high velocities involved and the lack of clear flow domain. Using DEM to simulate shotcrete is advantageous as high velocities are easy to handle and there is no requirement of a flow domain. Flow like behaviour and the constitutive model can be implemented through the FDR model by assigning appropriate parameters. Thus Bingham behaviour can only be indirectly mimicked in a non-continuum based approach and is non-physical. DEM involves discretising concrete into a finite number of distinct particles. The use of non-continuum based approaches to model concrete does not appear to conform with the nature of fresh concrete which like any other fluid is a continuum with a continuous distribution of flow variables like velocity and pressure. Fresh concrete is also incompressible in nature and this condition is satisfied explicitly due to the mass conservation equation in the case of continuum based approaches. In DEM however, incompressibility does not appear to be a condition which is rigorously implemented. Last but not least, it is hard, if not impossible, to achieve convergence with DEM simulations, and the result of DEM simulation can vary greatly when the particle number changes. Hence, DEM can be a useful tool for conceptual studies, but without a rigorous convergence verification it is questionable for use in quantitative investigations.

In Section 4.4 Lagrangian formulation based FEM techniques have been used to model concrete flow [CFFP10], [CH05], [MT90], [TM89]. The Lagrangian approach allows for easy free surface modelling. These methods are able to simulate small deformation without remeshing but require remeshing once the mesh gets distorted. The process of remeshing is computationally expensive and outweighs the gains of using such an approach. Although remeshing may not be required in Eulerian based approaches, modelling the free surface poses a challenge. Research on modelling free surfaces in fresh concrete flow has been carried out in [DPC05] and [CFFP10]. Although volume of fluid (VOF) is not the most accurate method to capture free surfaces it is still the most popular because it is computationally less expensive and relatively simple to implement.

As discussed earlier, the Bingham fluid model is incapable of simulating phenomena such as segregation, blocking and bleeding. Defects related to these are of prime concern in the industry and capturing them should be the main focus of research on numerical simulations of fresh concrete flow. The Bingham model has been used to simulate the L-box test in a number of papers. The purpose of L-box test is to measure the blocking resistance of the concrete. Using Bingham model, which assumes homogeneous concrete, guarantees that no blocking will occur during simulation, defeating the purpose of the test. This has been acknowledged in many papers which try to explicitly model aggregates or consider its effect as a volume fraction [BKK16a], [AKK17], [SSL09], [SRH$^+$12], [ARKK17], [ECRKA17], [HKY17b]. However the interaction between the constituents have not yet been completely resolved. The shape of aggregates also affects the interaction between them and the mortar and should be considered as a factor. Attempts to get realistic aggregate shapes have been made using DEM in [YG11], [GYSF10], [CJLW17], [HSPC15] but a model to describe its effect on interaction between mortar and aggregate requires more research. Homogenisation techniques are used

to capture the effect of obstruction of concrete flow due to the rebar cage where a porous medium is used to replace the rebar area [VSK+16], [KPZ18], [VRMK10], [VMKR11]. This technique helps keep computational costs low compared to a fully resolved rebar cage area and is useful when the flow near the rebar is not of concern. However, many important questions regarding fresh concrete flow are related to the behaviour of concrete around the rebar region and in such situations porous medium replacement would lead to loss of information in the region. There have been attempts to model the movement and orientations of fibres in the flow of concrete reinforced with fibres [KPT15], [DKK14c], [DKK14b], [LSCT07]. Sizes of the fibres are of the same order as that of aggregates or even smaller. Their movement and orientation would depend on the presence of aggregate particles. Fibre orientation in research has been modelled with the assumption of homogeneous concrete not considering presence of aggregates making the approach questionable. In summary the assumption of homogeneous concrete which is implied by the Bingham fluid model posses serious restrictions on the phenomena captured. Research should thus be focused on models which replace the Bingham fluid model allowing interactions between the constituents of concrete to be modelled.

## 4.6 Conclusions

Concrete is a material which has been improved upon for centuries. The need for a highly flowable variant of concrete led to the introduction of self-compacting concrete in 1988. To take complete advantage of highly flowable concretes and due to the increasing complexity of structures there is now an urgent need to understand fresh concrete rheology and model its flow behaviour. Complex interactions between the constituents of concrete and multi-scale nature of the phenomena involved make modelling fresh concrete a difficult task. Bingham model is the simplest model available to describe the "bulk" flow of wet concrete but considers the material to be homogeneous in nature neglecting interactions amongst its components. There exist standard lab tests which, at best, serve as a relative measure of the yield stress and plastic viscosity parameters. Large-scale experiments are limited by technology available to monitor the concrete flow. Numerical simulations offer an alternative to study fresh concrete rheology and can be used as a tool by engineers to predict defects and prescribe better mix designs. DEM, SPH, LBM, FEM and FVM are numerical techniques used in literature to simulate fresh concrete flow. Most research works on numerical modelling of fresh concrete flow assume the Bingham fluid model. Thus defects such as blocking, segregation and bleeding cannot be modelled. There is therefore a need to develop a new model which considers the effect of various interactions amongst the constituents of concrete in order to answer questions of immediate concern regarding concrete placement in the industry.

In the next chapter the homogeneous Binhgam model is applied to simulate the flow of fresh concrete. The quantification of the yield stress and plastic viscosity for a given concrete mix still remains a challenge and a new method to determine them is proposed. The same model is then used to simulate a practical industrial-scale problem. In the process the homogeneous Bingham model is pushed to its limit and is used to answer a few of the questions surrounding fresh concrete flow which the

industry demands. As a result the limitations of this approach are also highlighted which further bolsters the need for a more sophisticated approach towards modelling fresh concrete flow.

# Chapter 5

# Simulating concrete flow using the homogeneous Bingham model

In this chapter, techniques to model multiphase flows, are applied to simulate concrete flow. The Bingham model is used as the constitutive model and the concrete is assumed to be homogeneous. The objective is to gain a better understanding of concrete rheology and attempt to provide an insight into common problems which the industry faces during the concrete placement process. A detailed review on these issues, the experiments used to describe concrete behaviour and techniques used to numerically model its flow were provided in the previous chapter. From the review it is clear that a consensus has been met on the use of Bingham model to adequately describe flow of fresh concrete. It remains a challenge to determine the values of yield stress and plastic viscosity. The first part of the chapter provides an overview of a method to determine the parameters by simply measuring the flow diameter and flow time from the slump flow and V-funnel tests respectively. Both the tests are numerically modelled and a parametric study is performed. The resultant calibration curves are used to numerically determine the values of Bingham parameters.

The second part of the chapter looks particularly at the case of placement of tremie concrete in deep foundation piles. The industry currently is unclear on the exact mode and pattern of the flow of concrete during the placement process. A case study is performed by simulating the placement in a full-scale pile, varying the parameters and time of pour. The case study provides evidence that flow of concrete through the tremie pipe to its final position follows a peculiar pattern which must be considered while designing mixes and techniques of placement. It also reveals the limitations of the Bingham model in modelling the effects of segregation and blocking which cause most defects witnessed in the placement process.

## 5.1 Determination of rheological parameters for concrete mixes

Self compacting concrete (SCC) was first introduced by Japanese researchers in the 1980s. The main objective was to design a concrete mix which would not require any

effort or compacting equipment to make it flow and take the shape of its form-work. SCC can freely flow under its own weight filling all spaces and automatically levelling at the surface. The applications of SCC are wide and used mainly where compacting equipment cannot be used or simply if the skilled workers needed to handle such equipment are unavailable. These applications include pile foundations, underwater construction, highly reinforced structures etc. The Bingham model which is the simplest and most widely used model to describe concrete rheology [CM09, BGB10, CJLW17] consists of two parameters namely plastic viscosity ($\mu$) and yield stress ($\tau_0$) (As seen is Figure 5.1). A Bingham fluid retains its shape if the shear stress on the fluid is less than $\tau_0$. When the shear stress is above $\tau_0$, the fluid begins to flow and the shear rate becomes linearly proportional to the excess value of shear stress. Although the model is relatively simple, researchers have tried various experimental means to obtain the numerical values of these parameters for a given concrete mix. There still exists no standard methodology to obtain them and the tests, at best, offer only a relative qualitative measure of the parameters.

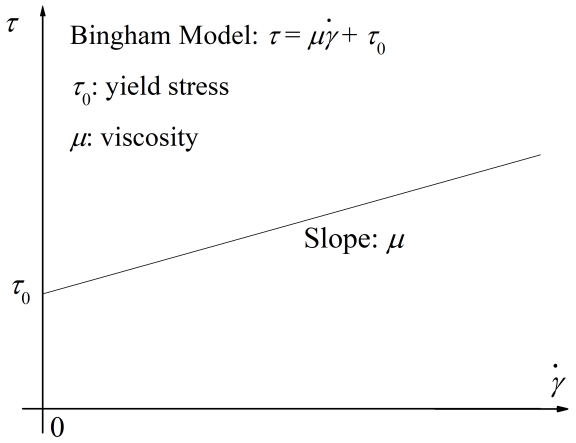

Figure 5.1: Concept of Bingham Model

### 5.1.1 Workability and rheometer tests

There are various standard concrete workability evaluation tests suggested by several standards such as The European Guidelines for Self-Compacting Concrete. These tests include the slump flow test, V-funnel test, L-box test etc. and qualitatively assess certain aspects of concrete flow behaviour. However, these tests can only provide a relative measure of performance rather than quantify fundamental parameters like viscosity and yield stress. It cannot be denied that there is a correlation between the test results and the parameters which must be exploited in order to get closer to quantifying the parameters.

Apart from these standard industry tests, more direct tests, the concrete rheometers have been proposed with the objective of directly obtaining the values of the Bingham parameters. The most used rheometers are BML viscometer [Tat91], BTRHEOM [DLHS+97], RSNS rheometer [Li15] and ICAR rheometer. The ICAR rheometer is shown in Figure 5.2. By measuring the rotation rate and the torque on the vanes, rheometers are directly able to output the values of yield stress and plastic viscosity for that mix.

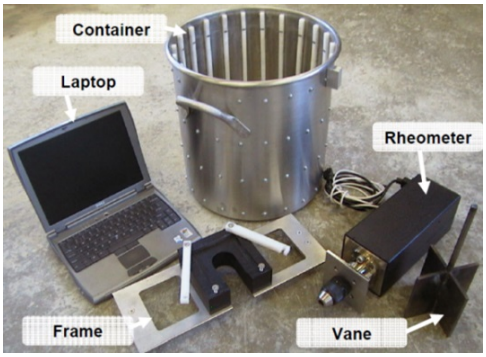

Figure 5.2: ICAR rheometer

In this study the ICAR rhometer was used on a concrete mix and the values of plastic viscosity and yield stress where found to be $1Pa$ and $59Pa{\cdot}s$ respectively. The ICAR rheometer was simulated using the finite volume method with the concrete being modelled using the Bingham model with the same values for the parameters. The pressure distribution on the vanes is shown in Figure 5.3 for a rotation speed of $0.05rps$. The torque on the vanes is compared to ones obtained from experiments. The torques for various rotation speeds are given in Table 5.1. The results from the experiment and simulation match each other well.

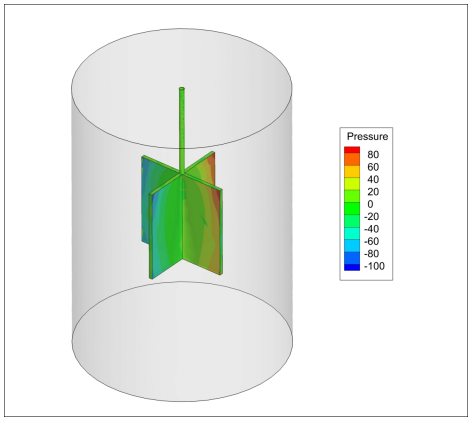

Figure 5.3: Pressure on the vanes of ICAR rheometer (Pa)

Table 5.1: Torque on vanes of ICAR rheometer

| **Speed (RPS)** | **Experimental torque (Nm)** | **Simulation torque (Nm)** | **Relative error** |
|---|---|---|---|
| 0.5 | 1.5000 | 1.3125 | $-0.149$ |
| 0.425 | 1.258 | 1.1235 | $-0.107$ |
| 0.35 | 1.063 | 0.9252 | $-0.13$ |
| 0.275 | 0.695 | 0.7264 | 0.045 |
| 0.2 | 0.497 | 0.5283 | 0.063 |
| 0.125 | 0.398 | 0.3301 | $-0.17$ |
| 0.05 | 0.143 | 0.1320 | $-0.077$ |

The main drawback of rheometers is that different rheometers tend to produce different values of yield stress and plastic viscosity [BF03, BGB10, FCT+12]. This

disagreement along with a lack of general consensus about which rheometer is more accurate renders rheometers only useful for determining the relative performance between different concrete mixes. Rheometers are expensive and hard to be performed on site. Also, the industry demands a fast and simple test to determine the quality of concrete prior to placement, restricting the use of rheometers to the lab rather than in practice.

### 5.1.2 Mathematical models to establish relationship between test results and parameters

Slump flow is closely related to the yield stress [Mur84, CPA96, Dom98] and researchers have attempted to quantify it. [KHMF97] established a relation between yield stress and spread diameter, taking the total volume of concrete into consideration while neglecting the influence of viscosity. This relation is given in (5.1) where $D_f$ is measured spread diameter, $\rho$ is the concrete density, $g$ is the acceleration of gravity and $V_c$ is total volume of slump cone. [RC05] divided the flow behaviour of the slump flow test in to three regimes, namely the pure shear flow, pure elongational flow and the intermediate regimes. It also improved (5.1) by discussing the influence of surface tension effects resulting in (5.2). Where $\lambda$ is the coefficient representing the influence of both surface tension and contact angle.

$$\tau_0 = \frac{225\rho g V_c^2}{4\pi^2 D_f^5} \tag{5.1}$$

.

$$\tau_0 = \frac{D_f^2}{4V_c}\left(\frac{225\rho g V_c^3}{\pi^2 D_f^7} - \lambda\right) \tag{5.2}$$

.

In the slump flow test, the total flow time when spread reaches the final diameter and the time when spreading diameter reaches 500 mm ($T_{500}$) have also been evaluated. [TFS08] studied the relationship between the rheological properties and the flow time. A simple linear relationship was seen between the ratio of plastic viscosity and yield stress to the total flow time. [FCT+12] arrived at an empirical equation for this relationship based on experimental data. [Esp07] studied the relationship between $T_{500}$ and rheological properties by experiments. The result suggested that $T_{500}$ is sufficiently influenced by both yield stress and viscosity. [NPK+10] also arrived at similar conclusions.

[RLR05] proposed an equation to represent the relationship between flow time of cement paste in Marsh cone test and its rheological properties. The author suggested that viscosity and yield stress could be solved directly using the equations if flow times obtained from two different shape Marsh cones were given. The work showed that both viscosity and yield stress had significant influence on flow time. [NRG+06] improved the flow rate evaluation of this method by considering the Reynolds number in the nozzle and using the Herschel-Bulkley model instead of Bingham model. However, when applying their solution to V-funnel test of SCC, the level surface and constant flow-rate assumption was not found to be reasonable

any more [LHC14].

### 5.1.3 Predicting parameters based on proportion of concrete constituents

Another method for predicting viscosity is based on the rheology of concentrated suspensions. Concrete is assumed to be a system where particles are uniformly suspended in fluid. The overall viscosity of mixture is a function of the fluid viscosity and the ratio of particle packing density to the maximum particle packing density. [Far68] developed an equation for multi-modal suspensions of spheres. Its underlying assumption is that the finer particles in a bimodal suspension behave as a fluid medium surrounding coarse aggregate if the size ratio of two type particles is below 0.1. The viscosity (5.4) can be calculated from unimodal viscosity (5.3) of each size range if the difference between them meets the requirement of assumption. $\mu_0$ is fluid viscosity, $\mu$ is the overall viscosity, $i$ is the number of particle classes, $n$ is the total number of particle classes, $\phi_i$ is the volume concentration of certain particle class $i$, $V_i$ is particle volume of certain class $i$, $H(\phi_i)$ is the coefficient between $\mu$ and $\mu_0$, which is a function of $\mu_0$ and $\phi_i$ in case of fresh concrete. Considering conditions of different particle classes varies such as particle shape and size distribution, [MK92] proposed different $H(\phi_i)$ for different classes. [HDLG95] introduced this solution to predict the HPC flow in rheometer, and modified $\phi_i$ in (5.4) as $\phi_i/\alpha_i$, where $\alpha_i$ is the maximum volume concentration of particle class i. Further, [FD98] proposed a semi-empirical equation with same pattern for yield stress prediction, which is based on the assumption that $\phi_i/\alpha_i$ can be used to represent the effective friction between particles.

$$\mu = \mu_0 H(\phi) \tag{5.3}$$

$$\mu = \mu_0 \prod_{i=1}^{n} H(\phi_i) \tag{5.4}$$

$$\phi_i \;=\; V_i \sum_{j=0}^{i} V_j \tag{5.5}$$

Numerical simulation has become an effective research tool driven by the rise in computational power. [BGB10] simulated the mini-conical slump flow test of cement paste and pointed out that the effect of plastic viscosity on spread diameter cannot be neglected when yield stress is small. It suggests (5.6) to modify the spread diameter involving the viscosity to improve (5.2), where $\mu_f^{ref}$ is equivalent viscosity and $D_f^{ref}$ is reference spread diameter. With the knowledge of viscosity according to concentrated suspension theory, [BKK16a] obtained yield stress by matching SPH simulation result of slump flow test with measured data from experiments. [LHC14] modelled a 2D V-funnel test by SPH method to study the proper discharge time.

$$\frac{D_f}{D_f^{ref}} = 1 - 0.13 \ln\left(\frac{\mu_{equ}}{\mu_0}\right) \tag{5.6}$$

### 5.1.4 A novel method to determine Bingham parameters

Despite all the solutions we have seen so far, there is still no consensus on how to determine viscosity and yield stress for a given fresh concrete mix. Analytical solutions for simple tests are based on assumptions which makes the result a rough assumption. The complexity of concrete mixture and variety of admixtures/additions make the predicting solutions rather unconvincing. Experimental solutions require repeating expensive labour. Further, variation of results during testing is inevitable and is a significant factor for cementitious material. Research works based on numerical methods are few and a systematic study is absent. A recent parametric study [SY] has shown that the slump flow and V-funnel tests could be used to determine Bingham parameters by measuring the flow diameter and flow time from both tests respectively. Calibration curves have been plotted by simulating the tests using concrete with varying Bingham parameters. Therefore, by knowing the flow diameter and outflow time from tests, it is possible to quantify the parameters. An overview of this approach has been provided in this section.

#### 5.1.4.1 Geometry and numerical models

In this parametric study the V-funnel test and the slump flow tests are simulated. The tests along with their geometry and dimensions are shown in Figures 5.4 and 5.5.

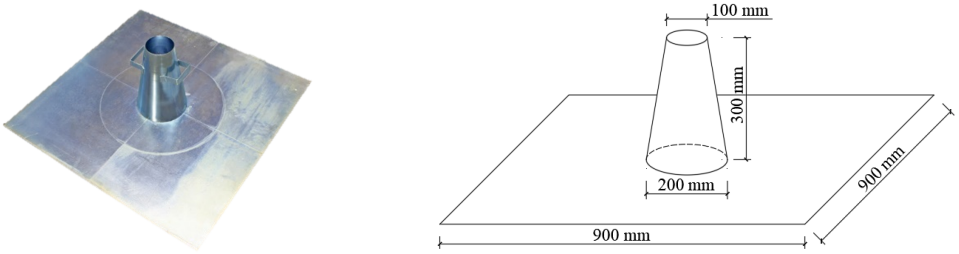


(a) Apparatus (b) Geometry

Figure 5.4: Slump Flow Test

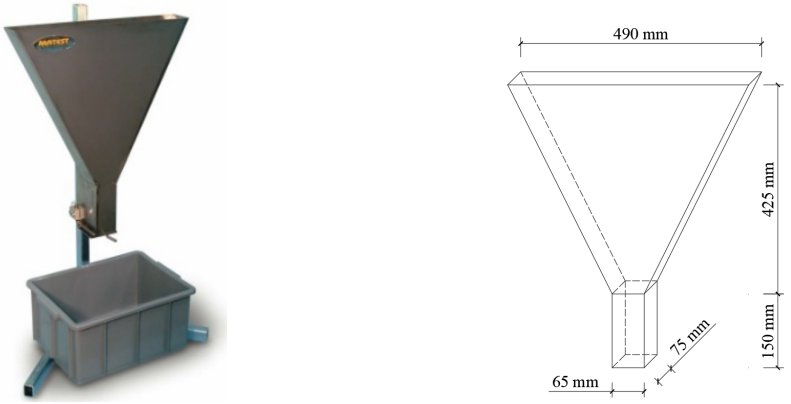


(a) Apparatus (b) Geometry

Figure 5.5: V-funnel Test

The slump flow test consists of two parts, a frustum and a square plate. The top and bottom diameters of the frustum are $100mm$ and $200mm$ respectively while the height is $300mm$. The side length of the plate is $900mm$. The V-funnel test is an extrusion of a V-shaped geometry which is a combination of a rectangle and an isosceles trapezoid. The sides of the rectangle are of lengths $65mm$ and $150mm$. The top and bottom sides of the trapezoid are of length $65mm$ and $490mm$ with a height of $425mm$. The thickness of the V-funnel is $75mm$.

The finite volume method (FVM) is chosen for the simulations and the Navier-Stokes equations are solved for the fluid flow. The Bingham model is used as the constitutive model for the concrete. To model the free surface of the concrete, the volume of fluid method (VOF) is used to track the interface between air and concrete. Air is modelled as a usual Newtonian fluid. The meshes used in the simulations for the slump flow and the V-funnel tests are shown in Figures 5.6 and 5.7 respectively.

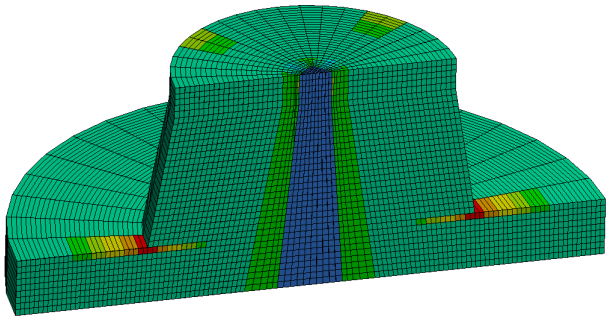

Figure 5.6: Slump flow test mesh (cross-sectional view)

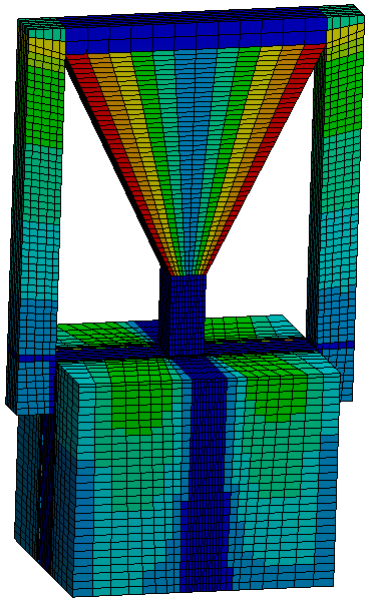

Figure 5.7: V-funnel test mesh

FVM is an Eulerian method and requires a fixed mesh. Besides the concrete, the space where the concrete might flow is also needed to be modelled. Along with

that the space taken by the air also has to be modelled. Sufficient space has to be provided between the concrete interface and the model boundary so that boundary effects do not affect the concrete flow.

A time step size of $0.1s$ was found to produce stable results with reasonable accuracy and is used in all simulations. To increase the computing speed, stability and accuracy of the models a structured mesh is preferred. Coarse meshes result in large inaccuracies and poor stability. At the same time too fine a mesh would require too much computational time. An appropriately fine mesh is required so that both accurate and efficient results are obtained. A convergence study is performed to ensure that the mesh is fine enough to produce accurate mesh independent outputs.

#### 5.1.4.2 Simulation results

The aim of this study is to quantify the relationship between the rheological parameters and test results. A series is simulations of the two tests is performed by varying the values of plastic viscosity and yield stress. Simulations were performed by using 5 different values of yield stress ($10Pa \cdot s$, $30Pa \cdot s$, $50Pa \cdot s$, $70Pa \cdot s$, $90Pa \cdot s$) and 5 different values of plastic viscosity ($10Pa$, $30Pa$, $50Pa$, $70Pa$ $90Pa$). There are 25 combinations for the values which result in 25 simulations for each of the tests.

From the data for both tests different indices can be captured which gives us an idea of the rheology of fresh concrete. For the slump flow test, the final spread diameter will be used in this study. Another parameter which could be obtained is $T_{500}$, which is the time it takes for the spread to reach a diameter of $500mm$ counted from the time the cone is lifted. For the V-funnel test the flow time will be used in the study. The flow time is defined as the time it takes for daylight to first show through the nozzle viewed from the top of the V-funnel. This is demonstrated in Figure 5.8. This is the time when most of the concrete has flowed out of the funnel.

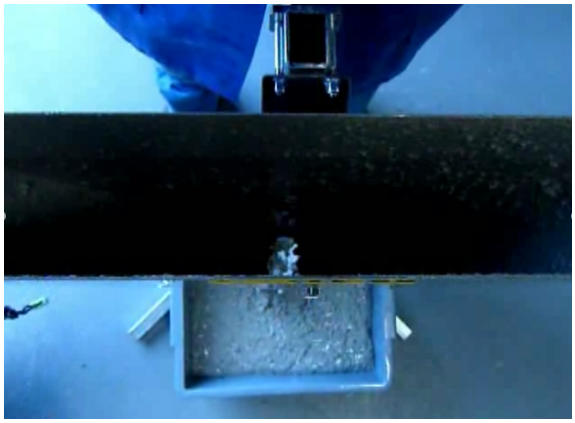

Figure 5.8: Daylight Passing through the nozzle

A rendered result of a typical slump flow test simulation at various stages is shown in Figure 5.9. All slump flow simulations are run for $30s$ which should allow enough time for the diameter to reach its maximum spread value. Similarly, a rendered result of a typical V-funnel test simulation at various stages is shown in Figure 5.10. Simulations are run till concrete inside the funnel runs out.

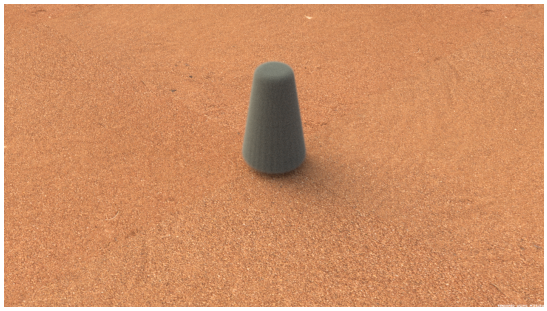

$0s$

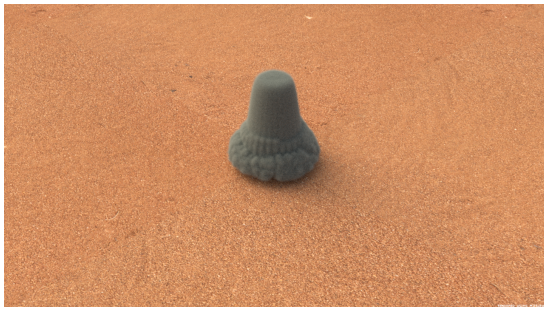

$0.1s$

$0.2s$

$0.3s$

$30s$

Figure 5.9: Slump flow test simulation rendered results

$0s$

$0.1s$

$0.2s$

$0.3s$

$1s$

Figure 5.10: V-funnel test simulation rendered results

#### 5.1.4.3 Analysis and calibration curves

The flow diameter versus plastic viscosity curves are plotted in Figure 5.11 with results obtained from simulations on the slump flow test. Similarly flow diameter versus yield stress curves are plotted in Figure 5.12. The flow time versus plastic viscosity curves are plotted in Figure 5.13 with results obtained from simulations on the V-funnel test. Similarly flow time versus plastic viscosity is plotted in Figure 5.14. From Figure 5.11 we can see that the flow diameter is more sensitive to yield stress than plastic viscosity. The plots suggest that for a particular value of yield stress the maximum diameter does not change by much. The maximum diameter tends to be slightly lower as the plastic viscosity increases, but its effect does not seem to be as prominent as that of yield stress. From Figure 5.14 it is clear that the flow time is more sensitive to the plastic viscosity than the yield stress. For a particular value of plastic viscosity the flow time does not seem to vary by much. For higher values of yield stress the flow time increases, but this increase is not as prominent as that of plastic viscosity.

This finding provides a possibly convenient method to determine the value of Bingham parameters for a particular concrete mix. By performing the slump flow and V-funnel tests on a concrete mix, the flow diameter and the flow time can be determined. With the help of the calibration curves above, these values can be back-traced to unique values of yield stress and plastic viscosity by interpolating the values. These can potentially serve as good estimations of the Bingham parameters values for that particular concrete mix.

This method of determining the Bingham parameters is straightforward and can be performed using already existing and widely used tests in the industry. It is a much cheaper alternative than the rheometer tests and can be performed outside of a lab environment as well. In the next section these calibration curves will be used to determine the values of plastic viscosity and yield stress for an arbitrary concrete mix. The values will be verified by performing simulations and comparing the results to those obtained from the actual tests.

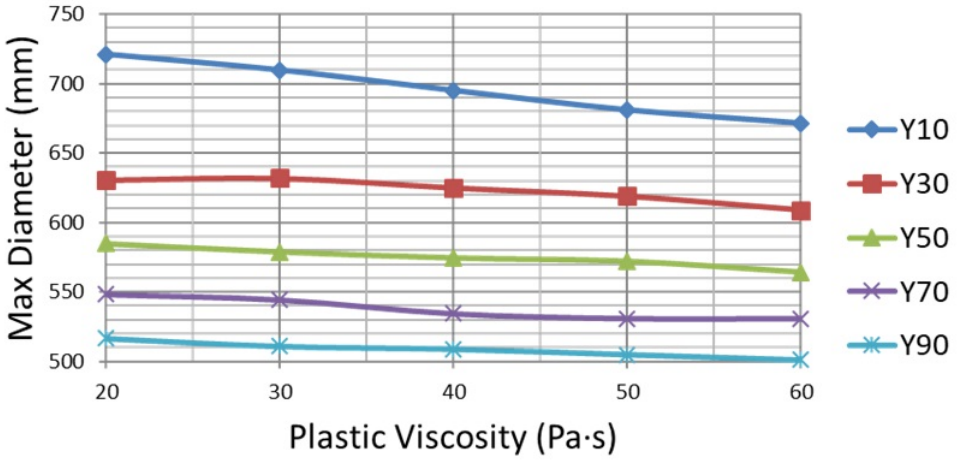


Figure 5.11: Flow diameter vs. plastic viscosity

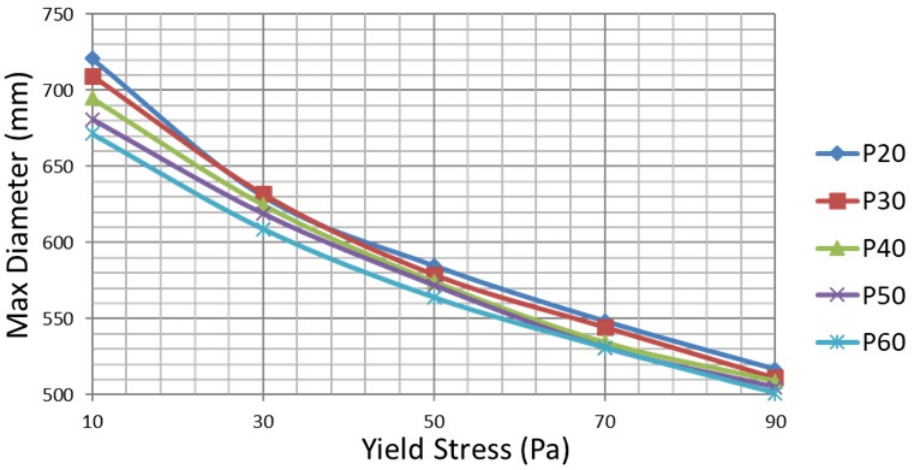


Figure 5.12: Flow diameter vs. yield stress

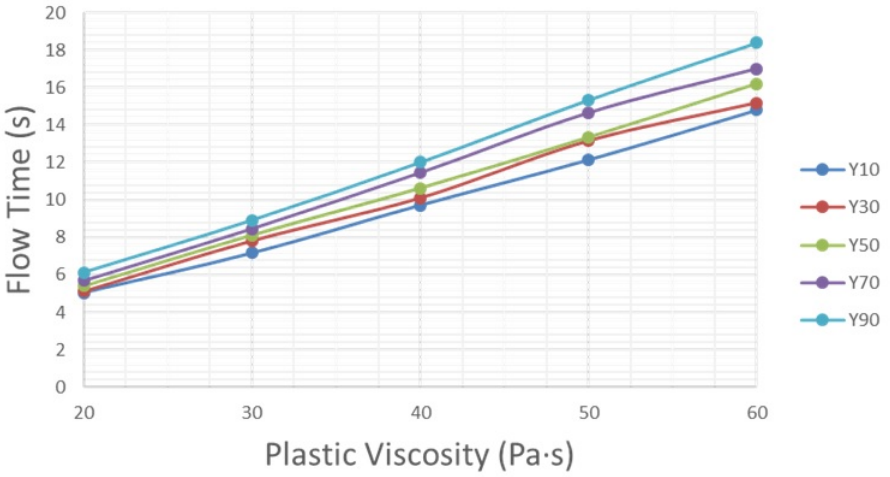


Figure 5.13: Flow time vs. plastic viscosity

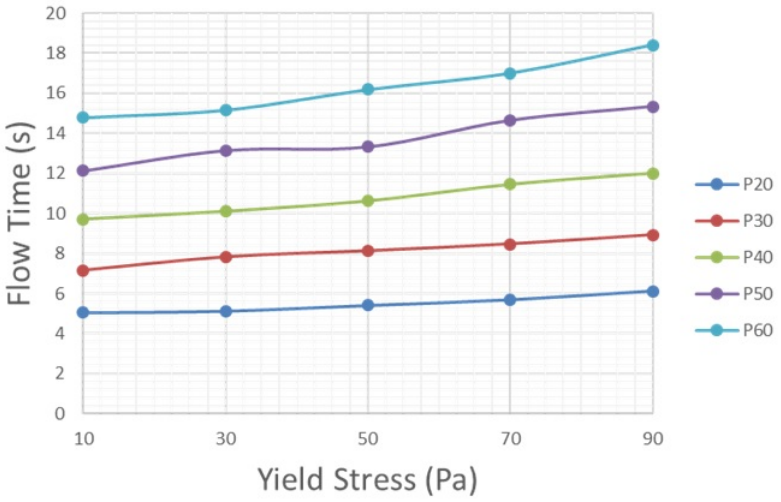


Figure 5.14: : Flow time vs. yield stress

### 5.1.5 Validation of the new method to determine Bingham parameters

To validate the idea behind the method seen in the previous subsection, both the V-funnel and slump flow tests are performed on a randomly chosen concrete mix. The flow diameters and the flow time obtained from the test are used to obtain values of plastic viscosity and yield stress by appropriately interpolating the calibration curves. With these Bingham parameters values, the slump flow and V-funnel tests are simulated using the same method used for obtaining the calibration curves.

A concrete mix was made by adding appropriate proportions of fine and coarse aggregate. Along with the cement and water, admixtures like super plasticisers were added to the mix such that concrete resembles highly workable self compacting concrete used in the industry. A slump flow test was performed using this mix and the final flow diameter was found to be $615.70mm$. The flow diameter is usually measured to the nearest $5mm$ in practice, but for the purpose of this study more accuracy was sought. The V-funnel test using the same concrete mix resulted in a flow time of $5.97s$. Using the calibration curves and interpolation, the values of yield stress and plastic viscosity corresponding to these values of flow diameter and flow time are $27.5Pa$ and $23.5Pa \cdot s$ respectively.

Using the obtained values of the Bingham parameters for the concrete mix a slump flow test simulation is run. The flow diameter obtained form the simulation is shown in Table 5.2. The flow diameter from the test and the simulation are close to each other and the relative error is around 4%. This is a highly encouraging result and the error can potentially be minimised by adding more data points to the calibration curves so that the interpolation can provide better estimates.

Table 5.2: Flow diameter results for new concrete mix

| | |
|---|---|
| Test | $641.25mm$ |
| Simulation | $615.70mm$ |
| Error | $-25.55$ |
| Relative error | 0.04 |

Similarly using the Bingham parameters of the concrete mix a V-funnel test simulation is run. The flow time obtained from the simulation is shown in Table 5.3. The flow time obtained from the simulation is strikingly close to the one obtained from the test with a relative error of only 0.2%. This again is a good result and can be further minimised by adding more data to the calibration curves. We can therefore conclude that the value for Bingham parameters determined by the calibration curves are a reasonably good estimate of the true value.

Table 5.3: Flow time results for new concrete mix

| | |
|---|---|
| Test | $5.97s$ |
| Simulation | $5.96s$ |
| Error | $-0.01$ |
| Relative error | 0.002 |

However, to completely validate the new method it is necessary to put it through a third test. The same concrete mix is then used to perform the L-box test. The apparatus along with the geometry of the L-box test is shown in Figure 5.15. The test contains a vertical hopper and a horizontal flow tank. A gate is placed at the bottom of the vertical section to keep the concrete from flowing. A two or three bar obstacle is placed at the beginning of the horizontal flow tank. The vertical hopper is filled with concrete and the gate is then opened. The passing ability ratio is computed and recorded as the ratio between the depth of concrete in the horizontal and vertical section. Using the values of the Bingham parameters determined by the calibration curves, the L-box test is simulated. A rendered image of the simulation of the L-box test is shown in Figure 5.16.

The passing ability ratio obtained from the simulation and actual test are shown in Table 5.4. The relative error between the test and simulation result is 16.13%. The error is relatively higher for the L-box than it was for V-funnel or the slump flow test. This is understandable as the test is sensitive to the effects of blocking of aggregates in the rebars. The simulation, since performed with the homogeneous Bingham model assumption, is unable to capture this effect and hence results in a higher passing ability ratio than the test. Nonetheless, the results are still close enough to suggest that the values of the Bingham parameters being used are reasonable estimates.

Table 5.4: Passing ability ratio for new concrete mix

| | |
|---|---|
| Test | 0.727 |
| Simulation | 0.844 |
| Error | $-0.113$ |
| Relative error | 0.1613 |

The L-box test and its simulation further bolsters the need for a model that captures the interaction between the concrete constituents and enables modelling the blocking and segregation phenomena. It highlights this main limitation of the Binhgam model. Capturing the interaction between the concrete constituents will not only enable us to simulate the L-box test more accurately but also practical defects often witnessed by the industry can be studied in greater detail. Potential solutions to avoid these defects can also be achieved using the power of simulation tools.

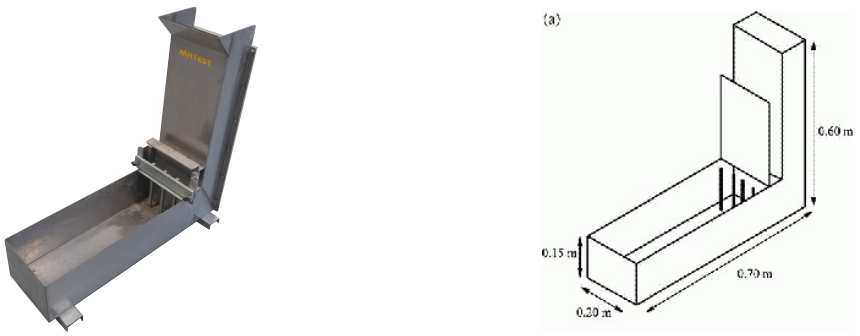


(a) Apparatus (b) Geometry

Figure 5.15: L-box Test

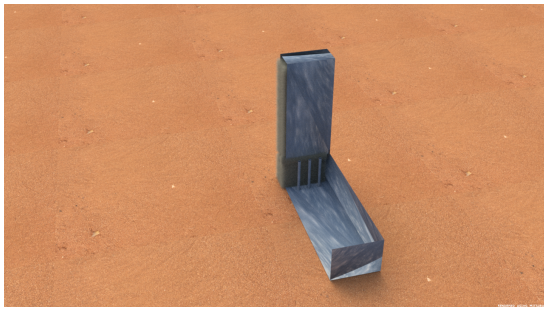

$0s$

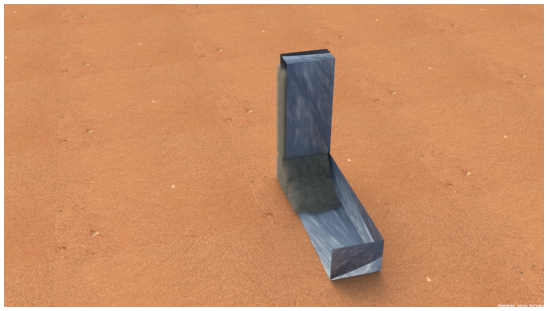

$0.1s$

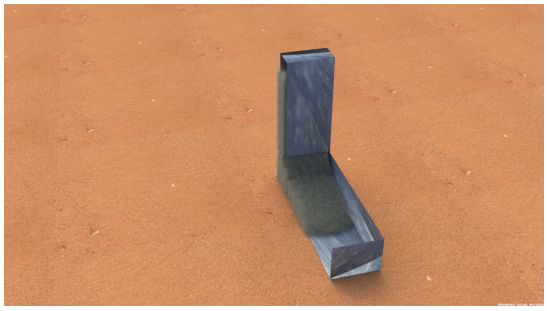

$0.2s$

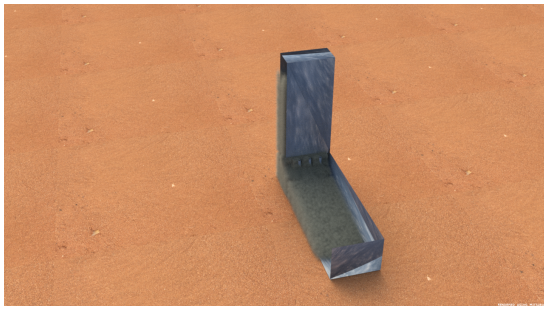

$0.3s$

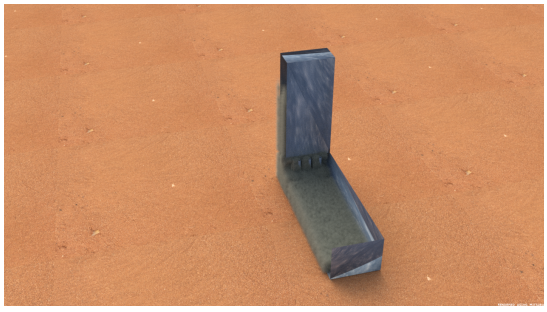

$30s$

Figure 5.16: L-box test simulation rendered results

The validation performed above indicates that the calibrations curves derived as a result of the parametric study can be used to obtain values of the Bingham parameters for any given concrete mix. These values are good estimates and can be used to simulate the flow of that particular concrete mixes in workability tests as well as actual applications. We can potentially get even better estimates if more data points on the calibration curves are obtained. However, the Binhgam fluid model alone cannot capture the effects of blocking and segregation which is witnessed in the L-box test. In the next section the homogeneous Bingham fluid model of simulating concrete flow is applied to an industrial scale problem. The limits of this model are pushed to answer the most urgent questions the industry demands answers for.

## 5.2 Full-scale pile simulation and case study

In this section, the placement of tremie concrete in a full-scale bored pile is simulated using the Bingham model. A case-study is performed by varying the values of yield stress, plastic viscosity and the placement time of each pour. The main objective of performing the simulation is to understand how concrete flows when placed using a tremie pipe which was largely a matter of debate prior to this case-study.

### 5.2.1 Background

A review of problems in bored piles and diaphragm walls using tremie methods, jointly conducted by European Federation of Foundation Contractors (EFFC) and Deep Foundations Institute (DFI), identified certain common issues [ED18]. The root of many problems in casting concrete in deep foundations was found to be the use of inadequate concrete mixes with inadequate workability, insufficient stability or limited robustness. This, in turn, was found to be caused by inadequate concrete specifications and testing procedures. The joint review concluded that effort must be put on designing the right concrete mix.

Concrete Task Group was set up by EFFC and DFI in 2014 to further look into issue surrounding tremie concrete placement. The group was formed to address the problems that contractors experience on site with modern concrete mixes. It was supported by consultants, concrete suppliers and contractors with a view of collaborating to create a practical guide to placement and testing of tremie concrete on site. The primary purpose of the guide was to give guidance on characteristic performance of fresh concrete and its method of placement using tremie methods in bored piles and diaphragm walls, allowing construction of high-quality elements. In addition, the guide intended to propose changes to methods used to specify the concrete mix, as well as methods used to test the mix. The task group carried out a detailed assessment of current best practices and research. It hoped that the guide would provide information for use in future European and American Standards. As a result, the group funded a field research project in both the US and Europe to establish what the acceptability criteria for the concrete provided on site should be.

The group identified that apart from the standard tests such as the slump, V-funnel and L-box tests, an effective way to study and obtain critical information is to perform full-scale tests. Problems identified in full-scale trials can then be

addressed prior to placement of concrete in permanent structures. They also provide opportunities for refining aspects of the construction process and developing compliance parameters. However, such tests are very expensive. Moreover, due to a lack of technology it is not possible to monitor all aspects of the placement process. Numerical simulations offer an alternative approach to study concrete flow. Flow behaviour and phenomenon such as blocking, and segregation of aggregates can be studied using numerical modelling. It also has the capability to offer better understanding of concrete rheology and the effect of mix design on the properties. Thus, the task group investigated further into the use of numerical simulations as an alternative to full-scale tests by collaborating with researchers. The case-study detailed in the current section is a result of the same collaboration.

### 5.2.2 The case-study problem description and its geometry

The geometry of the bored pile is shown in Figure 5.18 and in Figure 5.17. The depth of the pile is 16000$mm$ and diameter is 1500$mm$. The diameter of the tremie pipe is 250$mm$. Diameter of the horizontal reinforcements is 16$mm$ with 200$mm$ spacing between them. 32 vertical reinforcement bars with diameter 25$mm$ are placed equally spaced with a cover of 60$mm$ from the wall. The pile is initially completely filled with bentonite slurry. Concrete is poured in 3 charges with the tremie pipe being lifted once after each pour. The first charge of concrete is poured at a tremie depth of 15.80$m$ from the top with a pouring time of 5$min$. The embedment of the tremie before the second and third pour are 13.907$m$ and 8.814$m$ respectively. The time of pour for the last two charges varies according to the case. Volume of concrete discharged in each pour is $9m^3$. 4 cases are run by varying the yield stress, plastic viscosity and pour time. The details of the 4 cases are given in Table 5.5. The density of concrete is $2400kg/m^3$. The bentonite is modelled with a yield stress of $10Pa$, viscosity of $0.02Pa \cdot s$ and density $1010kg/m^3$.

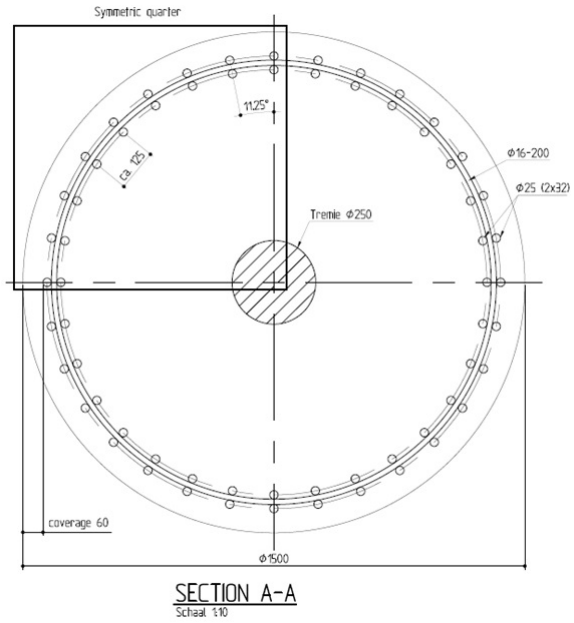

Figure 5.17: Geometry of the bored pile (horizontal cross-section)

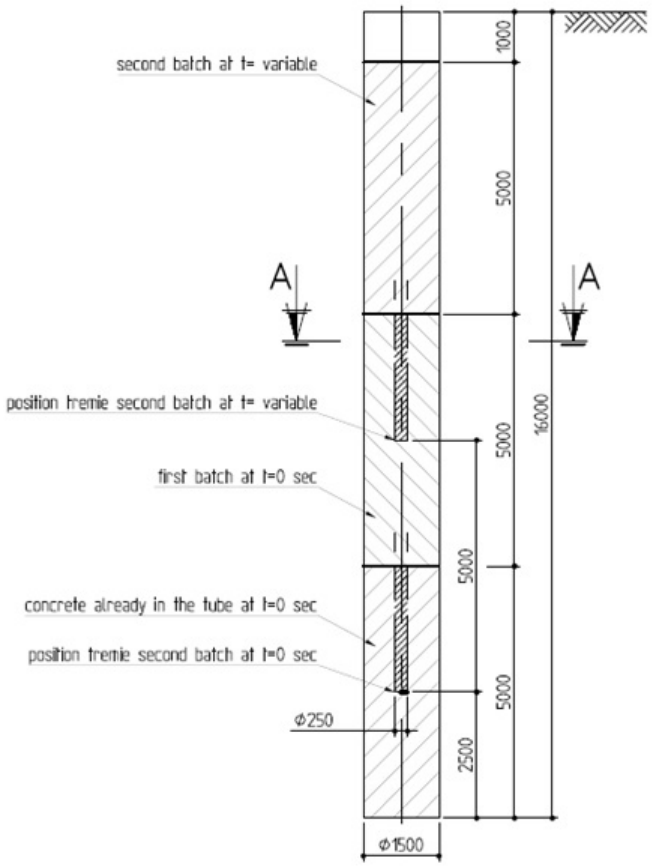


Figure 5.18: Geometry of the bored pile (vertical cross-section)

Table 5.5: Details of the cases

| Case | Concrete charge | Yield stress ($Pa$) | Plastic viscosity ($Pa \cdot s$) | Time ($s$) |
|---|---|---|---|---|
| 0 | 1 | 150 | 30 | 5 |
| | 2 | 150 | 30 | 7.5 |
| | 3 | 150 | 30 | 10 |
| 1 | 1 | 150 | 30 | 5 |
| | 2 | 150 | 10 | 5 |
| | 3 | 150 | 50 | 10 |
| 2 | 1 | 300 | 30 | 5 |
| | 2 | 50 | 30 | 7.5 |
| | 3 | 150 | 30 | 10 |
| 3 | 1 | 50 | 10 | 5 |
| | 2 | 300 | 50 | 10 |
| | 3 | 150 | 30 | 10 |

### 5.2.3 Numerical approach

Just like in the parameteric study in the previous section, FVM is used to solve the fluid governing equations and volume of fluid (VOF) is used to track the interface between the bentonite and concrete phase. The Bingham model is used as the constitutive model for both the concrete and bentonite slurry. Rebars and the

tremie pipe are fully resolved by the finite volume mesh and are treated as 'no-slip' walls. A close-up of the mesh used is shown in Figure 5.19. The total number of elements used are 9139545. A convergence study was performed to ensure that the mesh is adequately refined and that mesh independent results are achieved. The final mesh was selected keeping in mind the computational efficiency. The effect of the tremie lifting is simulated by converting the termie walls into interior faces of the domain each time the tremie is lifted. The domain has an inlet at the top of the tremie pipe through which concrete enters while the outlet is at the top of the pile through which the bentonite slurry exits. The pour time is controlled by using appropriate values of velocity at the inlet. A time step of $0.1s$ is used for all simulations and is found to produce stable and accurate results.

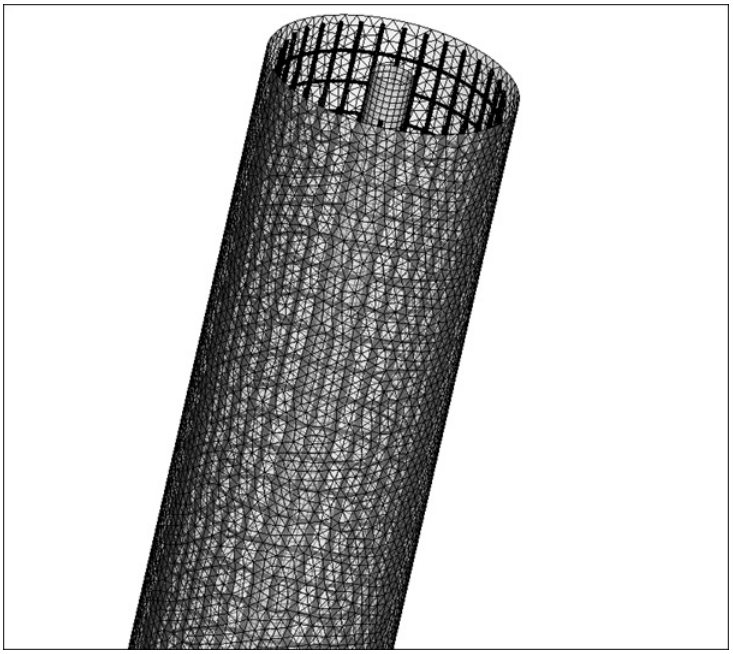

Figure 5.19: Mesh used in the simulation

### 5.2.4 Results and discussion

A rendered version of a typical simulation result at different stages is shown in Figure 5.20. The bentonite has not been rendered in these images. As expected, the concrete exits the tremie pipe at the bottom and displaces an equal amount of bentonite. The level of concrete increases gradually as the simulation progresses and eventually fills up the entire pile. To get a better understanding of the flow pattern actually taking place, the various stages of the placement of concrete using simulations for a typical case is shown in Figure 5.21. In these figures, yellow represents the newest concrete while blue represents old concrete. The main characteristic of these figures is the formation of a bowl shape right below the opening of the tremie. Each time the tremie is lifted, a new bowl shape pattern is formed. The concrete within the bowl is new concrete while the concrete immediately outside the bowl is older concrete. The interface between them is relatively sharp. This can be attributed to the yield property of concrete. The final contour plot of age of concrete for all four cases is shown in Figure 5.22.

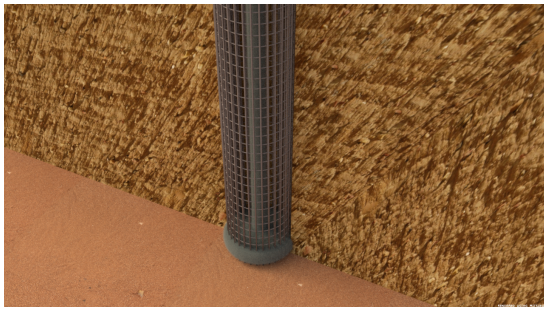

$100s$

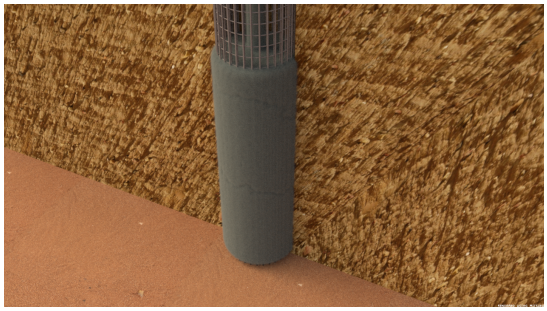

$200s$

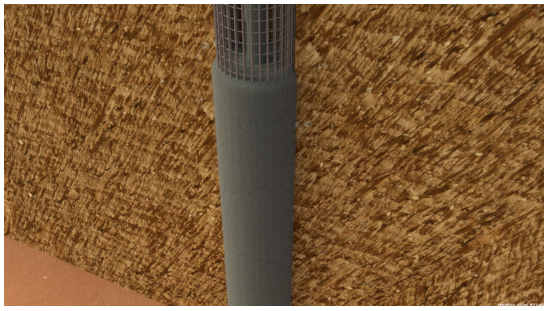

$400s$

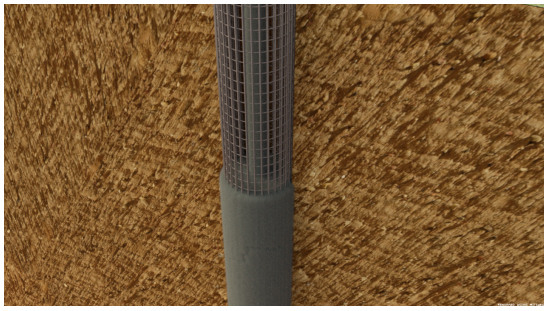

$600s$

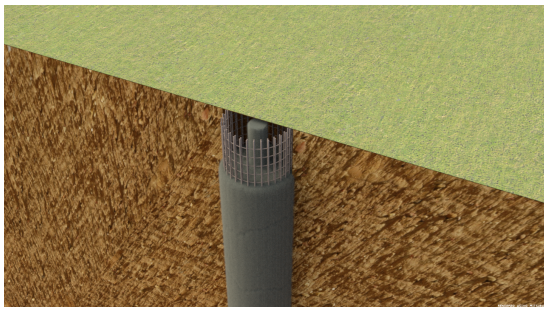

$900s$

Figure 5.20: Pile simulation rendered results

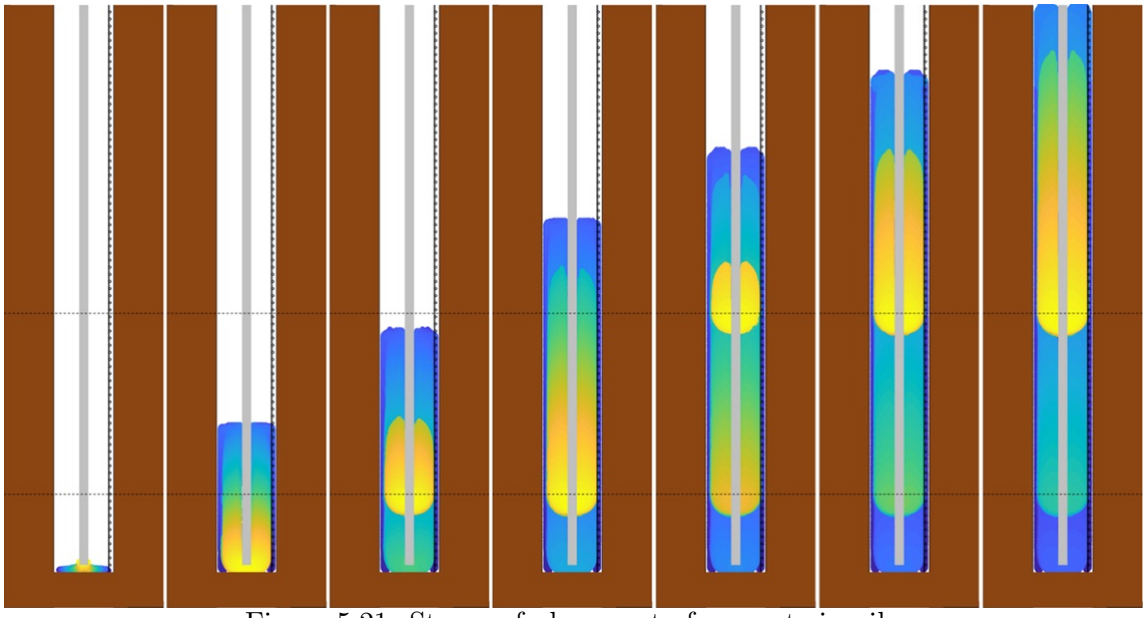

Figure 5.21: Stages of placement of concrete in pile

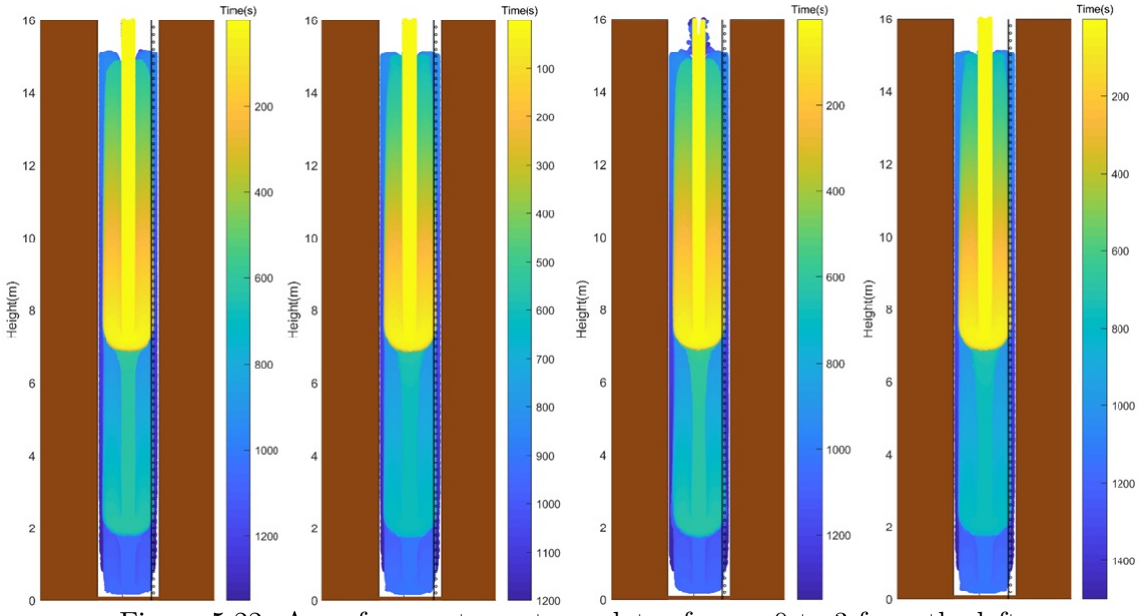


Figure 5.22: Age of concrete contour plots of cases 0 to 3 from the left

The concrete being released from the tremie pipe has enough momentum to push to a certain distance below the opening after which it moves upwards. As we move towards the edge of the bowl, the shear of the moving concrete reduces and drops below the yield stress, suddenly locking the concrete in place, resulting in the sharp interface. The concrete outside below the bowl is therefore yielded concrete locked in position. The concrete within and above the bowl moves upwards as it tries to occupy spaces with the least potential energy. As the concrete nears the surface, it moves to the sides beyond the rebar cage. This explains the old concrete near the pile walls throughout the length of the pile. Once the concrete enters the cover zone it loses its energy and the shear drops below the yield stress, locking it in

position. This initial upward and then sideward movement of concrete in a pile can be confirmed by the streamline plots for a typical case at various stages in Figure 5.23. This figure clearly shows the upwards movement of concrete as soon as it is released from the tremie opening. Towards the top the streamlines point sideways. Also, from the plots of concrete age, we can see slightly newer concrete where the lifted tremie used to be. This is explained by the fact that concrete in the tremie is newer than the concrete surrounding the tremie pipe. Once the pipe is lifted, the concrete in it yields and gets locked into position.

At first glance the plots of concrete age for all cases do not seem to differ from each other much. This indicates that for the given problem statement varying the parameters does not seem to have much of an effect on the final position of concrete. This can be explained by the limited amount of interaction between old and new concrete. Once the tremie is lifted the old concrete gets locked into position and does not interfere with the new concrete being poured in. However, when the tremie is lifted, since the tremie is embedded into the older concrete, the older concrete above the opening continues its journey towards the surface and then to the sides into the cover zone. It then yields and gets locked in the cover zone.

A further analysis on the case study is presented here. The age of concrete is plotted along a line going through the centre of the pile for all cases and the plots are shown in Figure 5.24. The line through the centre of the pile passes through where the tremie was embedded. The concrete in the tremie moves relatively much faster than the concrete in the pile. Hence most of the concrete in the tremie is of the same age. When the tremie is lifted the concrete in the tremie gets locked in position. Hence, we see three horizontal lines, one for each pour. There is an abrupt change of age close to where the tremie is lifted. This in fact represents the interface of the bowl formed due to lifting. The concrete within the bowl is new while just outside it, concrete is old. The penetration of the new concrete into the new concrete can be obtained from this, i.e. the distance of the lowest point of the bowl from the bottom of the tremie pipe can be obtained. The penetration for both lifts is plotted for all cases in Figure 5.25. There seems to be no clear trend to the penetration levels as it depends on the pump rate, viscosity of old and new concrete and their yield stress.

A similar plot is made for a line along the length of the pile at a distance one fourth the radius from the centre of the pile. The plots are shown in Figure 5.26. From this plot we can see that each plot has three slanted lines one representing each of the concrete pours. If the slope of these lines is calculated, they are found to be proportional to the pump rate of that particular pour. This is clarified in Figure 5.27 where the slope for each pour is plotted for every case.

Another similar plot is made for a line along the pile wall. The plots are shown in Figure 5.28. These plots are not as smooth as the previous two due to interference of the rebar cage randomising the distributing of concrete. The scatter plot can be divided into two groups both of which have a general sense of a slope. Each group represents a pour. The group corresponding to the third pour cannot be seen as the concrete from the third pour hadn't reached the pile wall at the time the pile was completely filled.

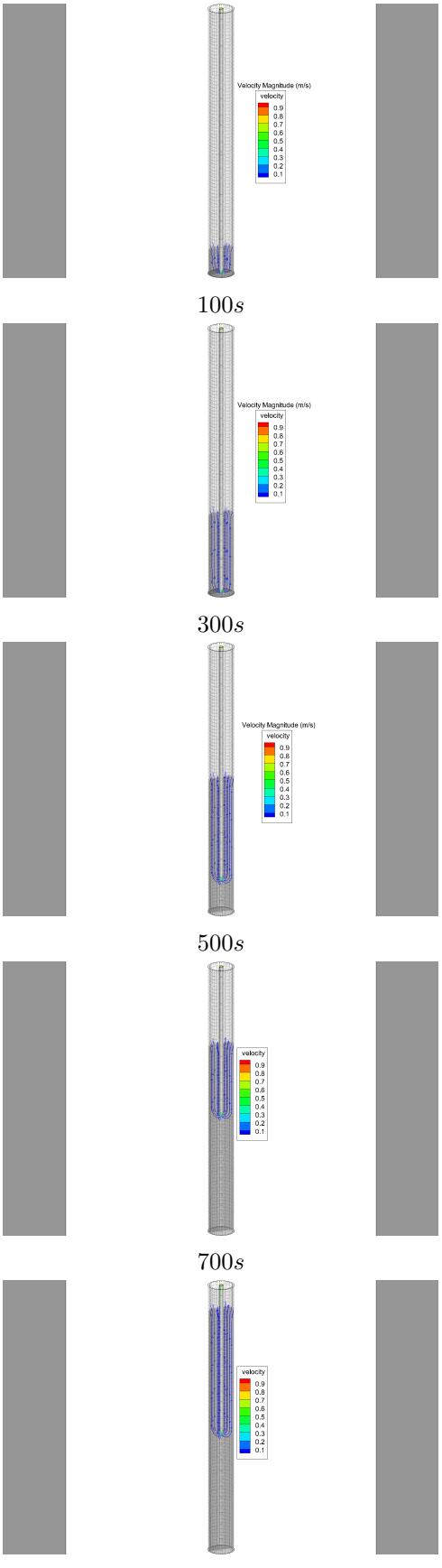


Figure 5.23: Streamlines of pile simulation

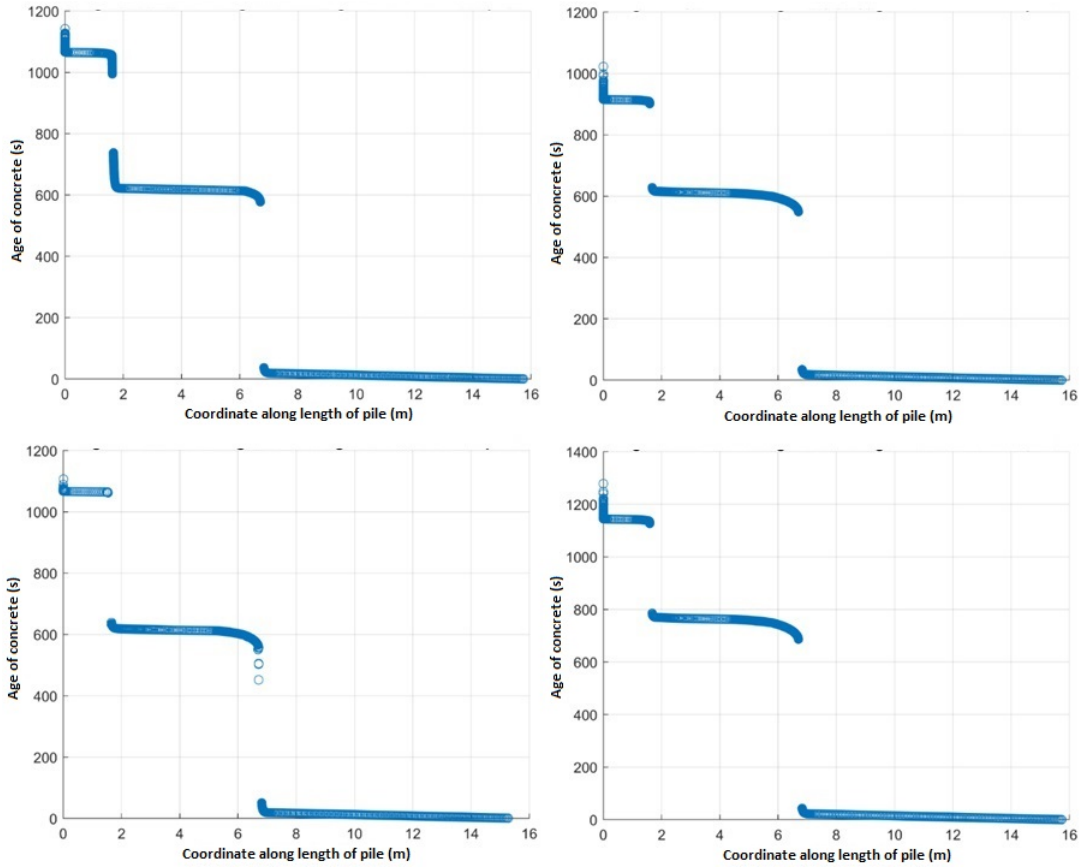

Figure 5.24: Age concrete along the centre line for all 4 cases starting from the top left

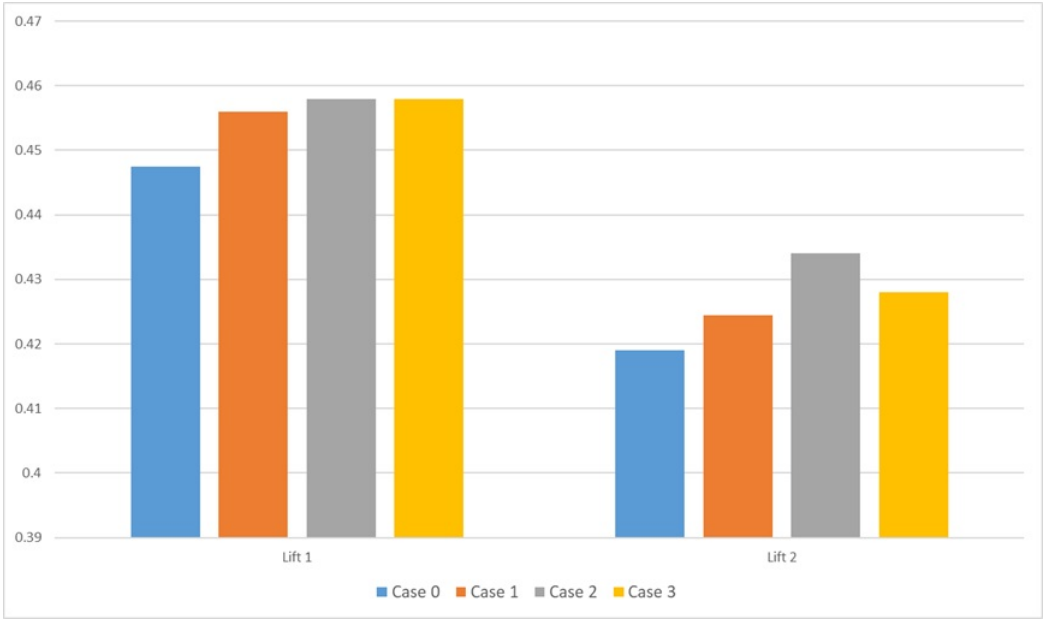

Figure 5.25: Penetration of new concrete into old concrete in metres

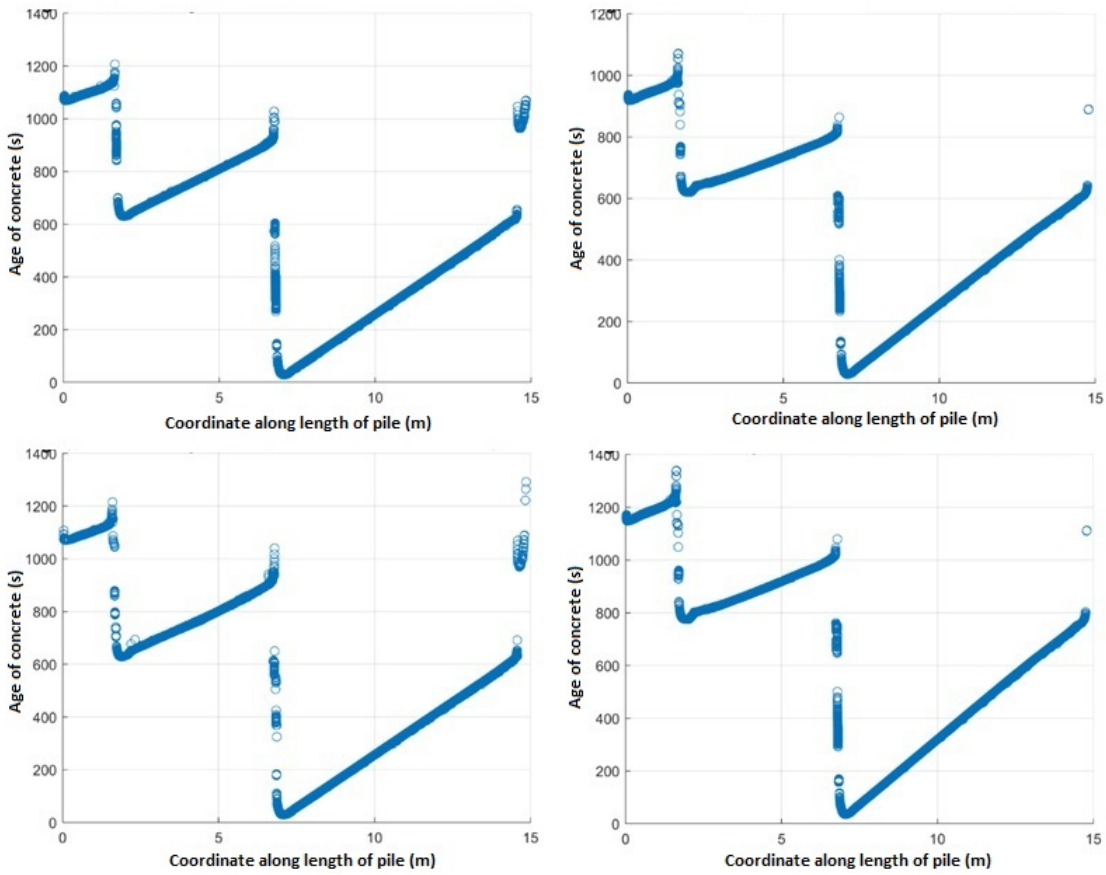


Figure 5.26: Age of concrete along a line at a distance of radius/4 from the centre

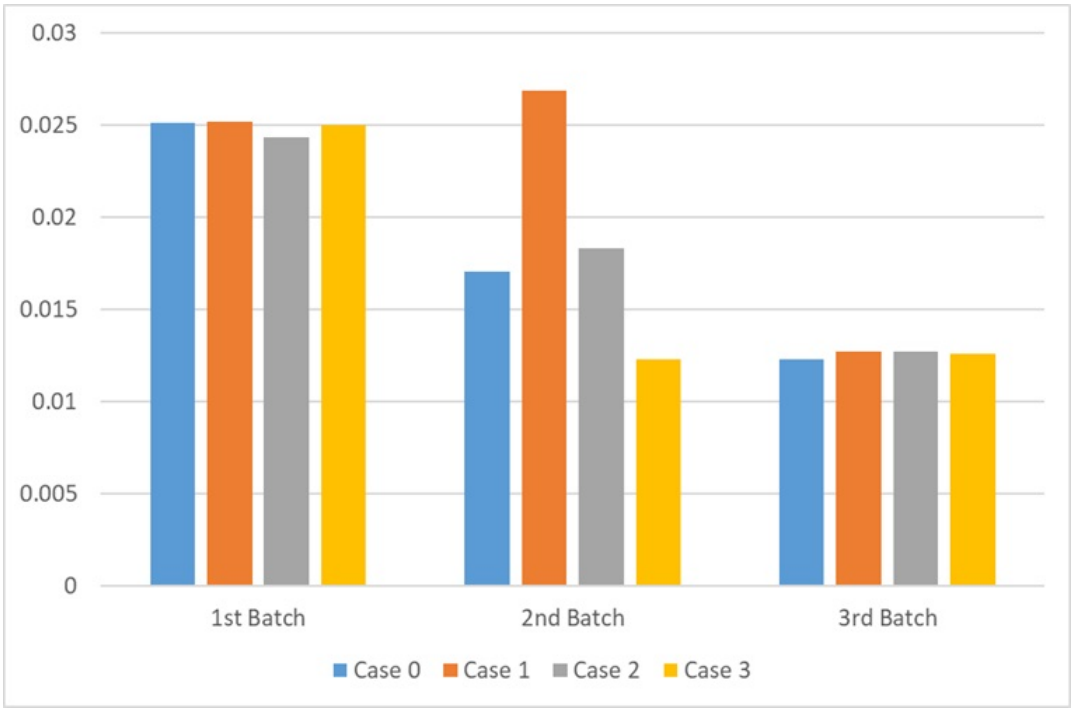


Figure 5.27: Slope of plot for age of concrete along a line through the middle of the pile

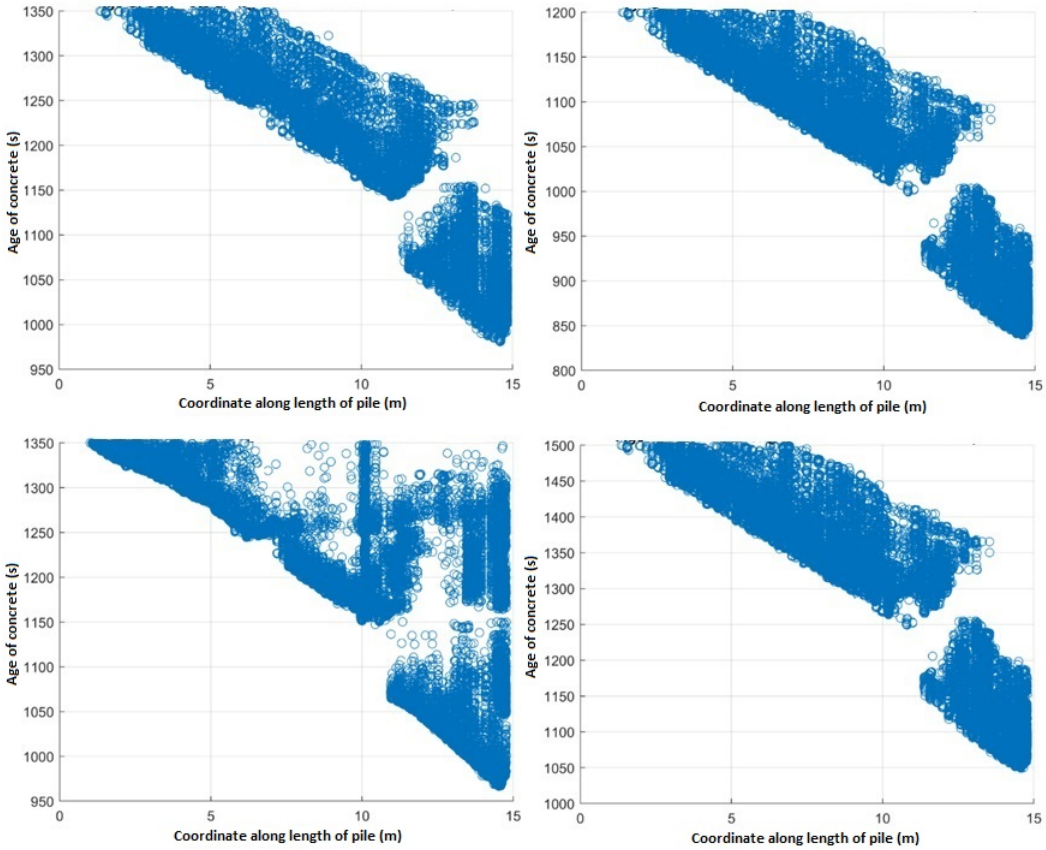

Figure 5.28: Age of concrete along a line near to the pile wall

From the results, it is clear that concrete follows a certain uniform direction of flow. The concrete coming out of the tremie pipe tries to make its way to the top and enters the sides, into the cover zone, once it nears the surface. In the process, it forms a bowl shape which penetrates into the older locked concrete. Concrete beyond the rebar cage is therefore older compared to the concrete within the pile. The results also show us the limitation of modelling the flow of concrete with the homogeneous Bingham assumption. Millions of pounds worth of losses have been incurred due to defective pile placements. These defects are often a result of blocking of aggregates in the rebar cage or segregation of aggregates in certain areas of the pile. None of these defects can be modelled using the current approach. The concrete flows through the reinforced area with lower obstruction than that would occur in reality. Different constituents of concrete are homogeneously distributed throughout the concrete phase leaving no scope to capture segregation. A more sophisticated approach is clearly required in order to model such phenomena.

## 5.3 Conclusions

In this chapter the Bingham model was used to simulate concrete flow assuming the concrete to be a homogeneous fluid. This approach is widely used in literature to model the flow of concrete and there is a general consensus on its use. However, determining the exact values of the Bingham parameters, namely plastic viscosity and yield stress, is a challenge. Various techniques, from rheometers to mathematical

correlations, have been proposed to determine the parameters for a given concrete mix. All the existing methods have weaknesses and there is no general agreement in literature on the use of any single method. In light of this, this chapter looked at a new method to determine the Bingham parameters by simply performing the slump flow and V-funnel test on a given concrete mix. By means of a parametric study in which numerous simulations of the slump flow and V-funnel test were performed, calibration curves were plotted. These calibration curves can be used to determine the value of plastic viscosity and yield stress if the flow time and flow diameter are obtained for any mix. The method, as validated, resulted in very accurate estimates of the true values of the Bingham parameters. However, in the L-box test, the results were not as accurate. The relatively poorer performance of the method in the case of the L-box test can be attributed to the weaknesses in the homogeneous Bingham approach. Since the Bingham model does not model aggregates or constituents separately, blocking cannot be modelled. Blocking of aggregates in the L-box test plays a major role in the end result and it us understandable that the Bingham model does not produce accurate results in its case.

In this chapter the homogeneous Bingham model was also used to model placement of tremie concrete in deep foundation piles. A case-study was performed by varying the value of the parameters for each pour and also varying the time of pour. The study revealed that the flow of concrete follows a peculiar pattern once it exits from the tremie. The yield property of the concrete is responsible for the formation of a characteristic bowl shaped pattern near the end of the tremie. The concrete, that comes out of the tremie, makes its way upwards towards the interface with the bentonite. It then moves sideways into the cover zone where it gets locked into position. This was a major revelation which the industry had no knowledge of prior to this investigation. The placement process can be better designed keeping the flow pattern in mind. However, this study did not answer any questions related to the defects caused by segregation and blocking. The flow was largely unobstructed through the dense rebar cage where one would expect to see a gathering of aggregates struggling to pass through. This highlights the major disadvantage of the homogeneous approach with the Bingham model. In order to simulate such defect causing phenomena more advance techniques of multiphase modelling have to be employed in which aggregates are considered as an entity in the flow rather than them being homogenised with the rest of the constituents of concrete. In the next chapter some of the more sophisticated methods of multiphase flow modelling are applied to simulate concrete flow. The potential of such methods to capture the effects of segregation and blocking are seen with the hope that more insight can be provided to the industry on them.

# Chapter 6

# Application of advanced modelling techniques to simulate fresh concrete flow

In the previous chapter we applied the Bingham model to simulate fresh concrete flow. The Bingham model, in literature, has been accepted to be the best approach to model concrete flow. A novel method to estimate the values of the Bingham parameters was introduced by means of a parametric study. An industrial scale problem was also simulated and a case-study was performed by varying the yield stress, plastic viscosity and the batch placement times. The L-box test performed as a part of the parametric study showed a comparatively large difference between the simulated and experimental results. In the experiment, aggregates got stuck in the rebars and added an obstruction to the flow. This blocking effect was not captured in the simulation as concrete was assumed to be a homogeneous material obeying the Bingham model. The result was a higher passing ability ratio in the simulation. This highlights one of the major drawbacks of Bingham approach towards modelling concrete. The limitation was witnessed again in the case-study. Although the case-study was useful to answer questions surrounding the general flow patterns in tremie concrete placement it completely failed to capture blocking of aggregates in the rebars and issues related to segregation. The industry currently face great challenges posed by defects caused due to segregation and blocking and it is amply clear that the Bingham approach towards modelling concrete flow is unlikely to provide any insights in to the matter.

This chapter attempts to apply more sophisticated multiphase flow modelling techniques to simulate concrete flow. The potential of these techniques to capture the interaction between the constituents of concrete have been demonstrated. The hope is to gain a better understanding of the science behind segregation and blocking and to provide solutions to minimise its effects. Concrete, as we know, is also a thixotropic material. This means that when no shear is applied to it, structural build-up causes it to thicken over time, while when under shear, the material thins over time. The Bingham approach in its raw form is not able to model the thixotropic nature of concrete. This chapter also explores a potential method to capture this time dependant behaviour.

## 6.1 Modelling thixotropy

Till now, in this work, we have looked at concrete as a homogeneous material which obeys the Bingham model. This assumption is accepted in literature and is completely valid if the 'bulk' flow behaviour is concerned. In the Bingham model, the non-Newtonian nature of concrete is captured fairly accurately. Concrete, when under no shear, effectively behaves as a solid. In fact it is not until the shear stress exceeds a certain yield stress that it gains the ability to flow. Once concrete begins to flow the ratio between shear stress and shear strain is constant and is termed as the plastic viscosity. However, concrete displays additional complex behaviour which we have chosen to ignore to this point. It is observed that if concrete is left unstressed for a long enough time, concrete thickens and becomes increasingly difficult to get flowing. Similarly, once enough shear is applied to get the concrete moving, it thins over time and becomes increasingly easier to keep flowing. It is to be noted that this behaviour is observed even before the effects of hydration kick in.

To fully simulate concrete flow, it is necessary to model the effects of thixotropy. Till now we have ignored these effects and used the Bingham model to simulate concrete flow. It is found that the effects of thixotropy become significant only after $15min$ of its production. It can therefore be assumed that thixotropy is insignificant for fresh concrete in the first $15min$ of its mixing. After the initial mixing, concrete can be kept agitated up to the point where it is to be placed to negate the effects of thixotropy. This is common practice when transporting concrete from the ready mix plant to the construction site. In the previous chapters we have thus assumed concrete simulated to be fresh concrete used immediately after its mixing. Wherever experimental comparisons were necessary, the use of fresh concrete was ensured. However, in the industry, applications where thixotropy becomes a significant factor is very common. An example of this is when concrete is to be placed in layers like when casting pavements or roads. A model which considers the effects of thixotropy is therefore critical when simulating placement of concrete in such type of scenarios.

Concrete is known to display thixotropic or time-dependant behaviour. This can affect certain placement procedures which pour concrete in layers. Thus modelling thixotropy is critical to the successful simulation of such techniques. It is observed that the yield stress of concrete increases the longer it is kept at rest. This is due to structural build-up at the micro-scale as a result of flocculation of cement particles. This build-up can be broken down if a large enough shear stress is applied to the concrete. The thixotropy caused due to flocculation of cement particles is known as reversible thixotropy as its effect can be reversed by subjecting the concrete to strain. Stiffening caused due to the hydration of cement is referred to as irreversible thixotropy as the effects of hydration cannot be reversed. Thus the thixotropy of concrete can be classified as either reversible or irreversible. In the context of fresh concrete flow, in most modern applications, retarders are often used to delay the onset of hydration. It is safe to assume that in most applications where best practices of concrete placement procedures are followed, irreversible thixotropy is not a significant factor. Therefore in this section only reversible thixotropy caused by flocculation is discussed.

It is evident that a more sophisticated constitutive model than the Bingham

model is required to model the effects of thixotropy. We can expect that any such model will have time derivatives since the basis of thixotropy lies in the properties of concrete being time dependent. The effects of reversible thixotropy can be modelled by slightly modifying the Bingham model [Rou06b]:

$$\begin{aligned} \tau &= (1+\lambda)\tau_0 + \mu\dot{\gamma} \\ \frac{\partial\lambda}{\partial t} &= \frac{1}{T} - \alpha\lambda\dot{\gamma} \end{aligned} \tag{6.1}$$

where $\lambda$ is the flocculation parameter, $T$ is the characteristic time for flocculation and the term $1/(\alpha\dot{\gamma})$ is the characteristic time for deflocculation. Two extra parameters are therefore introduced into the original Bingham equations.

In this section, the Bingham model used in the simulation of concrete in the previous chapter is replaced by the above model. To demonstrate the effect of thixotropy using this model, a two-dimensional case of concrete flow is simulated. This demonstration follows a certain series of events. A cube of freshly prepared concrete is allowed to deform under the effects of gravity until it achieves a stable configuration. The concrete is kept at rest for $2000s$ (around $35min$) to allow for structural build-up. Then a cube of freshly prepared concrete, with the same properties, is introduced nearby and allowed to deform under gravity interacting with the concrete already present. The interaction between them is observed. The set-up is shown in Figure 6.1. Values of the parameters used are shown in Table 6.1. Two cases are run, one with the thixotropic model being implemented and one without (the unmodified Bingham model).

Table 6.1: Values of properties used in thixotropy simulation

| | |
|---|---|
| $\rho$ | $2400kg/m^3$ |
| $\tau_0$ | $500Pa$ |
| $T$ | 200 |
| $\alpha$ | 0.003 |

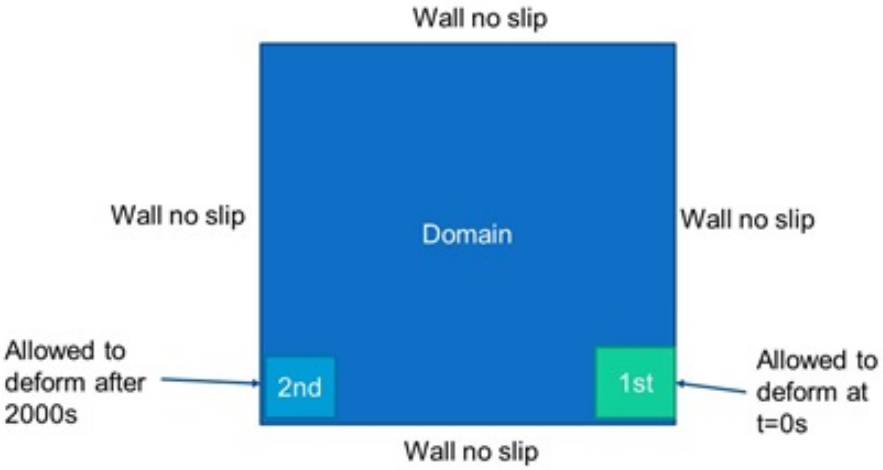


Figure 6.1: Set-up for demonstration of thixotropy simulation

Stages of the simulation with the thixotropy model not implemented is shown in Figure 6.3. Similarly, stages of the simulation with the new thixotropy model

implemented is shown in Figure 6.4. The final configurations and positions of concrete from both the simulations are shown Figure 6.2. From the results we can see that in both cases the first cube deforms under gravity forming a pile of concrete. This concrete attains a stable configuration after it yields. In both simulations the process and the final configuration of the concrete are similar with hardly any difference between them. This is understandable as at this stage not enough time has passed for the effects of thixotropy to kick in. However, in the next stage the concrete from the first block is kept at rest for $35min$ after which a fresh block of concrete is allowed to deform. We see that in the case without thixotropy, the new concrete pushes the older one and mixes with it to form a continuous surface at the top. For the case in which thixotropic effects have been modelled, the new concrete is unable to push the older concrete back and forms a new layer on top of it. It thus, forms a discontinuous jagged surface at the top. The concrete of the first block thickens due to thixtropic effects and is not easily displaced by the energy of concrete from the second block.

The simulations give us an idea of the effect thixotropy can have on placing concrete in layers. If the second layer is placed after significant structural build-up it can lead to separated and hence weak interfaces between layers. Thus using a slightly modified version of the Bingham model and by introducing two new parameters, the effects of thixotropy on the concrete can be simulated. In certain applications, like in the case of placing concrete in layers, there can be a significant delay between placing concrete batches. During this delay, the stationary concrete can thicken disallowing proper mixing of the concrete from different batches. This often leads to defects. Although the effects of hydration can be delayed, the structural build-up of reversible thixotropy remains an issue. Modelling reversible thixotropy gives us an opportunity to better understand the effects of decisions made in concrete placement procedures and better practices to do so. It is thus critical to develop more sophisticated models to simulate thixotropic effects like then one introduced in this section.

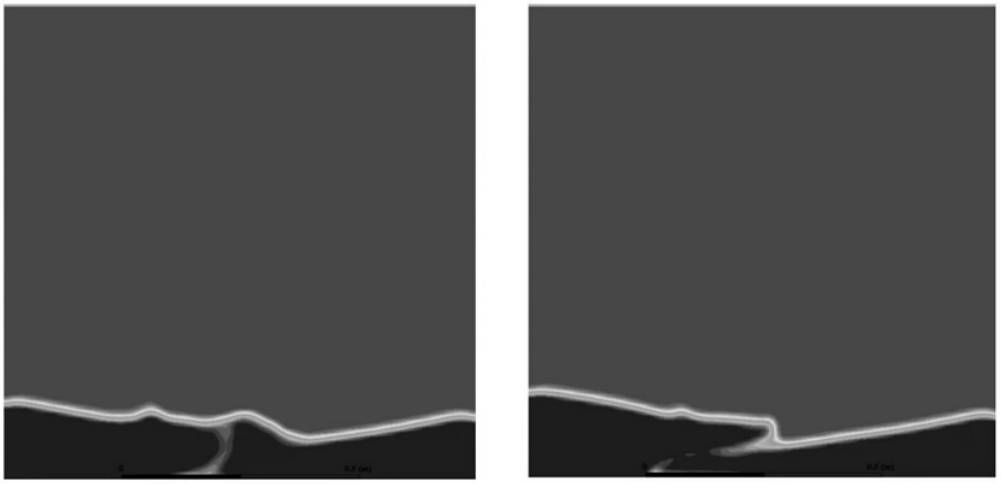

Figure 6.2: Final configuration of concrete in the simulation without thixotropy (left) and with thixotropy (right)

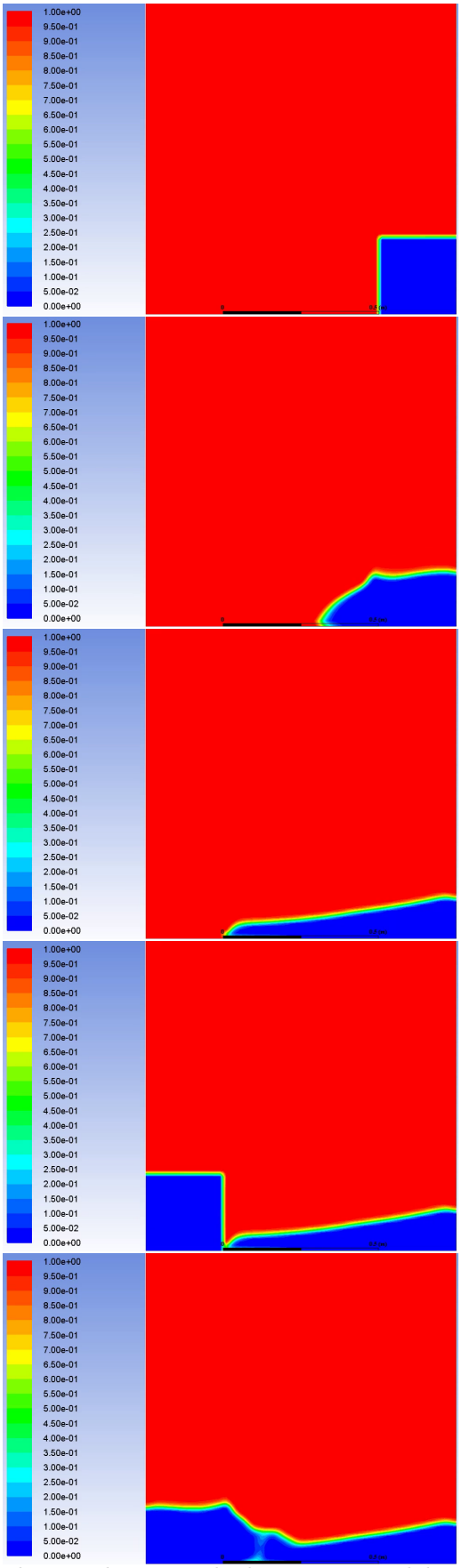


Figure 6.3: Stages in the simulation with thixotropy model not implemented (only Bingham model)

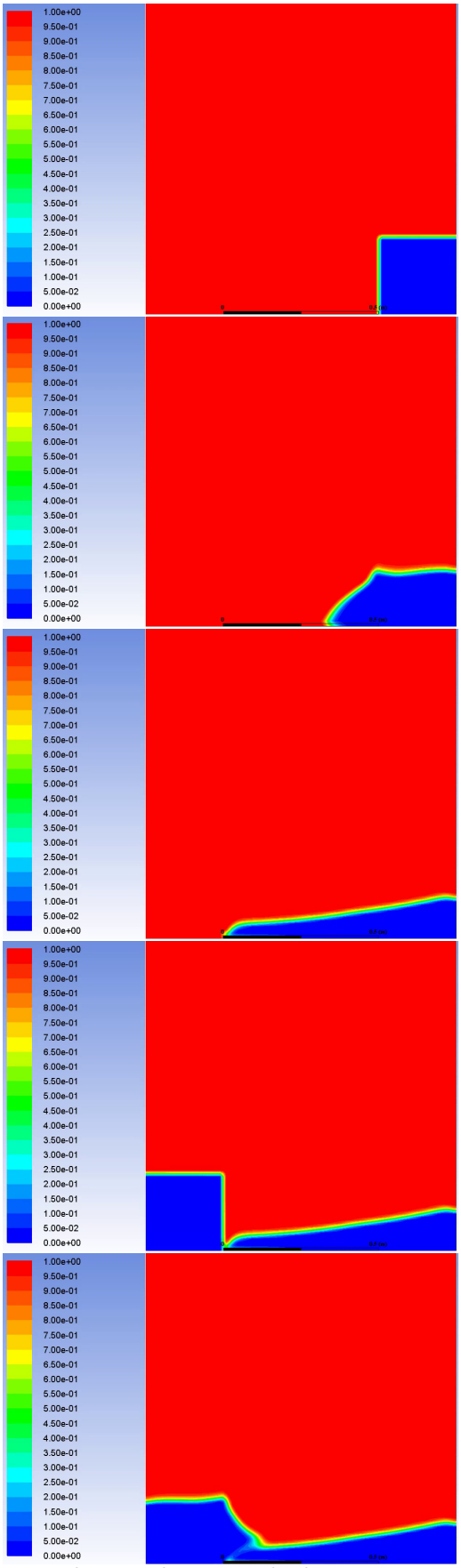


Figure 6.4: Stages in the simulation with thixotropy model implemented

## 6.2 Discrete particle modelling

In the last chapter we have seen the limitations of using the homogeneous Bingham fluid approach of modelling concrete flow. Although it works perfectly well for tracking the bulk flow of concrete, interactions at smaller scales are missed. As a result the effects of segregation and blocking cannot be modelled using this technique. In order to model these defect causing effects, constituents of concrete must be considered and modelled in some manner. In this section, the use of discrete particle modelling (DPM) is explored to model coarse aggregates in the concrete mix.

Concrete is a mixture of cement, water, fine aggregates and coarse aggregates. Of these constituents, individual coarse aggregates are of a scale much larger than individual components of the others. Thus the mixture of cement, sand and water, can be assumed to be a single phase while the coarse aggregates can be considered as a separate phase. In fact, the mixture of sand, cement and water is known in the industry as mortar and we can therefore term this phase as the mortar phase. Modelling concrete as a multiphase material constituting of the mortar phase and coarse aggregate phase adds a whole new level of sophistication to the concrete flow modelling problem.

It is found that the mortar phase behaves like a Bingham fluid. The homogeneous Bingham approach we have used to model fresh concrete flow in the previous chapter can be used to model mortar. In fact it seems much more appropriate to do so for mortar than for concrete since mortar usually remains well mixed. Assuming it to be homogeneous, especially when observed from the coarse aggregate scale, seems valid. There are, however, defects caused by phase separation at this small scale like bleeding. Modelling bleeding is out of the scope of this work but is critical from the perspective of the larger research on concrete flow modelling. Coarse aggregates can be modelled using DPM by assuming them to be discrete particles which interact with the continuous mortar phase. In DPM, particles are modelled mathematically as spheres whose motion is governed by Newton's laws of motion. These particles interact with the continuous phase via drag and pressure gradient forces. The limitation of this technique is that the presence of particles, in terms of space occupied by the discrete phase, is not considered by the continuous phase. This is a major drawback and thus very accurate results cannot be expected with this method. Nonetheless, the potential of this method is explored in the following sections.

### 6.2.1 Simulating the column segregation test

The DPM technique, described in the previous section, is applied to simulate the column segregation test. The experimental set-up of the test is shown in Figure 6.5. The height of the column is $600mm$ with a diameter of $200mm$. It is divided into three sections height-wise with the top section $165mm$, middle $330mm$ and bottom $165mm$ in height. To perform the test, freshly prepared concrete is poured into the column. It is then allowed to stand undisturbed for $15min$. Immediately after that period, a collector plate is inserted between the top and middle section and the top section is removed. Similarly the middle section is removed by inserting a

plate between the middle and bottom section. With the three sections separated, the aggregates from the top and bottom section are sieved off and their weight for each section is measured. The following formula is used to compute the percent static segregation.

$$S = 2 * \frac{(CA_B - CA_T)}{(CA_B + CA_T)} * 100 \tag{6.2}$$

where $CA_T$ and $CA_B$ is the mass of concrete in the top and bottom section.

The experiment described above is recreated via simulation using the DPM technique. In the simulation, aggregates of sizes ranging from $10mm$ and $20mm$ are modelled as spherical discrete particles while the mortar is modelled as a Bingham fluid. Properties of the mortar and aggregates are given in Table 6.2. The particles are initially distributed equally in the cylinder. The simulation is run till a time of 15 minutes.

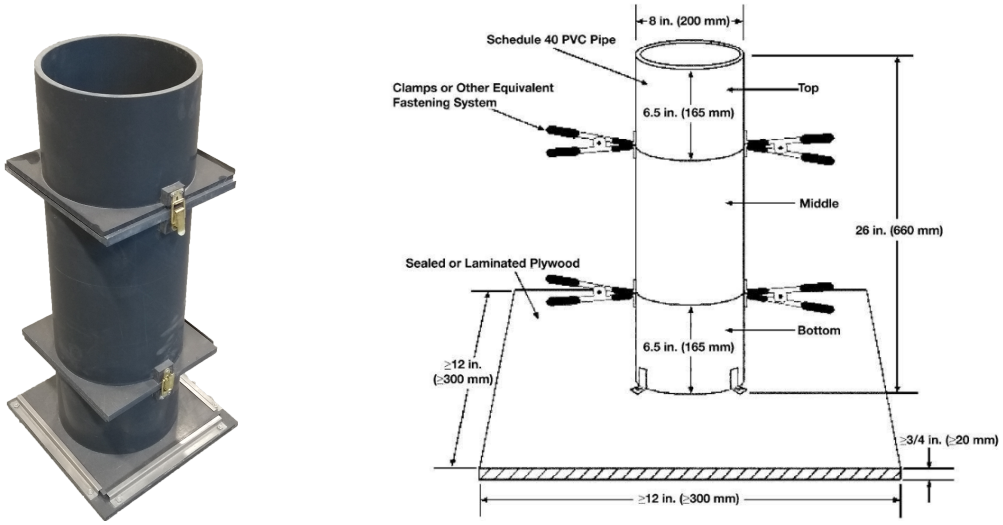


(a) Apparatus (b) Geometry

Figure 6.5: The column segregation test

An instance of the simulation is shown in Figure 6.6. Particles exert drag forces on the mortar as a result of being pulled down due to gravity. The aggregates are much denser than the mortar mix. This force causes a stress that exceeds the yield stress of the fluid and the mortar immediately surrounding the aggregates flows, allowing them to sink towards the bottom. Heavier particles sink at a larger rate. This mode of segregation is known as static segregation and occurs only when the weight of the aggregates exceeds the capacity of the yield property of mortar to resist it. Such situations occur when the yield stress of the mortar is very low as in our current example. The simulation is stopped after running it for $15min$ in simulation time. The mass in the top and bottom sections of the cylinder before and after the simulation is shown in Table 6.3. By using the formula introduced above, the static segregation ratio is calculated to be 7.19%. For an unstable mix, like the one we have simulated above, this number is similar to values found by performing the test in practice.

Table 6.2: Properties of mortar and aggregates

| | |
|---|---|
| Yield stress of mortar | $10Pa$ |
| Plastic viscosity of mortar | $10Pa$ |
| Density of mortar | $2200kg/m^3$ |
| Density of aggregates | $2700km/m^3$ |

Table 6.3: Result of DPM simulation on column segregation test

| Time | $0min$ | $15min$ |
|---|---|---|
| Mass of aggregates in top section | $1.68kg$ | $1.58kg$ |
| Mass of aggregates in bottom section | $1.69kg$ | $1.83kg$ |

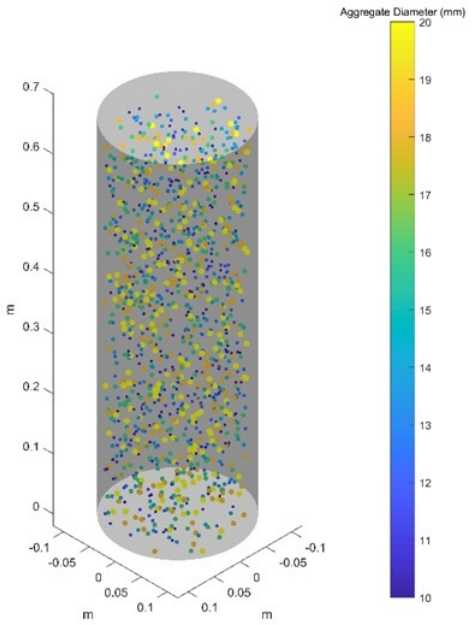


Figure 6.6: Column segregation test

It can be seen that DPM is a useful tool in modelling concrete as a multiphase material. Using this strategy, static segregation can be modelled which was not possible with the homogeneous Bingham approach. In the above simulation, collision between the particles was not modelled since the particles were evenly distributed and particle overlap did not happen. Also collisions do not significantly affect the column segregation test as the rate of sinking would hardly be influenced by it. The major drawback of this approach however is the fact that the mortar phase does not consider the presence of the aggregates in terms of volume occupied. The only coupling that exists are the drag and pressure gradient forces that are exchanged. The problem is therefore weakly coupled compromising the physical accuracy. The ability to track aggregate motion is however a step in the right direction.

### 6.2.2 Modelling segregation in the pile bore

In this section, DPM is applied to the full-scale pile simulation case which was introduced in the previous chapter. DPM has the potential to provide some sort of

insight into the mechanism behind segregation in piles. The modelling techniques used are similar to the ones used in the previous chapter with the difference being that the concrete phase is separated out into the mortar phase and the aggregate phase. The mortar phase continues to be modelled using the Bingham approach along with the bentonite. VOF is used to track the interface between them. Aggregate sizes of $15mm$ and $20mm$ are used and are injected in equal proportion along with the mortar from the tremie. The tremie pipe is lifted in 5 places during the simulation.

An instance of the simulation with the position of aggregates can be seen in Figure 6.7. There is evidence of lighter blue particles on the top and heavier red particles at the bottom of the pile. The concrete coming out of the tremie pipe contains more or less equal proportions of the two sizes of aggregates. As we have seen from the case-study in the previous chapter, this concrete forces its way upward towards the interface between the concrete and mortar. The heavier particles move to the top slower than the lighter particles. This is because a larger drag force is needed to move them upward against their weight. The percentage of heavier particles is therefore higher in the bottom sections than in the top. Such type of segregation is referred to as dynamic segregation since it occurs when the system is in motion. The larger forces required to displace heavier aggregates results in dynamic segregation. Any type of concrete mix is susceptible to dynamic segregation irrespective of the yield stress. As we have seen in the case-study, each time the tremie is lifted, a bowl shaped pattern of flow is formed below the tremie from the concrete coming out of it. The concrete outside this bowl towards the bottom side ceases to flow since the mortar yields. Within the yielded concrete, the aggregates get locked into position. Although unstable mixes may be susceptible to static segregation even at this point, a well designed concrete mix should not allow this. The moving concrete within the bowl continues to be subjected to dynamic segregation.

The number of particles is plotted against height of the pile in Figure 6.8. The vertical dotted lines represent where positions of tremie lift. Towards the bottom of the tremie we see a higher number of heavier particles while at the top there are a greater number of lighter particles. Also, in positions where the tremie is lifted there is a spike in the number of particles and then a gradual decrease. There also appears to be a cross-over of heavier and lighter particle for each lift. This suggests that lifting of the tremie influences the segregation and number density of aggregates.

The results discussed show the usefulness of the DPM technique in providing insight into dynamic segregation that often plagues the construction industry. Further investigations would lead to a better understanding of this technique and its usefulness in modelling fresh concrete flow. DPM adds a degree of sophistication to the modelling of fresh concrete flow despite its obvious limitations on physical accuracy. An even more advanced approach would consider the presence of the particles and its effect on the fluid phase. Also modelling the interaction between the aggregates could enable the simulation of blocking of aggregates in the rebars. The next section takes the concepts we have applied in the use of DPM to overcome its limitations. An even more powerful method is applied to model fresh concrete flow.

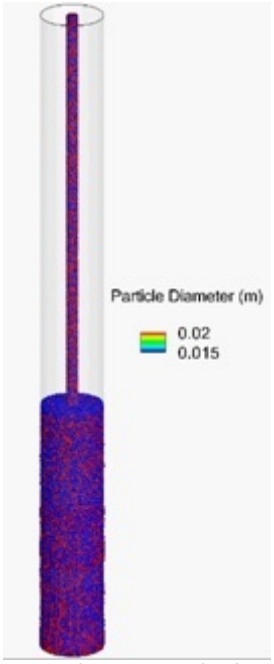

Figure 6.7: Pile simulation with discrete aggregates

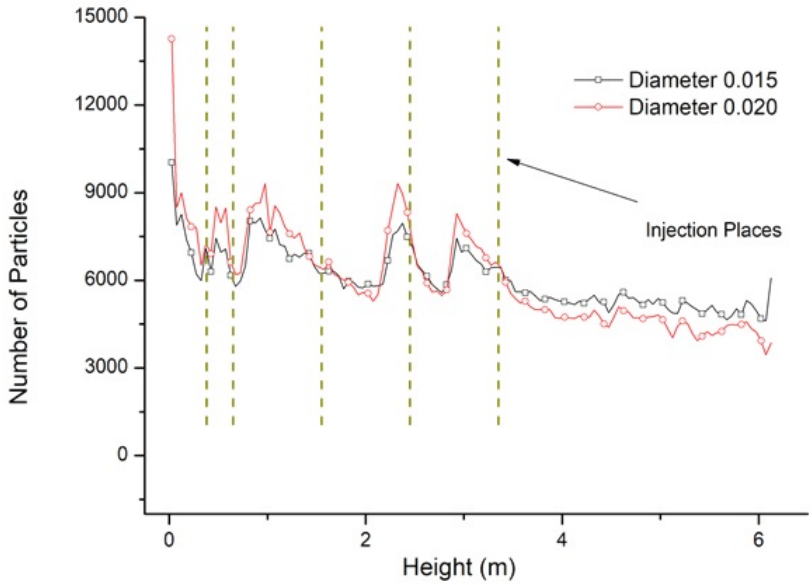

Figure 6.8: Number of particles vs height

## 6.3 CFD-DEM approach

In the previous section we used DPM to model concrete flow as a multiphase material. The mortar phase was modelled using the Bingham model we have often seen in this work while the aggregate phase was modelled used DPM. This added the needed sophistication in order to model segregation. Both static and dynamic segregation were demonstrated using this technique. However, the limitation of DPM is that it is physically inaccurate. This is because the continuous mortar

phase completely ignores the presence of the aggregates. Only forces are exchanged between the two phases. Also the interactions between the aggregates were ignored in the previous section. Although inter-particle interaction may not influence segregation as much, the blocking phenomenon cannot be modelled since blocking mechanisms depend on interlocking of particles. In this section, the CFD-DEM technique we have seen in Chapter 3 is applied to fresh concrete flow simulations. The governing equations we have seen in CFD-DEM consider the presence of particles in terms of volume fraction. The forces between the continuous and discrete phases are coupled using momentum exchange terms. Due to the collision detection algorithm, inter-particle interactions can be captured. CFD-DEM thus overcomes the limitations of DPM and can potentially model concrete flow with very high fidelity.

### 6.3.1 Outline of the technique

In this section, the CFD-DEM technique we have seen previously is configured and tailored to simulate fresh concrete flow. The CFD governing equations have already been introduced and will be used to model the mortar phase. The only modification required for this is the use of the Bingham model as the constitutive relationship. As we have seen, concrete flow modelling usually involves interaction with a second continuous phase such as bentonite fluid or air. This phase is also modelled using CFD. VOF is used to track the interface between the two phases. In CFD-DEM however, the phase indicator equation of the VOF has to be slightly modified to consider the volume fraction of the particulate phase. Similarly the CFD equations (3.1, 3.2) have to modified to include the VOF phase. The phase indicator equation solved in the VOF is [UI99]

$$\frac{\partial \alpha}{\partial t} + \nabla \cdot \alpha \mathbf{u} = 0 \tag{6.3}$$

where $\alpha$ is the indicator function for the primary phase. With the introduction of volume fraction of the particulate phase in the problem, this equation can be written as

$$\frac{\partial (\alpha \phi_{\mathrm{f}})}{\partial t} + \nabla \cdot \alpha \phi_{\mathrm{f}} \mathbf{u} = 0 \tag{6.4}$$

where $\phi_{\mathrm{f}}$ is the volume fraction of the continuum phases given by $1 - \phi_{\mathrm{s}}$ where $\phi_{\mathrm{s}}$ is the particulate volume fraction. Lastly, DEM is used to model the aggregate particles and track their motion. The governing equations for these are the same as those introduced in Chapter 3. The collision detection algorithm will ensure that inter-particle interaction is not ignored. In the next section, the use of CFD-DEM to model concrete flow is demonstrated.

### 6.3.2 Simulating the L-box test using CFD-DEM

We will now simulate the L-box test using the CFD-DEM approach which we have introduced above. The L-box test has been introduced in Chapter 5 and simulated using the homogeneous Bingham model. The same will be done here except that the

CFD-DEM approach will be used instead. To simplify the study, rebars have not been used in an attempt to reduce computational time. Aggregates of diameter $1cm$ have been used and initially distributed evenly in the concrete. The DEM properties of aggregates used are shown in Table 6.4.

Table 6.4: DEM properties of aggregates

| **Property** | **Value** |
|---|---|
| Diameter | $10mm$ |
| Density | $2750kg/m^3$ |
| Coefficient of restitution | 0.45 |
| Friction coefficient | 0.1 |

The properties used for the mortar phase are shown in Table 6.5. The secondary phase used is air and it is modelled as a regular Newtonian fluid. Standard CFD properties are used for air in the simulation. The time-step size used for the CFD solver is $0.001s$ while the time-step size for the DEM solver is $1E{-}6s$. The simulation is run till the concrete reaches a stable and settled configuration. The motion of the aggregates at different stages of the simulation is shown in Figure 6.9. The indicator function for the mortar phase at the various stages of the simulation on a cross-sectional plane through the centre of the L-box is shown in Figure 6.10. Similarly, the volume fraction of the aggregate phase on a cross-sectional plane through the centre of the L-box is shown in Figure 6.11.

Table 6.5: Properties of the mortar phase

| **Property** | **Value** |
|---|---|
| Density | $2162kg/m^3$ |
| Yield stress | $10Pa$ |
| Plastic viscosity | $8Pa.s$ |

From the results it can be seen that CFD-DEM technique can be used to simulate fresh concrete flow with extremely high fidelity. Information on the position of the aggregates is readily available. This enables us to plot the volume fraction occupied by the aggregates at any point. The data which can be extracted from the simulation far exceeds than the those obtained using the homogeneous Bingham approach. The CFD-DEM approach considers the presence of particles in the governing equations and is therefore physically more accurate than DPM. From Figure 6.11 it can be seen that there is a higher concentration of the aggregate phase at the left bottom corner of the box. The aggregates tend to get accumulated here since the concrete in this region does not move much. There is also a region near the gate where there is a lower concentration of aggregates. The concentration is also higher near the walls of the vertical section of the L-box and is especially high in the corners. The concrete in the middle region tends to flow faster leaving it less concentrated with aggregates. This highlights the potential of the CFD-DEM to predict defects in the placement process due to congestion or scarcity of aggregates in a particular region of the form-work. Blocking and segregation can be easily modelled using CFD-DEM.

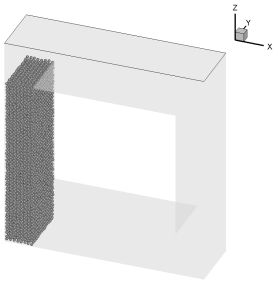

$0s$

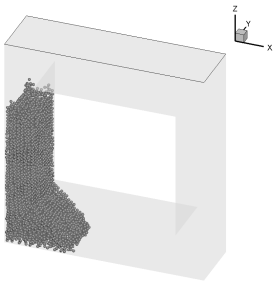

$0.25s$

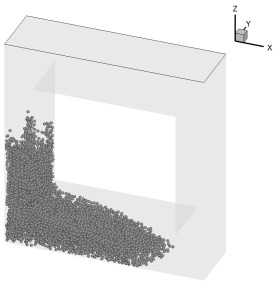

$0.5s$

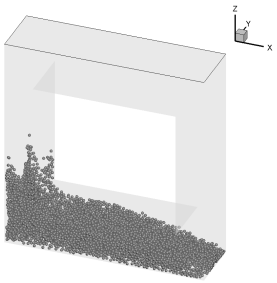

$0.75s$

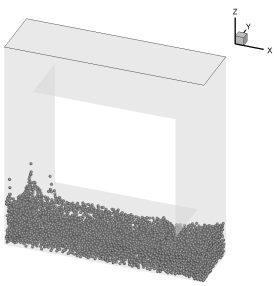

$1s$

Figure 6.9: Motion of aggregates in L-box simulation

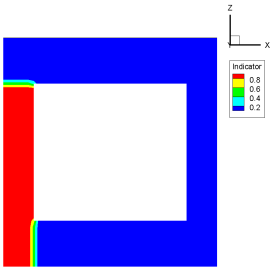


$0s$

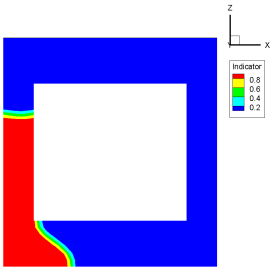


$0.25s$

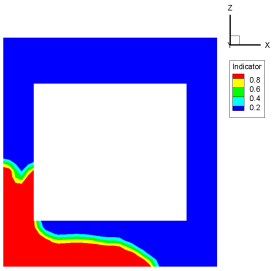


$0.5s$

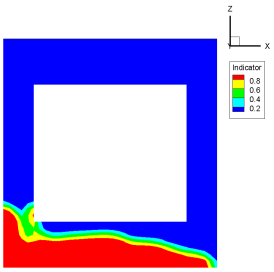


$0.75s$

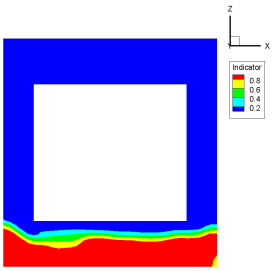


$1s$

Figure 6.10: Indicator function at various stages of the simulation

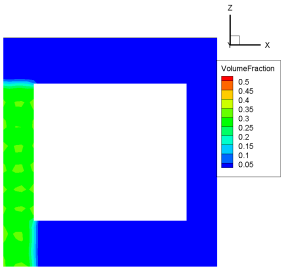


$0s$

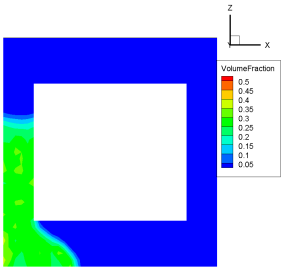


$0.25s$

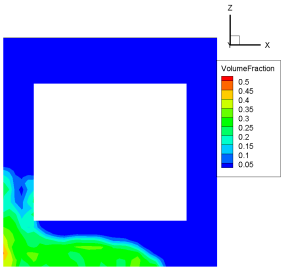


$0.5s$

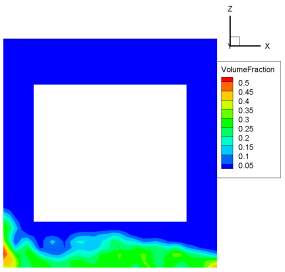


$0.75s$

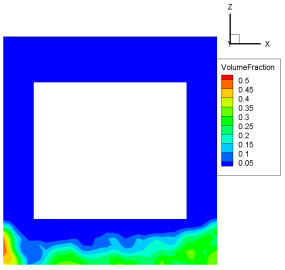


$1s$

Figure 6.11: Volume fraction of aggregate phase at various stages of the simulation

CFD-DEM is a powerful tool in the study of fresh concrete flow and needs to be studied in greater detail. By applying it to full-scale industrial problems, defect causing mechanisms can be investigated with high precision and potential methods to avoid the defects can be researched. CFD-DEM thus offers the industry the breakthrough it desperately needs to solve issues during concrete placement procedures.

## 6.4 Conclusion

The homogeneous Bingham fluid approach of modelling concrete flow has major limitations and is only useful where the bulk flow of concrete is to be simulated. To model major defect causing phenomena, more advance approaches are required. Also concrete rheology displays time dependant behaviour known as thixotropy. In this chapter a new model which modifies the Bingham model by adding two extra parameters to it was used to model thixotropy. DPM was applied to model the column segregation test and was able to model static segregation in unstable concrete mixes. It was then applied to the full-scale pile simulation seen in the previous chapter. Dynamic segregation was observed and demonstrated as a result. Although DPM is more advanced than the homogeneous Binhgam approach, it still suffers from a lack of accuracy due to the continuous phase ignoring the aggregate phase presence. The use of CFD-DEM is able to overcome that limitation and due to the collision detection algorithm, interaction between the aggregates can be captured as well. CFD-DEM was used to simulate the L-box test in this chapter and is a very powerful tool in the context of fresh concrete flow modelling research.

# Chapter 7

# Conclusions

Flows observed in nature and engineering applications rarely consist of a single homogeneous fluid. They usually consist of two or more distinct phases flowing simultaneously. Such flows in which the phases are separated at a scale well above the molecular level are termed as multiphase flows. Research on modelling multiphase flows continues to be of significance to several different industries including medicine, engineering and transportation. Although significant progress has been made on developing models and techniques to predict multiphase flow behaviour, there remains a lot to be wanted. Better accuracy, efficiency and stability will result in more efficient design, lower losses and most importantly safer end products.

In this work we have seen the various techniques to model multiphase flows which are available in literature. These techniques can be broadly classified into Eulerian-Eulerian and Eulerian-Lagrangian approaches. In Chapter 2, details on these methods were provided and their strengths and weaknesses were analysed. Each method was designed to cater to a certain range of applications the understanding of which is crucial in successfully simulating a given problem. The suitability of each of the methods was discussed in detail and formed the basis for the rest of the chapters.

In Chapter 3, a particular Eulerian-Lagrangian approach, namely, CFD-DEM was looked at more closely. This approach models the continuum phase using CFD and the discrete phase using DEM. Unlike Eulerian-Eulerian approaches, the position of particles can be tracked with accuracy and results in high fidelity simulations. The drag model plays an important role in CFD-DEM coupling and various such drag models exist in literature. The formulations differ greatly and a systematic analysis on their applicability is lacking. In the chapter, the performance of the models were compared to each other and results were benchmarked against a fully resolved FVM model. All models were found to be reasonably accurate for low Reynolds number flows. However, diverging results were observed when the Reynolds number increased beyond unity. Also in the chapter, a new benchmark experiment was proposed to complement the existing fluidised bed validation experiment. In this new experiment, CFD-DEM coupling for low Reynolds number flows is tested. The results obtained from simulations were found to be close to the ones obtained from the experiment.

In Chapter 4, a potential application of multiphase flow modelling, namely the

modelling of fresh concrete flow was reviewed. The underlying physics of concrete rheology was introduced. Concrete consists of different constituents which interact with each other in a complex manner to produce the rheological behaviours we observe. There exist industrial tests which attempt to provide a qualitative measure for these rheological parameters for any given concrete mix. Full-scale tests are expensive to conduct and are difficult to monitor and simulating fresh concrete flow is the only viable means of predicting its behaviour in a particular scenario. The Bingham model has been widely used in literature to simulate concrete flow but can only be used to describe the "bulk" flow. DEM, SPH, LBM, FEM and FVM have all been used in concrete flow numerical modelling and were critically reviewed in this chapter. In order to model more complex defect causing phenomena it was concluded that a more sophisticated model is necessary.

In Chapter 5, the Bingham model was used to simulate fresh concrete flow. Although the Bingham model is widely used in literature, obtaining actual values for the yield stress and plastic viscosity remains a challenge. In this chapter a novel method for obtaining the values was introduced. A parametric study was performed in order to obtain calibration curves which correlate flow diameter and flow time to the Bingham parameters. Thus by simply performing the slump flow and the V-funnel test on a fresh concrete mix, the flow diameter and flow time can be mapped to unique values for the Bingham parameters by using the calibration curves. This new method was shown to produce accurate results. Also the Bingham model was applied to a full-scale pile simulation and a case-study was performed. The simulations revealed the flow pattern of tremie concrete in piles and the manner in which it reaches its final configuration. This helped answer outstanding questions which the industry had in tremie concrete placement. It also revealed the limitations of the homogeneous Bingham approach which is incapable of modelling segregation and blocking.

In Chapter 6, more advanced modelling techniques were used to capture the more complex concrete behaviours. Thixotropy was modelled by using a formulation which modifies the Bingham model and adds two extra parameters to it. In a more advanced model, concrete was separated into a mortar and coarse aggregate phase. The mortar phase was described with the usual continuum Bingham approach while the aggregates were described using DPM. The potential of this method to model segregation was shown. Since in DPM particle-particle interaction and the volumetric presence of the discrete phase is ignored, in an even more sophisticated technique, DPM was replaced by DEM. The L-box test was simulated using this technique and its potential to capture effects of segregation and blocking were demonstrated.

## 7.1 Achievements and contributions

The broader goal of the thesis was to develop a method to model fresh concrete flow and capture all defect causing phenomena so that issues which the industry currently face can be resolved. The work in this thesis has contributed greatly to that cause and the main achievements can be summarised as follows:

1. Multiphase flow modelling techniques were introduced systematically and each of their advantages and disadvantages were clearly analysed. Their suitability for different scenarios and applications were established.

2. A comprehensive review was performed on the rheology of fresh concrete flow. The defects seen regularly in the industry and their causes were identified. The standard industrial tests were critically analysed. Existing numerical techniques to model fresh concrete flow available in literature were classified according to set criteria and critically discussed.

3. A novel method to determine yield stress and plastic viscosity was introduced and demonstrated to produce accurate results. The Bingham model was used to simulate the placement of tremie concrete in a full-scale pile. The flow pattern that the concrete follows in the pile was established and used to answer certain questions which the industry demanded.

4. A CFD-DEM framework was developed with the aim of applying it to fresh concrete flow. In the process the drag models were compared with each other and their performances were analysed. A new validation test was also developed to complement the already existing fluidised bed test.

5. The CFD-DEM framework was applied to simulate fresh concrete flow and its potential to model segregation and blocking was demonstrated. The modelling of thixotropy using a modification to the Bingham model was also demonstrated.

## 7.2 Future work

Although a lot was achieved towards fully modelling fresh concrete flow there are still many challenges that need to be overcome to completely reap the benefits of simulation technology in the construction industry. The CFD-DEM framework was developed to model segregation and blocking. It was used to simulate the L-box test, but further investigation is required and a systematic study needs to be performed in order to thoroughly demonstrate its potential. It also remains to be applied to a full-scale problem which would provide more insight into the issues faced by the industry. The framework needs to be improved so that large models can be simulated with reasonable speed. In this approach concrete was separated into only two phases, mortar and coarse aggregate. Defect causing phenomena such as bleeding cannot be modelled with this approach as it involves the interaction between cement and water. To model bleeding, the mortar phase would need to be further modelled as distinct cement, sand and water phases. Further, multiphase flow modelling could also be applied to other applications such as proppant transport in the oil and gas industry. Thus there is a lot of scope for research in the area of multiphase flow modelling and its applications in the industry.

# References


[ABL12] Habib Alehossein, Karsten Beckhaus, and Martin Larisch. Analysis of l-box test for tremie pipe concrete. *ACI Materials Journal-American Concrete Institute*, 109(3):303, 2012.

[AE13] Falah Alobaid and Bernd Epple. Improvement, validation and application of cfd/dem model to dense gas–solid flow in a fluidized bed. *Particuology*, 11(5):514–526, 2013.

[AK17] Benjamin Allen and Arshad Kudrolli. Depth resolved granular transport driven by shearing fluid flow. *Physical Review Fluids*, 2(2):024304, 2017.

[AKK17] Wajde S Alyhya, Sivakumar Kulasegaram, and Bhushan Lal Karihaloo. Simulation of the flow of self-compacting concrete in the v-funnel by sph. *Cement and Concrete Research*, 100:47–59, 2017.

[ARKK17] Muna AL-Rubaye, Sivakumar Kulasegaram, and Bhushan Lal Karihaloo. Simulation of self-compacting concrete in an l-box using smooth particle hydrodynamics. *Magazine of Concrete Research*, 69(12):618–628, 2017.

[AT17] Michael P Allen and Dominic J Tildesley. *Computer simulation of liquids*. Oxford university press, 2017.

[BB05] Christopher Earls Brennen and Christopher E Brennen. Fundamentals of multiphase flow. 2005.

[BBX+17] JH Bi, C Bao, D Xu, J Guan, and WX Cheng. Numerical simulation of the distribution and orientation of steel fibres in the scc. *Magazine of Concrete Research*, 69(16):811–822, 2017.

[Bea94] Denis Beaupre. *Rheology of high performance shotcrete*. PhD thesis, University of British Columbia, 1994.

[BF03] Lynn E Brower and Chiara F Ferraris. Comparison of concrete rheometers. *Concrete International*, 25(8):41–47, 2003.

[BGB10] Adrien Bouvet, Elhem Ghorbel, and Rachid Bennacer. The mini-conical slump flow test: Analysis and numerical study. *Cement and concrete research*, 40(10):1517–1523, 2010.

[BKK16a] Firas Badry, Sivakumar Kulasegaram, and Bhushan Lai Karihaloo. Estimation of the yield stress and distribution of large aggregates from slump flow test of self-compacting concrete mixes using smooth particle hydrodynamics simulation. *Journal of Sustainable Cement-Based Materials*, 5(3):117–134, 2016.

[BKK16b] Firas Badry, Sivakumar Kulasegaram, and Bhushan Lal Karihaloo. Effect of cone lift rate on the flow time of self-compacting concrete. *Magazine of Concrete Research*, 68(2):80–86, 2016.

[BPLH13] B Böhle, M Pulsfort, WR Linder, and U Hinzmann. Untersuchungen zum fließund ansteifverhalten von beton bei herstellung von bohrpfählen. *Vorträge zum*, 9:81–92, 2013.

[BSS11] Amir Hosein Bakhtiarian, Morteza Shokri, and Mohammad Reza Sabour. Application of self-compacting concrete, worldwide experiences. In *5th Symposium on Advances in Sciences and technology. Mashhad: Khavaran Higher-education Institute, Mashhad*, volume 12, 2011.

[BvdHK07] R Beetstra, Martin Anton van der Hoef, and JAM Kuipers. Drag force of intermediate reynolds number flow past mono-and bidisperse arrays of spheres. *AIChE journal*, 53(2):489–501, 2007.

[CDRDM10] Fernando Cello, Alberto Di Renzo, and Francesco Paolo Di Maio. A semi-empirical model for the drag force and fluid–particle interaction in polydisperse suspensions. *Chemical Engineering Science*, 65(10):3128–3139, 2010.

[CFFP10] Massimiliano Cremonesi, Liberato Ferrara, A Frangi, and Umberto Perego. Simulation of the flow of fresh cement suspensions by a lagrangian finite element approach. *Journal of Non-Newtonian Fluid Mechanics*, 165(23-24):1555–1563, 2010.

[CH05] SE Chidiac and F Habibbeigi. Modelling the rheological behaviour of fresh concrete: An elasto-viscoplastic finite element approach. *Computers and Concrete*, 2(2):97–110, 2005.

[CJLW17] Wei Cui, Tianzhu Ji, Ming Li, and Xinli Wu. Simulating the workability of fresh self-compacting concrete with random polyhedron aggregate based on dem. *Materials and Structures*, 50(1):92, 2017.

[CKK13] Myoung Sung Choi, Young Jin Kim, and Seung Hee Kwon. Prediction on pipe flow of pumped concrete based on shear-induced particle migration. *Cement and Concrete Research*, 52:216–224, 2013.

[CKK14] Myoung Sung Choi, Young Jin Kim, and Jin Keun Kim. Prediction of concrete pumping using various rheological models. *International Journal of Concrete Structures and Materials*, 8(4):269–278, 2014.

[CL17] Guodong Cao and Zhuguo Li. Numerical flow simulation of fresh concrete with viscous granular material model and smoothed particle hydrodynamics. *Cement and Concrete Research*, 100:263–274, 2017.

[CLX19] Guodong Cao, Zhuguo Li, and Zhisong Xu. A sph simulation method for opening flow of fresh concrete considering boundary restraint. *Construction and Building Materials*, 198:379–389, 2019.

[CM09] SE Chidiac and F Mahmoodzadeh. Plastic viscosity of fresh concrete–a critical review of predictions methods. *Cement and Concrete Composites*, 31(8):535–544, 2009.

[CMMH05] Matteo Chiesa, Vidar Mathiesen, Jens A Melheim, and Britt Halvorsen. Numerical simulation of particulate flow by the eulerian–lagrangian and the eulerian–eulerian approach with application to a fluidized bed. *Computers & chemical engineering*, 29(2):291–304, 2005.

[CPA96] Philippe Coussot, Sébastien Proust, and Christophe Ancey. Rheological interpretation of deposits of yield stress fluids. *Journal of Non-Newtonian Fluid Mechanics*, 66(1):55–70, 1996.

[CSOO17] Abram H Clark, Mark D Shattuck, Nicholas T Ouellette, and Corey S O'Hern. Role of grain dynamics in determining the onset of sediment transport. *Physical Review Fluids*, 2(3):034305, 2017.

[CST+98] Clayton Crowe, Martin Sommerfeld, Yutaka Tsuji, et al. *Multiphase flows with.* Ž, 1998.

[CWYV09] KW Chu, B Wang, AB Yu, and A Vince. Cfd-dem modelling of multiphase flow in dense medium cyclones. *Powder Technology*, 193(3):235–247, 2009.

[CY08] KW Chu and AB Yu. Numerical simulation of complex particle–fluid flows. *Powder Technology*, 179(3):104–114, 2008.

[CYSW18] Wei Cui, Wei-shuo Yan, Hui-fang Song, and Xin-li Wu. Blocking analysis of fresh self-compacting concrete based on the dem. *Construction and Building Materials*, 168:412–421, 2018.

[CZT+15] Guodong Cao, Hao Zhang, Yuanqiang Tan, Jiaqian Wang, Rong Deng, Xiangwu Xiao, and Binxing Wu. Study on the effect of coarse aggregate volume fraction on the flow behavior of fresh concrete via dem. *Procedia engineering*, 102:1820–1826, 2015.

[DAVdHK07] NG Deen, M Van Sint Annaland, Martin Anton Van der Hoef, and JAM Kuipers. Review of discrete particle modeling of fluidized beds. *Chemical engineering science*, 62(1-2):28–44, 2007.

[DF94] R Di Felice. The voidage function for fluid-particle interaction systems. *International Journal of Multiphase Flow*, 20(1):153–159, 1994.

[DKK14a] R Deeb, S Kulasegaram, and BL Karihaloo. 3d modelling of the flow of self-compacting concrete with or without steel fibres. part i: slump flow test. *Computational Particle Mechanics*, 1(4):373–389, 2014.

[DKK14b] Rola Deeb, Bhushan L Karihaloo, and Sivakumar Kulasegaram. Reorientation of short steel fibres during the flow of self-compacting concrete mix and determination of the fibre orientation factor. *Cement and Concrete Research*, 56:112–120, 2014.

[DKK14c] Rola Deeb, Sivakumar Kulasegaram, and Bhushan Lai Karihaloo. 3d modelling of the flow of self-compacting concrete with or without steel fibres. part ii: L-box test and the assessment of fibre reorientation during the flow. *Computational Particle Mechanics*, 1(4):391–408, 2014.

[DKK16] MS Abo Dhaheer, Sivakumar Kulasegaram, and Bhushan Lal Karihaloo. Simulation of self-compacting concrete flow in the j-ring test using smoothed particle hydrodynamics (sph). *Cement and Concrete Research*, 89:27–34, 2016.

[DLHS+97] F De Larrard, C Hu, T Sedran, JC Szitkar, M Joly, F Claux, and F Derkx. A new rheometer for soft-to-fluid fresh concrete. *Materials Journal*, 94(3):234–243, 1997.

[dLR11] François de Larrard and Nicolas Roussel. Flow simulation of fresh concrete under a slipform machine. *Road materials and pavement design*, 12(3):547–566, 2011.

[Dom98] P Domone. The slump flow test for high-workability concrete. *Cement and Concrete Research*, 28(2):177–182, 1998.

[DP99] Donald A Drew and Stephen L Passman. Relation of microstructure to constitutive equations. In *Theory of Multicomponent Fluids*, pages 153–192. Springer, 1999.

[DPC05] Frédéric Dufour and Gilles Pijaudier-Cabot. Numerical modelling of concrete flow: homogeneous approach. *International journal for numerical and analytical methods in geomechanics*, 29(4):395–416, 2005.

[DRDM07] Alberto Di Renzo and Francesco Paolo Di Maio. Homogeneous and bubbling fluidization regimes in dem–cfd simulations: hydrodynamic stability of gas and liquid fluidized beds. *Chemical Engineering Science*, 62(1-2):116–130, 2007.

[ECRKA17] K El Cheikh, S Rémond, N Khalil, and G Aouad. Numerical and experimental studies of aggregate blocking in mortar extrusion. *Construction and Building Materials*, 145:452–463, 2017.

[ED18] EFFC and DFI. *EFFC/DFI Concrete Task Group: Best Practice guide to Tremie Concrete for Deep Foundaitons*. 2018.

[EO49] Sabri Ergun and Ao Ao Orning. Fluid flow through randomly packed columns and fluidized beds. *Industrial & Engineering Chemistry*, 41(6):1179–1184, 1949.

[Esp07] Oskar Esping. Early age properties of self-compacting concrete. *Effects of fine aggregate and limestone filler Ph. D. Sweden: Chalmers University of Technology*, 2007.

[F+11] ANSYS Fluent et al. Ansys fluent theory guide. *ANSYS Inc., USA*, 15317:724–746, 2011.

[Far68] RJ Farris. Prediction of the viscosity of multimodal suspensions from unimodal viscosity data. *Transactions of the Society of Rheology*, 12(2):281–301, 1968.

[FCT+12] Liberato Ferrara, Massimiliano Cremonesi, Nathan Tregger, Attilio Frangi, and Surendra P Shah. On the identification of rheological properties of cement suspensions: Rheometry, computational fluid dynamics modeling and field test measurements. *Cement and concrete research*, 42(8):1134–1146, 2012.

[FD98] Chiara F Ferraris and Francois DeLarrard. Testing and modeling of fresh concrete rheology. 1998.

[FGMM07] Chiara F Ferraris, Mette Geiker, Nicos S Martys, and Nicholas Muzzatti. Parallel-plate rheometer calibration using oil and computer simulation. *Journal of Advanced Concrete Technology*, 5(3):363–371, 2007.

[FLT+15] YT Feng, Xikui Li, Yuanqiang Tan, Shunying Ji, Rong Deng, Hao Zhang, and Shengqiang Jiang. Numerical study of concrete mixing transport process and mixing mechanism of truck mixer. *Engineering Computations*, 2015.

[FPS02] Joel H Ferziger, Milovan Perić, and Robert L Street. *Computational methods for fluid dynamics*, volume 3. Springer, 2002.

[FXZ+04] YQ Feng, BH Xu, SJ Zhang, AB Yu, and P Zulli. Discrete particle simulation of gas fluidization of particle mixtures. *AIChE Journal*, 50(8):1713–1728, 2004.

[GDM19] Vladislav Gudžulić, Thai Son Dang, and Günther Meschke. Computational modeling of fiber flow during casting of fresh concrete. *Computational Mechanics*, 63(6):1111–1129, 2019.

[GGS82] UKNG Ghia, Kirti N Ghia, and CT Shin. High-re solutions for incompressible flow using the navier-stokes equations and a multigrid method. *Journal of computational physics*, 48(3):387–411, 1982.

[GGT+98] D Gera, M Gautam, Y Tsuji, T Kawaguchi, and T Tanaka. Computer simulation of bubbles in large-particle fluidized beds. *Powder Technology*, 98(1):38–47, 1998.

[Gil01] LG Gilbilaro. Fluidization-dynamics: The formulation and applications of a predictive theory for the fluidized state, 2001.

[GKD+12] Christoph Goniva, Christoph Kloss, Niels G Deen, Johannes AM Kuipers, and Stefan Pirker. Influence of rolling friction on single spout fluidized bed simulation. *Particuology*, 10(5):582–591, 2012.

[GS11] Annika Gram and Johan Silfwerbrand. Numerical simulation of fresh scc flow: applications. *Materials and Structures*, 44(4):805–813, 2011.

[GSL14] Annika Gram, Johan Silfwerbrand, and Björn Lagerblad. Obtaining rheological parameters from flow testanalytical, computational and lab test approach. *Cement and concrete research*, 63:29–34, 2014.

[GYSF10] Zhan-Qi Guo, Quan Yuan, P Stroeven, and ALA Fraaij. Discrete element method simulating workability of fresh concrete. In *AIP Conference Proceedings*, volume 1233, pages 430–435. American Institute of Physics, 2010.

[HDLG95] Chong Hu, François De Larrard, and Odd E Gjørv. Rheological testing and modelling of fresh high performance concrete. *Materials and Structures*, 28(1):1, 1995.

[Hey19] Joris Heyman. Tractrac: A fast multi-object tracking algorithm for motion estimation. *Computers & Geosciences*, 128:11–18, 2019.

[HK12a] Hooman Hoornahad and Eduard AB Koenders. Simulation of the slump test based on the discrete element method (dem). In *Advanced Materials Research*, volume 446, pages 3766–3773. Trans Tech Publ, 2012.

[HK12b] Hooman Hoornahad and Eduard AB Koenders. Tracking the rheological behavior change of a fresh granular-cement paste material to a granular material based on dem. In *Advanced Materials Research*, volume 446, pages 3803–3809. Trans Tech Publ, 2012.

[HK14] Hooman Hoornahad and Eduard AB Koenders. Modelling rheological behavior of fresh cement-sand mixtures. In *International Conference on Offshore Mechanics and Arctic Engineering*, volume 45455, page V005T11A029. American Society of Mechanical Engineers, 2014.

[HKBvS96] BPB Hoomans, JAM Kuipers, Willem J Briels, and Willibrordus Petrus Maria van Swaaij. Discrete particle simulation of bubble and slug formation in a two-dimensional gas-fluidised bed: a hard-sphere approach. *Chemical Engineering Science*, 51(1):99–118, 1996.

[HKvB11] H Hoornahad, Eddy AB Koenders, and Klaas van Breugel. Towards a model for fresh granular-paste systems based on discrete element method. In *Key Engineering Materials*, volume 452, pages 569–572. Trans Tech Publ, 2011.

[HKY17a] Masoud Hosseinpoor, Kamal H Khayat, and Ammar Yahia. Numerical simulation of self-consolidating concrete flow as a heterogeneous material in l-box set-up: coupled effect of reinforcing bars and aggregate content on flow characteristics. *Materials and Structures*, 50(2):163, 2017.

[HKY17b] Masoud Hosseinpoor, Kamal H Khayat, and Ammar Yahia. Numerical simulation of self-consolidating concrete flow as a heterogeneous material in l-box set-up: Effect of rheological parameters on flow performance. *Cement and Concrete Composites*, 83:290–307, 2017.

[HL89] A Haider and O Levenspiel. Drag coefficient and terminal velocity of spherical and nonspherical particles. *Powder technology*, 58(1):63–70, 1989.

[HN81] Cyril W Hirt and Billy D Nichols. Volume of fluid (vof) method for the dynamics of free boundaries. *Journal of computational physics*, 39(1):201–225, 1981.

[HODJ15] Morgane Houssais, Carlos P Ortiz, Douglas J Durian, and Douglas J Jerolmack. Onset of sediment transport is a continuous transition driven by fluid shear and granular creep. *Nature communications*, 6:6527, 2015.

[HODJ16] Morgane Houssais, Carlos P Ortiz, Douglas J Durian, and Douglas J Jerolmack. Rheology of sediment transported by a laminar flow. *Physical Review E*, 94(6):062609, 2016.

[HSPC15] Huan He, Piet Stroeven, Eric Pirard, and Luc Courard. On the shape simulation of aggregate and cement particles in a dem system. *Advances in Materials Science and Engineering*, 2015, 2015.

[HYK19] Masoud Hosseinpoor, Ammar Yahia, and Kamal H Khayat. Modeling of flow performance of self-consolidating concrete using dam break theory and computational fluid dynamics. *Cement and Concrete Composites*, 102:14–27, 2019.

[IH10] Mamoru Ishii and Takashi Hibiki. *Thermo-fluid dynamics of two-phase flow*. Springer Science & Business Media, 2010.

[Ish90] Mamoru Ishii. Two-fluid model for two-phase flow. *Multiphase science and technology*, 5(1-4), 1990.

[KÇY+18] Cenk Karakurt, Ahmet Ozan Çelik, Cem Yılmazer, Volkan Kiriççi, and Ethem Özyaşar. Cfd simulations of self-compacting concrete with discrete phase modeling. *Construction and Building Materials*, 186:20–30, 2018.

[KGH+12] Christoph Kloss, Christoph Goniva, Alice Hager, Stefan Amberger, and Stefan Pirker. Models, algorithms and validation for opensource dem and cfd–dem. *Progress in Computational Fluid Dynamics, an International Journal*, 12(2-3):140–152, 2012.

[KH01] Donald L Koch and Reghan J Hill. Inertial effects in suspension and porous-media flows. *Annual Review of Fluid Mechanics*, 33(1):619–647, 2001.

[KHMF97] Takeshi Kokado, Takashi Hosoda, Toyoaki Miyagawa, and Manabu Fujii. Study on a method of evaluating a yield value of fresh concrete with a slump flow value. *Doboku Gakkai Ronbunshu*, 1997(578):19–29, 1997.

[KK05] Nikolay Ivanov Kolev and NI Kolev. *Multiphase flow dynamics*, volume 1. Springer, 2005.

[KKG11] Sivakumar Kulasegaram, Bhushan Lal Karihaloo, and Akbar Ghanbari. Modelling the flow of self-compacting concrete. *International Journal for Numerical and Analytical Methods in Geomechanics*, 35(6):713–723, 2011.

[KPT15] F Kolařík, B Patzák, and LN Thrane. Modeling of fiber orientation in viscous fluid flow with application to self-compacting concrete. *Computers & Structures*, 154:91–100, 2015.

[KPZ16] F Kolařík, B Patzák, and J Zeman. Numerical modeling of fresh concrete flow through porous medium. In *AIP Conference Proceedings*, volume 1738, page 480047. AIP Publishing LLC, 2016.

[KPZ18] Filip Kolařík, Bořek Patzák, and Jan Zeman. Computational homogenization of fresh concrete flow around reinforcing bars. *Computers & Structures*, 207:37–49, 2018.

[LCDK05] JM Link, LA Cuypers, NG Deen, and JAM Kuipers. Flow regimes in a spout–fluid bed: A combined experimental and simulation study. *Chemical Engineering Science*, 60(13):3425–3442, 2005.

[LCG18] Zhuguo Li, Guodong Cao, and Kun Guo. Numerical method for thixotropic behavior of fresh concrete. *Construction and Building Materials*, 187:931–941, 2018.

[LCHP13] Hadi Lashkarbolouk, Mohammad R Chamani, Amir M Halabian, and Ahmad R Pishehvar. Viscosity evaluation of scc based on flow simulation in the l-box test. *Magazine of concrete research*, 65(6):365–376, 2013.

[LCT16] Zhuguo Li, Guodong Cao, and Yuanqiang Tan. Prediction of time-dependent flow behaviors of fresh concrete. *Construction and Building Materials*, 125:510–519, 2016.

[LD88] RT Lahey and DA Drew. The three-dimensional time and volume averaged conservation equations of two-phase flow. In *Advances in nuclear science and technology*, pages 1–69. Springer, 1988.

[LHC14] Hadi Lashkarbolouk, Amir M Halabian, and Mohammad R Chamani. Simulation of concrete flow in v-funnel test and the proper range of viscosity and yield stress for scc. *Materials and structures*, 47(10):1729–1743, 2014.

[Li11] Zongjin Li. *Advanced concrete technology*. John Wiley & Sons, 2011.

[Li15] Z Li. Rheological model and rheometer of fresh concrete. *Journal of Structural and Construction Engineering, Transaction of Archcitectural Institstue of Japan*, 80(710):527–537, 2015.

[LL10] MB Liu and GR Liu. Smoothed particle hydrodynamics (sph): an overview and recent developments. *Archives of computational methods in engineering*, 17(1):25–76, 2010.

[LMLB17] Liqiang Lu, Aaron Morris, Tingwen Li, and Sofiane Benyahia. Extension of a coarse grained particle method to simulate heat transfer in fluidized beds. *International Journal of Heat and Mass Transfer*, 111:723–735, 2017.

[LSCT07] P Laure, L Silva, T Coupez, and F Toussaint. Numerical modelling of concrete flow with rigid fibers. In *AIP Conference Proceedings*, volume 907, pages 1390–1395. American Institute of Physics, 2007.

[Lud08] Stefan Luding. Introduction to discrete element methods: basic of contact force models and how to perform the micro-macro transition to continuum theory. *European Journal of Environmental and Civil Engineering*, 12(7-8):785–826, 2008.

[MB15] Jack C McCormac and Russell H Brown. *Design of reinforced concrete*. John Wiley & Sons, 2015.

[MF02] Nicos Martys and Chiara F Ferraris. Simulation of scc flow. In *Proc. 1st North American Conf. On the Design and Use of Self-Consolidating Concrete, Chicago, IL*, pages 27–30. Citeseer, 2002.

[MGK+14] Viktor Mechtcherine, Annika Gram, Knut Krenzer, Jörg-Henry Schwabe, Sergiy Shyshko, and Nicolas Roussel. Simulation of fresh concrete flow using discrete element method (dem): theory and applications. *Materials and structures*, 47(4):615–630, 2014.

[MK92] Jiro Murata and HirojiII Kukawa. Viscosity equation for fresh concrete. *Materials Journal*, 89(3):230–237, 1992.

[MMD+16] F Moukalled, L Mangani, M Darwish, et al. The finite volume method in computational fluid dynamics. *An advanced introduction with OpenFoam® and Matlab®. Nueva York: Springer. Recuperado de http://www. gidropraktikum. narod. ru/Moukalled-et-al-FVM-OpenFOAM-Matlab. pdf*, 2016.

[MS15] Viktor Mechtcherine and Sergiy Shyshko. Simulating the behaviour of fresh concrete with the distinct element method–deriving model parameters related to the yield stress. *Cement and Concrete Composites*, 55:81–90, 2015.

[MT90] H Mori and Y Tanigawa. Flow simulation of fresh concrete subjected to vibration. *Magazine of Concrete Research*, 42(153):223–232, 1990.

[MTK96] Mikko Manninen, Veikko Taivassalo, and Sirpa Kallio. On the mixture model for multiphase flow. 1996.

[Mur84] J Murata. Flow and deformation of fresh concrete. *Materiaux et Construction*, 17(2):117–129, 1984.

[Nev95] Adam M Neville. *Properties of concrete*, volume 4. Longman London, 1995.

[NGF+16] V Nerella, Filippo Galvani, Liberato Ferrara, Viktor Mechtcherine, et al. Normal and tangential interaction between discrete particles immersed in viscoelastic fluids: Experimental investigation as basis for discrete element modelling of fresh concrete. In *8th International RILEM Symposium on Self-Compacting Concrete*, pages 171–181, 2016.

[NPK+10] Marina K-A Neophytou, Stella Pourgouri, Antonios D Kanellopoulos, Michael F Petrou, Ioannis Ioannou, Georgios Georgiou, and Andreas Alexandrou. Determination of the rheological parameters of self-compacting concrete matrix using slump flow test. *Applied Rheology*, 20(6), 2010.

[NRG+06] VH Nguyen, S Rémond, JL Gallias, JP Bigas, and P Muller. Flow of herschel–bulkley fluids through the marsh cone. *Journal of non-newtonian fluid mechanics*, 139(1-2):128–134, 2006.

[NU99] Munaz Ahmed Noor and Taketo Uomoto. Three-dimensional discrete element simulation of rheology tests of self-compacting concrete. In

*Self-compacting concrete (Stockholm, 13-14 September 1999)*, pages 35–46, 1999.

[NZSGM16] Hamid Reza Norouzi, Reza Zarghami, Rahmat Sotudeh-Gharebagh, and Navid Mostoufi. *Coupled CFD-DEM modeling: formulation, implementation and application to multiphase flows*. John Wiley & Sons, 2016.

[OOO00] H Okamura, K Ozawa, and M Ouchi. Self-compacting concrete. *Structural concrete*, 1(1):3–17, 2000.

[PB09] B Patzák and Z Bittnar. Modeling of fresh concrete flow. *Computers & structures*, 87(15-16):962–969, 2009.

[PCA16] Ricardo Pieralisi, SHP Cavalaro, and A Aguado. Discrete element modelling of the fresh state behavior of pervious concrete. *Cement and Concrete Research*, 90:6–18, 2016.

[PT09] Andrea Prosperetti and Grétar Tryggvason. *Computational methods for multiphase flow*. Cambridge university press, 2009.

[PU99] UC Puri and T Uomoto. Numerical modelinga new tool for understanding shotcrete. *Materials and Structures*, 32(4):266–272, 1999.

[PU02] UC Puri and T Uomoto. Characterization of distinct element modeling parameters for fresh concrete and its application in shotcrete simulations. *Journal of materials in civil engineering*, 14(2):137–144, 2002.

[PW01] Eric Perkins and John R Williams. A fast contact detection algorithm insensitive to object sizes. *Engineering Computations*, 18(1/2):48–62, 2001.

[QH18] Liu-Chao Qiu and Yu Han. 3d simulation of self-compacting concrete flow based on mrt-lbm. *Advances in Materials Science and Engineering*, 2018, 2018.

[RC05] N Roussel and Ph Coussot. fifty-cent rheometer for yield stress measurements: from slump to spreading flow. *Journal of rheology*, 49(3):705–718, 2005.

[RG14] Nicolas Roussel and Annika Gram. Simulation of fresh concrete flow. *RILEM State-of-the-Art Reports*, 15, 2014.

[RGC+16] Nicolas Roussel, Annika Gram, Massimiliano Cremonesi, Liberato Ferrara, Knut Krenzer, Viktor Mechtcherine, Sergiy Shyshko, Jan Skocec, Jon Spangenberg, Oldrich Svec, et al. Numerical simulations of concrete flow: A benchmark comparison. *Cement and Concrete Research*, 79:265–271, 2016.

[RGD+07] Nicolas Roussel, Mette R Geiker, Frédéric Dufour, Lars N Thrane, and Peter Szabo. Computational modeling of concrete flow: general overview. *Cement and Concrete research*, 37(9):1298–1307, 2007.

[RLFC10] Nicolas Roussel, Anael Lemaître, Robert J Flatt, and Philippe Coussot. Steady state flow of cement suspensions: A micromechanical state of the art. *Cement and Concrete Research*, 40(1):77–84, 2010.

[RLR05] Nicolas Roussel and Robert Le Roy. The marsh cone: a test or a rheological apparatus? *Cement and concrete research*, 35(5):823–830, 2005.

[Rou06a] Nicolas Roussel. Correlation between yield stress and slump: comparison between numerical simulations and concrete rheometers results. *Materials and structures*, 39(4):501, 2006.

[Rou06b] Nicolas Roussel. A thixotropy model for fresh fluid concretes: theory, validation and applications. *Cement and concrete research*, 36(10):1797–1806, 2006.

[Rou07] Nicolas Roussel. The lcpc box: a cheap and simple technique for yield stress measurements of scc. *Materials and structures*, 40(9):889–896, 2007.

[RP14] Sebastien Remond and Patrick Pizette. A dem hard-core soft-shell model for the simulation of concrete flow. *Cement and concrete research*, 58:169–178, 2014.

[SAR13] A Sellountou, C Alvarez, and F Rausche. Thermal integrity profiling: A recent technological advancement in integrity evaluation of concrete piles. In *Proceedings from the First International Conference, Seminar on Deep Foundations*, 2013.

[Sch33] L Schiller. A drag coefficient correlation. *Zeit. Ver. Deutsch. Ing.*, 77:318–320, 1933.

[SKH17] Tae Yong Shin, Jae Hong Kim, and Seong Ho Han. Rheological properties considering the effect of aggregates on concrete slump flow. *Materials and Structures*, 50(6):239, 2017.

[SM10] S Shyshko and V Mechtcherine. Simulating fresh concrete behaviour–establishing a link between the bingham model and parameters of a dem-based numerical model. *HetMat–Modelling of Heteroginous Materials. RILEM Proceedings PRO*, 76:211–219, 2010.

[SM13] Sergiy Shyshko and Viktor Mechtcherine. Developing a discrete element model for simulating fresh concrete: Experimental investigation and modelling of interactions between discrete aggregate particles with fine mortar between them. *Construction and Building Materials*, 47:601–615, 2013.

[SRH+12] Jon Spangenberg, N Roussel, JH Hattel, H Stang, J Skocek, and MR Geiker. Flow induced particle migration in fresh concrete: Theoretical frame, numerical simulations and experimental results on model fluids. *Cement and Concrete Research*, 42(4):633–641, 2012.

[SSL09] Lin Shen, Leslie Struble, and David Lange. Modeling static segregation of self-consolidating concrete. *ACI Materials Journal*, 106(4):367, 2009.

[SSS+11] Oldrich Svec, Jan Skocek, Henrik Stang, John Forbes Olesen, and Peter Noe Poulsen. Flow simulation of fiber reinforced self compacting concrete using lattice boltzmann method. In *8th International Congress on the Chemistry of Cement*, 2011.

[ST58] Philip Geoffrey Saffman and Geoffrey Ingram Taylor. The penetration of a fluid into a porous medium or hele-shaw cell containing a more viscous liquid. *Proceedings of the Royal Society of London. Series A. Mathematical and Physical Sciences*, 245(1242):312–329, 1958.

[Sun16] Baojiang Sun. *Multiphase Flow in Oil and Gas Well Drilling*. John Wiley & Sons, 2016.

[Svá08] Petr Sváček. On approximation of non-newtonian fluid flow by the finite element method. *Journal of computational and applied mathematics*, 218(1):167–174, 2008.

[SY] Chenfeng Li Sizeng You, Ashutosh Bhokare. Parametric study. *Engineering computations*.

[Tat91] Geoffrey Howarth Tattersall. *Workability and quality control of concrete*. CRC Press, 1991.

[TB79] GH Tattersall and SJ Bloomer. Further development of the two-point test for workability and extension of its range. *Magazine of concrete research*, 31(109):202–210, 1979.

[TC87] R Turton and NN Clark. An explicit relationship to predict spherical particle terminal velocity. *Powder Technology*, 53(2):127–129, 1987.

[TDST+15] Serge Tichko, Geert De Schutter, Peter Troch, Jan Vierendeels, Ronny Verhoeven, Karel Lesage, and Niki Cauberg. Influence of the viscosity of self-compacting concrete and the presence of rebars on the formwork pressure while filling bottom-up. *Engineering Structures*, 101:698–714, 2015.

[TFS08] Nathan Tregger, Liberato Ferrara, and Surendra P Shah. Identifying viscosity of cement paste from mini-slump-flow test. *ACI Materials Journal*, 105(6):558, 2008.

[TKT93] Yutaka Tsuji, Toshihiro Kawaguchi, and Toshitsugu Tanaka. Discrete particle simulation of two-dimensional fluidized bed. *Powder technology*, 77(1):79–87, 1993.

[TLZ19] Hai Tran Thanh, Jianchun Li, and YX Zhang. Numerical modelling of the flow of self-consolidating engineered cementitious composites using smoothed particle hydrodynamics. *Construction and Building Materials*, 211:109–119, 2019.

[TM89] Yasuo Tanigawa and Hiroshi Mori. Analytical study on deformation of fresh concrete. *Journal of Engineering Mechanics*, 115(3):493–508, 1989.

[TMW90a] Y Tanigawa, H Mori, and K Watanabe. Analytical study on flow of fresh concrete by suspension element method. In *Proceedings of RILEM Colloquium on Properties of Fresh Concrete, Hanover*, pages 3–5, 1990.

[TMW90b] Y Tanigawa, H Mori, and K Watanabe. Computer simulation of consistency and rheology tests of fresh concrete by viscoplastic, prop. fresh concr. In *Proc. Colloq*, pages 301–308. Chapman & Hall Publ, 1990.

[TSG+04] Lars Nyholm Thrane, Peter Szabo, Mette Geiker, Mette Glavind, and Henrik Stang. Simulation of the test method l-box for self-compacting concrete. *Annual Transactions of the NORDIC rheology society*, 12(1):47–54, 2004.

[TSZ11] Grétar Tryggvason, Ruben Scardovelli, and Stéphane Zaleski. *Direct numerical simulations of gas–liquid multiphase flows*. Cambridge University Press, 2011.

[TVDMV+10] Serge Tichko, Jens Van De Maele, Niels Vanmassenhove, Geert De Schutter, Jan Vierendeels, Ronny Verhoeven, and Peter Troch. Numerical modelling of the filling of formworks with self-compacting concrete. *WIT Transactions on Engineering Sciences*, 69:157–168, 2010.

[TVDMV+14] Serge Tichko, Jens Van De Maele, Niels Vanmassenhove, Geert De Schutter, Jan Vierendeels, Ronny Verhoeven, and Peter Troch. Numerical simulation of formwork pressure while pumping self-compacting concrete bottom-up. *Engineering structures*, 70:218–233, 2014.

[UI99] O Ubbink and RI Issa. A method for capturing sharp fluid interfaces on arbitrary meshes. *Journal of computational physics*, 153(1):26–50, 1999.

[VBVDD+11] Maureen S Van Buijtenen, Willem-Jan Van Dijk, Niels G Deen, JAM Kuipers, T Leadbeater, and DJ Parker. Numerical and experimental study on multiple-spout fluidized beds. *Chemical engineering science*, 66(11):2368–2376, 2011.

[VM07] Henk Kaarle Versteeg and Weeratunge Malalasekera. *An introduction to computational fluid dynamics: the finite volume method*. Pearson education, 2007.

[VMKR11] Ksenija Vasilic, Birgit Meng, Hans-Carsten Kühne, and Nicolas Roussel. Flow of fresh concrete through steel bars: A porous medium analogy. *Cement and Concrete Research*, 41(5):496–503, 2011.

[VRMK10] Ksenija Vasilic, Nicolas Roussel, Birgit Meng, and Hans-Carsten Kühne. Computational modeling of scc flow through reinforced sections. In *Design, Production and Placement of Self-Consolidating Concrete*, pages 187–195. Springer, 2010.

[VSK+16] Ksenija Vasilic, Wolfram Schmidt, Hans-Carsten Kühne, Frank Haamkens, V Mechtcherine, and N Roussel. Flow of fresh concrete through reinforced elements: experimental validation of the porous analogy numerical method. *Cement and Concrete Research*, 88:1–6, 2016.

[Wac07] Anthony Wachs. Numerical simulation of steady bingham flow through an eccentric annular cross-section by distributed lagrange multiplier/fictitious domain and augmented lagrangian methods. *Journal of non-newtonian fluid mechanics*, 142(1-3):183–198, 2007.

[Wen66] C Yu Wen. Mechanics of fluidization. In *Chem. Eng. Prog., Symp. Ser.*, volume 62, pages 100–111, 1966.

[WGY+18] Hao Wu, Nan Gui, Xingtuan Yang, Jiyuan Tu, and Shengyao Jiang. A smoothed void fraction method for cfd-dem simulation of packed pebble beds with particle thermal radiation. *International Journal of Heat and Mass Transfer*, 118:275–288, 2018.

[WHY+17] Weiwei Wu, Xiaodiao Huang, Hong Yuan, Fei Xu, and Jingtao Ma. A modified lattice boltzmann method for herschel-bulkley fluids. *Rheologica Acta*, 56(4):369–376, 2017.

[WLXD16] Jun Wu, Xuemei Liu, Haihua Xu, and Hongjian Du. Simulation on the self-compacting concrete by an enhanced lagrangian particle method. *Advances in Materials Science and Engineering*, 2016, 2016.

[WO95] John R Williams and Ruaidhri OConnor. A linear complexity intersection algorithm for discrete element simulation of arbitrary geometries. *Engineering computations*, 12(2):185–201, 1995.

[WPC04] John R Williams, Eric Perkins, and Ben Cook. A contact algorithm for partitioning n arbitrary sized objects. *Engineering Computations*, 21(2/3/4):235–248, 2004.

[XY97] BH Xu and AB Yu. Numerical simulation of the gas-solid flow in a fluidized bed by combining discrete particle method with computational fluid dynamics. *Chemical Engineering Science*, 52(16):2785–2809, 1997.

[XYCZ00] BH Xu, AB Yu, SJ Chew, and P Zulli. Numerical simulation of the gas–solid flow in a bed with lateral gas blasting. *Powder Technology*, 109(1-3):13–26, 2000.

[YG11] Quan Yuan and Zhan Qi Guo. Ellipse particle modeling for fresh concrete and dynamic simulation of slump test. In *Advanced Materials Research*, volume 168, pages 746–750. Trans Tech Publ, 2011.

[YT19] Guan Heng Yeoh and Jiyuan Tu. *Computational techniques for multiphase flows*. Butterworth-Heinemann, 2019.

[ZAW15] Jingwei Zheng, Xuehui An, and Qiong Wu. Numerical pressure threshold method to simulate cement paste slump flow. *Materials and Structures*, 48(7):2063–2081, 2015.

[ZKCY10] ZY Zhou, SB Kuang, KW Chu, and AB Yu. Discrete particle simulation of particle–fluid flow: model formulations and their applicability. *Journal of Fluid Mechanics*, 661:482–510, 2010.

[ZLZ17] Xuan Zhang, Zhida Li, and Zhihua Zhang. Blocking mechanism study of self-compacting concrete based on discrete element method. *MS&E*, 269(1):012090, 2017.

[ZLZL18] Xuan Zhang, Zhida Li, Zhihua Zhang, and Yunyu Li. Discrete element analysis of the rheological characteristics of self-compacting concrete with irregularly shaped aggregate. *Arabian Journal of Geosciences*, 11(19):597, 2018.

[ZYZ+16] Wenqi Zhong, Aibing Yu, Guanwen Zhou, Jun Xie, and Hao Zhang. Cfd simulation of dense particulate reaction system: Approaches, recent advances and applications. *Chemical Engineering Science*, 140:16–43, 2016.

[ZZYY08] HP Zhu, ZY Zhou, RY Yang, and AB Yu. Discrete particle simulation of particulate systems: a review of major applications and findings. *Chemical Engineering Science*, 63(23):5728–5770, 2008.